Towards Haptic Intelligence for Artificial Hands: Development and Use of Deformable, Fluidic Tactile Sensors to Relate Action and Perception

by

Ruben Dario Ponce Wong

A Dissertation Presented in Partial Fulfillment
of the Requirements for the Degree
Doctor of Philosophy

Approved July 2013 by the
Graduate Supervisory Committee:

Veronica J. Santos, Chair
Panagiotis K. Artemiadis
Stephen I. Helms Tillery
Jonathan D. Posner
George Runger

ARIZONA STATE UNIVERSITY

August 2013

ABSTRACT

Human fingertips contain thousands of specialized mechanoreceptors that enable effortless physical interactions with the environment. Haptic perception capabilities enable grasp and manipulation in the absence of visual feedback, as when reaching into one's pocket or wrapping a belt around oneself. Unfortunately, state-of-the-art artificial tactile sensors and processing algorithms are no match for their biological counterparts. Tactile sensors must not only meet stringent practical specifications for everyday use, but their signals must be processed and interpreted within hundreds of milliseconds. Control of artificial manipulators, ranging from prosthetic hands to bomb defusal robots, requires a constant reliance on visual feedback that is not entirely practical. To address this, we conducted three studies aimed at advancing artificial haptic intelligence. First, we developed a novel, robust, microfluidic tactile sensor skin capable of measuring normal forces on flat or curved surfaces, such as a fingertip. The sensor consists of microchannels in an elastomer filled with a liquid metal alloy. The fluid serves as both electrical interconnects and tunable capacitive sensing units, and enables functionality despite substantial deformation. The second study investigated the use of a commercially-available, multimodal tactile sensor (BioTac sensor, SynTouch) to characterize edge orientation with respect to a body fixed reference frame, such as a fingertip. Trained on data from a robot testbed, a support vector regression model was developed to relate haptic exploration actions to perception of edge orientation. The model performed comparably to humans for estimating edge orientation. Finally, the robot testbed was used to

perceive small, finger-sized geometric features. The efficiency and accuracy of different haptic exploratory procedures and supervised learning models were assessed for estimating feature properties such as type (bump, pit), order of curvature (flat, conical, spherical), and size. This study highlights the importance of tactile sensing in situations where other modalities fail, such as when the finger itself blocks line of sight. Insights from this work could be used to advance tactile sensor technology and haptic intelligence for artificial manipulators that improve quality of life, such as prosthetic hands and wheelchair-mounted robotic hands.

DEDICATION

To my family, for their love and support throughout all stages of my life.

To my girlfriend Asuka, for being there for me no matter what.

To all my friends I met as a student in Arizona State University in the last nine years, for all the great times we shared.

ACKNOWLEDGMENTS

First and foremost I would like to thank my doctoral committee chair, Dr. Veronica Santos, for her invaluable guidance and support throughout the five years of the course of my graduate studies at Arizona State University. Her mentorship has allowed me to grow as a researcher and engineer as a whole.

I would also like to acknowledge my doctoral committee members: Dr. Panagiotis Artemiadis, Dr. Stephen Helms-Tillery, Dr. Jonathan Posner, and Dr. George Runger for their helpful feedback throughout my graduate career. Their input has helped me shape my research and improve the quality of my work.

The material presented in Chapter 2 is based upon work supported by the National Science Foundation under Grant No. 0954254. The authors would like to thank Dr. Philip Wheat and Dr. Steven Klein who assisted with clean room and microfabrication training, as well as Charles Corredor who helped with the Faraday cage experimental setup.

For the material presented in Chapters 3 and 4, the authors wish to thank Ismael Reveles for assistance with data collection and literature review, Dr. Stephen Helms Tillery for suggestions on the data collection protocol, and Dr. Ehsan T. Esfahani for recommending the Hilbert-Huang Transform technique. This work was supported in part by the National Science Foundation under Grants No. 0932389, 0954254, and 1208519.

Also, I would like to thank the ASU Ira A. Fulton Schools of Engineering and the ASU Graduate College for funding me at various points of the doctoral program. Their awarded fellowships allowed me to focus solely on research.

Finally, I would like to thank all my fellow graduate students and lab mates that have assisted me in the day-to-day lab activities with their teachings, suggestions, and constructive criticism.

TABLE OF CONTENTS

Page

CHAPTER Page

LIST OF TABLES

TABLE Page

LIST OF FIGURES

FIGURE Page

FIGURE Page

FIGURE Page

CHAPTER 1

INTRODUCTION

In the clinical setting, the "haptic intelligence test" is a tactile performance test used to evaluate blind or visually impaired individuals' abilities to accomplish tasks via touch rather than vision (Aiken, 2004). Such clinical tasks include using the sense of touch to analyze patterns of dots, assemble puzzle parts, and identifying missing parts of an object. In this dissertation, we use the phrase "haptic intelligence" to refer to the ability to relate actions of the fingertip to perception of objects through the sense of touch alone. A necessary component of haptic intelligence, in this sense, is the ability to map finger-object interactions into low-level raw tactile signals and then into high-level abstractions about object properties that can inform future manipulations of the object. While sensing involves the collection of raw data from interactions with the environment, perception involves the context-dependent interpretation of those tactile signals. Just as humans store memories of experiences, a robot database of haptic experiences could be maintained and referenced when novel objects or situations are encountered.

Tactile sensing in robotics is an area of rapid growth within the last few decades. In contrast to sight and hearing, touch requires physical interaction with the environment in order to collect meaningful information. For the sense of touch especially, action is tightly coupled with perception. That is, different types of physical interactions with an object will yield specific information about different object properties. Human studies on haptic object exploration have

shown that humans selectively perform hand movements based on the object property of interest (Lederman & Klatzky, 1987). For instance, extracting surface roughness information requires a lateral motion of the fingertip while estimating object stiffness requires a squeezing or poking motion (Lederman & Klatzky, 1987). Roboticists who use these human exploratory procedures as inspiration must address the challenges of developing algorithms that can efficiently collect, interpret, and use tactile sensor data to develop models of objects that can be used to inform future actions. Depending on a robot's task, different exploratory actions and action-specific or sensor-specific post-processing of tactile sensor data may be necessary.

Humans are constantly interacting physically with their environment with their fingertips as they perform different tasks, such as lightly holding a soda can or using a precision grasp for inserting a screw into a hole. In cases where other senses such as vision cannot be used (e.g. in the dark, behind obstacles, or when the hand itself occludes line of sight), humans often rely on touch to accomplish tasks, such as grabbing an object that has fallen underneath a couch. In order for robots to successfully and safely interact with humans or in an environment with objects designed for human hands, tactile sensing capabilities are critical. For instance, lack of tactile feedback could result in preprogrammed grasps that erroneously crush or drop a grasped object. Thus, human tactile sensing capabilities are typically viewed as the gold standard for robotic tactile sensing.

BRIEF OVERVIEW OF TACTILE SENSING IN HUMANS AND ROBOTS

It is well known that a large part of the human brain is dedicated to sensations of the hand, as shown by the cortical sensory homunculus (Penfield & Rasmussen, 1950). In particular, the fingertips contain thousands of tactile afferents which are neurons that send information from mechanoreceptors to the brain (Johansson & Flanagan, 2009). There are four main types of mechanoreceptors, each being sensitive to mechanical stimuli of different natures. Fast-adapting type I Meissner endings can sense relatively high frequency (~5-50 Hz) dynamic skin deformations. Slow-adapting type I Merkel endings measure static and low frequency (<5 Hz) forces. Fast-adapting type II Pacini endings sense high frequency vibrations (~40-400 Hz) propagating through tissues. Slow-adapting type II Ruffini-like endings measure low dynamic stimuli such as skin stretch. The human ability to carry out a variety of dexterous activities is enabled in part by the large number of tactile afferents which provide rich tactile information and the brain's ability to extract high-level, abstract information for specific tasks. In order to provide robots with human-like tactile capabilities, one must first have an adequate tactile sensor technology and then one must address the challenge of efficiently analyzing and interpreting large quantities of multimodal data.

Several review papers have been published that summarize the artificial tactile sensing technologies for robotics applications (Tiwana, Redmond, & Lovell, 2012; Dargahi & Najarian, 2005; Dahiya, Metta, Valle, & Sandini, 2010; M. H. Lee & Nicholls, 1999). The different types of transduction mechanisms

each have their strengths and weaknesses, and some of them are more appropriate for certain situations than others. For instance, piezoelectric sensors are well suited for dynamic stimuli but less so for sustained applied forces.

As known from studies of human tactile afferents, biological mechanoreceptors are specialized for particular types of stimuli and the human fingertip is equipped with multiple sensing modes. A multimodal sensor capable of measuring object hardness, temperature, and contour has been developed (J. Engel, Chen, Fan, & Liu, 2005). The sensor was fabricated using standard microelectromechanical systems (MEMS) techniques and included multiple components such as strain gauges and thermocouples, each dedicated to measuring specific types of stimuli. Although the sensor is flexible, the sensor's robustness to substantial deformations could be enhanced. The HEX-O-SKIN is a tactile module consisting of a printed circuit board connected to various discrete sensors embedded within a transparent elastomer (Mittendorfer & Cheng, 2011). Proximity sensors measure light touch, MEMS accelerometer measure vibration and orientation, and thermistors measure temperature. Hexagon shaped patches could be interconnected to cover large surface areas. However, its low spatial resolution makes them unsuitable for use as fingertip sensors.

To enhance the spatial resolution of artificial fingertip sensors, small electrical components are used which are typically thin, solid metal films encapsulated in a flexible, protective layer. Repeated deformation causes these metal films to fracture, rendering the sensor unusable. Since fluids do not suffer from fatigue or cracking issues, fluids have started to be incorporated into tactile

sensor designs. A eutectic liquid metal alloy has been used as electrical interconnects for LEDs (H.-J. Kim, Son, & Ziaie, 2008) and carbon nanotube sensing elements (Hu, Shaikh, & Liu, 2007a). A similar liquid metal alloy has been used in a sensor capable of measuring applied stress and multiaxial strain (Y.-L. Park, Chen, & Wood, 2012). A different use of conductive fluid can be observed in the BioTac, a multimodal sensor that can simultaneously measure pressure, vibration, and temperature (Nicholas Wettels, Santos, Johansson, & Loeb, 2008). A weakly conductive fluid is encapsulated between a deformable skin and sensing electronics embedded in a rigid core. The fluid serves as the medium through which static and dynamic stimuli are transferred to sensing elements.

BIOLOGICAL TACTILE SENSING AND HAPTIC PERCEPTION

Tactile sensors are merely the tools for collection of raw signals. Once low-level raw data have been collected, they must be post-processed and transformed into high-level abstractions in order for a robot to make inferences about its environment. Thus, the development or acquisition of an adequate tactile sensing technology is only the first, albeit critical, step in the haptic perception process. The use of capable artificial sensors must be coupled with appropriate processing algorithms. In order for a robotic system to make decisions, the robot must either be preprogrammed or able to adapt to new situations from learned experiences (Duffy & Joue, 2000). A more subtle point is that the robot must be able to relate its internal reference frame to countless other

external reference frames (e.g., gravity, other agents, objects in the environment). This provides, for example, the robot with knowledge about an object's pose relative to that of its own end-effector (Driels, 1986; D. M. Siegel, 1991). This is crucial information that could serve as the foundation for exploration and identification of objects (Lederman & Klatzky, 1987) and multifinger manipulation of objects by artificial hands. As with many engineered systems, the biological hand is a source of inspiration for perception and dexterous capabilities.

Haptic Perception of Object Shape. A seminal study by Lederman and Klatzy established that humans use a variety of "exploratory procedures" (EP) (Lederman & Klatzky, 1987) in order to haptically acquire knowledge about object properties. The properties can be related to the object's substance (texture, hardness, temperature, weight), structure (weight, volume, global shape, local shape), or function. It was found that specific exploratory procedures were necessary, if not optimal, for extracting specific object properties. For instance, lateral motion of a fingertip against a surface is typically employed for acquiring information on texture.

In a free sorting experiment, subjects placed objects into bins based on whether the objects were perceived as 'similar' with and without vision (Roberta L. Klatzky, Lederman, & Reed, 1987). It was found that substance ("how an object feels") was important for encoding the representation of an object through haptic means. However, structure ("how an object looks") was more important when vision was allowed. Furthermore, "economical" hand movements that

provide accurate information with the least cost were observed (Roberta L. Klatzky et al., 1987). Global shape and size were considered less economical for haptic exploration without vision. Although contour following provides local shape information for fine discrimination it is not considered economical due to its slow execution time, complexity of movement, and 'small view' of an object. (R. L. Klatzky & Lederman, 1999; Roberta L. Klatzky et al., 1987; Roberta L. Klatzky & Lederman, 1992).

A different study examined the sufficiency of different EPs for haptic object identification. Typically, subjects performed a two-stage sequence. The first stage would focus on coarse, global information through the application of enclosure and unsupported holding (Roberta L. Klatzky & Lederman, 1992). In the second stage, finer information would be extracted via EPs such as lateral motion and contour following. This behavior suggests that coarse information aids the subject in making initial hypothesis of the object identity, which in turn guides the selection of the subsequent EP (Roberta L. Klatzky & Lederman, 1992; Lederman & Klatzky, 1997). In order to reach a 100% accuracy in object identification, multiple seconds were needed.

A study on 3D haptic shape perception investigated the influence of object features such as curvature, aspect ratio, and edges on the ability of unimpaired subjects to quickly and accurately identify objects through touch alone (Plaisier, Bergmann Tiest, & Kappers, 2009). Free exploration of the objects was allowed such that subjects could employ any EPs with the dominant hand only. One conclusion of the study was that edges and vertices were the most salient local

features of 3D shape and that haptic searches were performed efficiently when the target object had edges (Lederman & Klatzky, 1997; Plaisier et al., 2009).

Response of Tactile Afferents to Skin Deformation. In spite of having a small size ranging between 7-12 mm in diameter, the fingertip provides rich tactile information. (R. H. LaMotte & Srinivasan, 1987; Robert H. LaMotte & Srinivasan, 1993; M. A. Srinivasan & LaMotte, 1991). The capability of perceiving shape at this small size could be attributed to skin conforming to the local shape, resembling a smaller version of whole-hand enclosure (R. L. Klatzky & Lederman, 1999).

Human and non-human primate studies on local shape perception have focused on edges and curvature. Slowly adapting SA I afferent units (Merkel endings) that respond to low-frequency (< 5 Hz) skin deformations (Johansson & Flanagan, 2009) are highly sensitive to spatial discontinuities, especially edges, in humans (Johansson, Landstrom, & Lundstrom, 1982), non-human-primates (Phillips & Johnson, 1981). This suggests that representations of local shape are actually encoded initially at the periphery by cutaneous mechanoreceptors (R. L. Klatzky & Lederman, 1999).

Despite changes in orientation, object curvature and the subsequent effects on skin curvature appear to be encoded primarily by SA I afferent units (R. H. LaMotte & Srinivasan, 1987; Mandayam A. Srinivasan & LaMotte, 1987). Studies in humans and non-human primates have suggested that the following pairs of variables can be perceived independently: curvature and contact force (Goodwin, John, & Marceglia, 1991), shape and orientation (R. H. LaMotte,

Friedman, Lu, Khalsa, & Srinivasan, 1998), and shape and stroke speed (R. H. LaMotte & Srinivasan, 1987).

In addition to SA I afferents, fast adapting FA I units respond to dynamic skin deformations, but for a higher frequency range (5-50 Hz) (Johansson & Flanagan, 2009). The relative contributions of these two types of mechanoreceptors depend on the finger-object interaction. In static-like shape indentations, SA I units seem to encode orientation (Dodson, Goodwin, Browning, & Gehring, 1998; Khalsa, Friedman, Srinivasan, & LaMotte, 1998). In dynamic shape indentation, both SA I and FA I units are helpful in orientation perception (R. H. LaMotte et al., 1998). Although FA I only provides rough outlines of indentation and not fine 3D shape information (R. H. LaMotte et al., 1998), they encode sharpness better than SA I units (Robert H. LaMotte & Srinivasan, 1987).

Haptic Perception of Orientation

Discrimination Thresholds. The perception of orientation has been studied with stimuli such as narrow cylindrical and rectangular bars (S. J. Bensmaia, Hsiao, Denchev, Killebrew, & Craig, 2008; Sliman J. Bensmaia, Denchev, Dammann, Craig, & Hsiao, 2008; Dodson et al., 1998; Fearing & Binford, 1991; M. A. Srinivasan & LaMotte, 1991). Passive indentation of cylinder into the finger pad could be perceived with discrimination threshold of 5.4° for cylinders with radius of 1.92 mm and 4.2° for cylinders with radius of 5.84 mm (Dodson et al., 1998). Improvements in orientation thresholds could be related to a greater amount of tactile afferents being activated (Goodwin et al.,

1991). A study that used rectangular bars and edges reported orientation discrimination thresholds of 20° (S. J. Bensmaia et al., 2008). In that study, edges that were scanned across the passive fingerpad were more easily discriminated than those that were indented.

Tactile Spatial Anisotropy. The presence of a tactile spatial anisotropy has been hypothesized in the form of an "oblique effect" in which orientation discrimination is better along vertical and horizontal direction than along diagonal directions with respect to the fingertip (Lechelt, 1988, 1992). However, there is debate on the source of the anisotropy and on the more accurate orientations. One study on line orientation with sighted, visually impaired, and blind subjects found that discrimination thresholds were 2.5°, 5°, and 15° for horizontal, vertical, and diagonal (right or left by 45°) stimuli, respectively, where horizontal refers to the radial-ulnar axis and vertical refers to the distal-proximal axis of the fingertip (Lechelt, 1988). Another study also found horizontal lines to be more easily discriminated (threshold of 16°) than vertical lines (threshold of 31°) (S. J. Bensmaia et al., 2008). In contrast, a different study using indented gratings reported sensitivities that were highest for vertical orientations, intermediate for diagonal orientations, and lowest for horizontal orientations (Essock, Krebs, & Prather, 1997).

Effect of the Cylindrical Nature of the Fingertip. The complexity of indenting rigid cylindrical bars on the deformable fingerpad is presented in a study on development of a cylindrical tactile sensor (Fearing & Binford, 1991). Contact area depended on the bar's curvature and orientation relative to the

fingertip. Interestingly, elliptical contact areas would not be aligned with the bar's long axis. The study predicts that orientation discriminability degrades as the bar's curvature decreases and as the bar is rotated away from the short axis of the finger (Fearing & Binford, 1991).

HAPTIC EXPLORATION IN ROBOTICS

Haptic Exploration of Object Substance ("how an object feels").

Human inspired strategies for haptic exploration have been previously implemented on robotic systems. One study employed tapping and squeezing EPs with a sensor composed of strain gauge and polyvinylidene fluoride (PVDF) films in order to determine hardness (Takamuku, Gomez, Hosoda, & Pfeifer, 2007). Mean strain gauge values from the squeezing procedure and patterns in the PVDF signals during tapping movements were used as inputs to self-organizing maps (SOM) that clustered objects based on hardness. Another study sought to correctly identify twelve object surfaces based on dynamic tactile data (H. Liu, Song, Bimbo, Seneviratne, & Althoefer, 2012). A 6DOF force/torque transducer attached to a BarrettHand served as a tactile sensor while sliding on surfaces of various objects. Five physical properties, such as friction coefficient and mean squared error of vibration signals, were extracted and input to various supervised learning models. The naïve Bayes classifier performed the best with an accuracy of 88.5% when identifying a material from a set of twelve.

Object compliance of five different materials were estimated using the BioTac sensor (Su, Fishel, Yamamoto, & Loeb, 2012). The finger-shaped sensor

was indented into samples of different stiffnesses. Electrodes located on the sensor core capable of measuring skin deformation revealed that skin deformation near the fingertip, especially radial and ulnar aspects, could be related to object compliance.

Another recent study used tactile feedback to label perceived objects with "haptic adjectives", such as sticky and bumpy (McMahon et al., 2012). In this study two BioTacs were used on a Willow Garage PR2 robot to explore objects. After performing five EPs, parameters were extracted and input to static and dynamic learning algorithms. Robot predictions were compared to those from a human study. It was concluded that meaningful sets of adjectives could be produced for novel objects when using all EPs and that specific EPs were more useful for labeling objects with certain haptic adjectives.

Haptic Exploration of Object Structure ("how an object looks"). A robotic hand with 45 piezoelectric sensors grasped objects in order to cluster them according to global shape using SOMs (Johnsson & Balkenius, 2007). Input parameters for the SOM models were extracted from proprioceptive and tactile feedback in order to discriminate between blocks, spheres, and cylinders. In a different study, a three axis tactile sensor was used to control a robotic arm as it performed contour-following on a curved surface (Abdullah, 2011). The test object and its geometric features were larger than the tactile sensors, which were used primarily for force control. Proprioceptive feedback, as opposed to tactile feedback, was used to determine object contour.

A 3-degree-of-freeedom Universal Robot Hand used resistive tactile sensors during a rotational manipulation task to determine the shape of small, symmetric objects (Nakamoto, Kobayashi, & Kojima, 2010) As the objects were rotated by two digits, tactile patterns were recorded and matched to known, predefined patterns. The robotic system could distinguish between a cylinder, hexagonal prism, and octagonal prism with accuracies of at least 90%. Another study used a biomimetic tactile sensor to perform active contour following on four different 2D shapes (Martinez-Hernandez et al., 2013). The control schematic employed a Baye's classifier to guide the sensor movements around 90° corners. Once the shape's full contour had been determined, the history of the fingertip positions was used to determine the objects's global shape with a 100% classification accuracy. In another study, a capacitive touch sensor was moved across 26 Braille alphabet characters to learn how to accurately distinguish them (Bologna, Pinoteau, Garrido, & Arleo, 2012). The sequence of activation of the six sensing units in the robotic sensor were used to extract inputs for a naïve Bayes classifier with an 89% accuracy.

Haptics-based Learning. While the studies mentioned above are capable of accomplishing predefined tasks accurately, unstructured environments and novel objects would likely necessitate re-programming and re-training of the robot. Recent work on haptics-based learning with robotic systems have led to the development of algorithms that can make predictions more efficiently. A robotic system using the BioTac sensor employed Bayesian exploration to sequentially select from prescribed exploratory movements in order to achieve

certainty thresholds for predictions of texture more efficiently (J. A. Fishel & Loeb, 2012). Predictions converged as more exploratory movements were performed. Each new movement was selected to best discriminate between candidates that seemed similar based on all prior information. A total of 117 textures were discriminated with a classification success rate of 95.4%. A related study applied a similar strategy on multiple tactile modalities to discriminate between ten objects (Xu, Loeb, & Fishel, 2013). While the previous study on textures used primarily vibration signals and proprioceptive feedback, this study on objects used estimates of object compliance, texture, and thermal conductivity. New trials were added to a growing database (memory) to account for long-term changes in signals such as drift. The success rate in identifying the objects was 99%.

In another study, robot movements were learned through curious exploration for a texture-classification task (Pape, Oddo, Controzzi, Förster, & Schmidhuber, 2012). The robot learned to make exploratory movements based on the sensory feedback without any supervision. Previously learned motor skills were further refined during learning. A 92% accuracy was reached when classifying seven textures.

Overall, there seems to be a consensus that emerging sensor technologies and their corresponding mathematical models continue to improve, but much work remains to accomplish the goal of enabling robots with intelligent grasp and manipulation capabilities (Tegin & Wikander, 2005). Robots need to be able interact safely and adequately in dynamic, unstructured environments.

OVERVIEW OF EXPERIMENTS

This dissertation is comprised of three separate studies that aim to advance haptic intelligence for artificial hands. Chapter 2 describes the development and proof-of-concept evaluation of a novel, capacitive, microfluidic tactile sensor skin capable of measuring normal forces comparable to those from light touch. The objective of this study was to create a robust, highly deformable sensor that could be used on artificial fingertips in real world environments.

Chapter 3 investigates the use of a commercially-available multimodal tactile sensor to estimate the orientation of a salient geometric feature (an edge) with respect to a fingertip reference frame. The aim of this study was to use bio-inspired exploratory procedures and supervised learning regression models to estimate edge orientation for stimuli having various widths and stiffnesses. Estimating orientation of a feature (or object) relative to itself and its environment is an important first step for an artificial system to determine subsequent physical interactions with the object.

Chapter 4 examines the use of the commercially-available multimodal tactile sensor for haptic exploration of finger-sized geometric features. The objective of the study was to determine the efficiency and accuracy of different exploratory procedures for estimating properties of small geometric features such as bumps and pits. Identification of small features could enable identification of an object and its pose within an artificial hand, particularly when visual feedback would not be helpful.

CHAPTER 2

A FLEXIBLE MICROFLUIDIC NORMAL FORCE SENSOR SKIN FOR TACTILE FEEDBACK

INTRODUCTION

There are three primary sensing modalities employed in microelectromechanical systems (MEMS) force sensors: resistive, piezoelectric, and capacitive (Yousef, Boukallel, & Althoefer, 2011). Resistive sensors detect mechanical stimuli by producing changes in resistance. Traditional high sensitivity, resistive strain gauges typically have issues such as fragility and low flexibility. Recently, some of the existing limitations have been addressed, for instance, with the development of conductive polymer composites (J. M. Engel et al., 2006; Dang et al., 2008; Ventrelli, Beccai, Mattoli, Menciassi, & Dario, 2009). Piezoelectric sensors generate voltage as applied forces are measured. Piezoelectric composites are flexible and chemically resistant but inappropriate for static loading and prone to output signal drift. Capacitive sensors, the focus of the present work, typically consist of pairs of plates whose capacitance is increased as the distance between opposing plates decreases or the permittivity of the dielectric medium between the plates increases. Capacitive sensors offer advantages such as high sensitivity, tunable spatial resolution when used in an array configuration (Yousef et al., 2011), and a simple, well-known governing equation. Electrical capacitance depends on the geometry of and distance between the electrodes and dielectric properties of the material between the electrodes.

Capacitive Sensors. For many applications, capacitive sensors are created by embedding conductive metal plates in flexible materials such as the polydimethyl siloxane (PDMS) polymer. The conductive plates are typically created using metal deposition such as evaporation (Adrega & Lacour, 2010; Micolich, Bell, & Hamilton, 2007), electroplating (H.-K. Lee, Chang, & Yoon, 2006), or sputtering (Feng & Zhao, 2007). Although the polymeric packaging is relatively robust to mechanical deformations and chemical degradation, the conductive plates and interconnects are susceptible to failure due to fractures and fatigue. Even a small crack in a plate or connect can result in the irreparable loss of electrical connectivity and failure of the sensor (Zhang & Wang, 2008). Fabrication of curved, doped nano-ribbons that can withstand significant deformation (D. H. Kim et al., 2008) and the deposition of spiral copper wire around a nylon wire that elongates when stretched (Cheng, Tsao, Lai, & Yang, 2011) have been used to provide electrical connections in flexible substrates. Capacitive sensors have sensitivity and tunable spatial resolution (Yousef et al., 2011). Arrays of capacitors have been used for a wide range of applications. Capacitance-based micro tactile sensor arrays are capable of detecting mN forces with negligible cross-talk between sensing elements, although hysteresis can be an issue (Gray & Fearing, 1996). A macro-scale pressure sensor made of fabric detected pressure fields with magnitudes of hundreds of fF capacitance spread around a 1 m^2 area (Sergio, Manaresi, Tartagni, Canegallo, & Guerrieri, 2002). A sensor capable of measuring phase fraction distribution of two-phase flows via permittivity variations was developed to distinguish between different types of

dielectric media between the capacitor plates (Da Silva, Schleicher, & Hampel, 2007). A tactile sensor capable of measuring normal and shear forces was created by depositing an array of gold thin films in PDMS and using 2x2 taxels as a single sensing unit (Hyung-Kew Lee, Jaehoon Chung, Sun-Il Chang, & Euisik Yoon, 2008; H.-K. Lee et al., 2006).

Fluids in MEMS Sensors. Fluids have been integrated into a variety of MEMS sensors for different applications. For instance, a vibration sensor was developed which had chambers filled with an NaCl solution (K. H. Kim & Seo, 2008). Mechanical vibrations induced motion of the electrolyte's ions, allowing the measurement of vibrations over a wide range of frequencies. For tactile sensing, a sensor was created by filling microchannels with an NaCl solution (Tseng et al., 2009). Mechanical deformation applied pressure to the reservoirs, displaced fluid, and produced measurable changes in resistance. A macroscale fluid-based tactile sensor called the BioTac (SynTouch, Los Angeles, CA) uses fluid as a transduction medium for both electric current and mechanical vibrations (Nicholas Wettels et al., 2008). This multimodal sensor consists of an elastomeric skin that has been inflated away from a rigid, fingertip-shaped core by a weakly conductive fluid (N. Wettels, Smith, Santos, & Loeb, 2008). An array of impedance electrodes embedded in the rigid core is used to measure changes in impedance as the fluid flowpath is altered by mechanical deformation. A hydrophone is used to measure vibrations at the skin-object interface. Each of these three sensing devices utilizes fluids encapsulated by elastic materials. Recently, fluids have been used as wires to connect sensing elements with

external circuitry. A liquid metal alloy called Galinstan has been used in MEMS devices to create robust wire paths capable of being bent, twisted, and stretched. Galinstan-filled microchannels enabled the powering of LED lights despite the bending and twisting of the device (H.-J. Kim et al., 2008). In another application, a stretchable force and temperature sensor was created with carbon nanotubes and Galinstan electrical connections embedded in PDMS (Hu, Shaikh, & Liu, 2007b). Galinstan is a fairly conductive (0.435 Ωm electrical resistivity (Surmann & Zeyat, 2005)) fluid created by Geratherm (Geschwenda, Germany) for use in thermometers as a nontoxic substitute for mercury ("Galinstan MSDS," 2006). Galinstan is a eutectic metal alloy composed of gallium, indium, and tin (Surmann & Zeyat, 2005). The voltammetric (Surmann & Zeyat, 2005) and electromagnetic (Schulze, Karcher, Kocourek, & Mohring, 2006) properties of this relatively new compound have been recently established. A eutectic metal alloy composed of only gallium and indium (eGaIn) has been used in the design of a pressure sensor (Y. L. Park, Majidi, Kramer, Bérard, & Wood, 2010), bend sensor (Kramer, Majidi, Sahai, & Wood, 2011; Majidi, Kramer, & Wood, 2011), and multi-axis strain sensor (Y. L. Park, Chen, & Wood, 2011). A PDMS skin having microchannels filled with eGaIn was wrapped around a human finger. Deformation-induced changes in resistance of the fluidic electrical circuit allowed for the measurement of joint angles as the finger was bent.

A Capacitive Microfluidic Normal Force Sensor. Tactile sensing is a field of great interest due to its potential impact on robot-assisted surgery and robotic grasp and manipulation, among other applications. In many cases, visual

and acoustic feedback alone does not provide the information necessary for decision making. A classic case is that of an amputee who accidentally crushes or drops an object with his prosthetic hand due to inadequate tactile information about the hand-object interaction. Many review articles have discussed the complexity of the sense of touch and the many challenges that remain for artificial touch sensors (Dahiya et al., 2010; Maheshwari & Ravi Saraf, 2008; Yousef et al., 2011). Some of the sensor design requirements for robotic applications include robustness, sensitivity, fine spatial resolution, fast dynamic response, and flexibility (Dahiya et al., 2010).

PDMS-based capacitive tactile sensors have been developed to measure normal forces (J. M. Engel et al., 2006; Gray & Fearing, 1996; H.-K. Lee et al., 2006) and shear forces (Hyung-Kew Lee et al., 2008), to determine the elasticity of a contacted object (Peng Peng, Rajamani, & Erdman, 2009), and to distinguish between different types of textures (Muhammad et al., 2011). For MEMS and microfluidic applications, PDMS offers advantages such as non-toxicity, high degree of flexibility, chemically inert nature, simple processing techniques, low cost, and impermeability to liquids (Jo, Van Lerberghe, Motsegood, & Beebe, 2000; C. Liu, 2007; Lotters, Olthuis, Veltink, & Bergveld, 1997; Schneider, Fellner, Wilde, & Wallrabe, 2008). Thus, PDMS provides protection from the environment for the embedded sensor electronics. The existing PDMS-based tactile sensors use embedded solid metal films (Gray & Fearing, 1996; Hyung-Kew Lee et al., 2008; H.-K. Lee et al., 2006; Muhammad et al., 2011) or carbon nanotubes (J. M. Engel et al., 2006) in a protective PDMS material. These

designs are prone to failure when deformed, for example around a robotic finger, and are therefore challenging to implement in robotic applications where conformal wrapping of curved surfaces or robustness to repetitive deformation is necessary.

In this work, we present a flexible, capacitive, microfluidic sensor for normal force sensing with microchannels filled with Galinstan that serve as both the flexible wire paths and the conductive metal plates that make up the capacitive sensing units. Novel features of the sensor include its deformable capacitive plates and heterogeneous, deformable dielectric medium. The prototype has a 5x5 array of individually addressable 0.5 mm x 0.5 mm taxels. The liquid metal-filled microfluidic channel design ensures the robustness of the sensor as there are no solid components that can crack and fail. The multilayer design allows for nonlinear tuning of the sensor response to the desired load. We present the sensor's spatial resolution and quantify the response of the capacitive sensor on flat and curved surfaces. Details of the sensor's design, fabrication, calibration, validation, and overall functional assessment are presented in this work to show the potential of using conductive fluids for sensor electronics.

METHODS

Prototype Fabrication. The capacitive, microfluidic sensor (*Figure 2.1*A) is fabricated using soft lithography and consists of two materials: a flexible elastomer to mimic the mechanical properties of human skin and a liquid metal to serve as flexible plates for the capacitive sensing units. The sensor

consists of four layers of PDMS. The two outermost PDMS layers contain microfluidic channels filled with Galinstan and the two inner layers seal the microfluidic layers and contain an array of square air pockets to tune the overall sensor's mechanical and electrical properties. The microchannels form a 5x5 array of taxels connected by in-plane wire paths (lengthways for the top layer and transverse for the bottom layer). The 125 μm thick microchannel wires pass through and connect five 0.5 mm x 0.5 mm taxel plates, each of which is separated from the next plate by 0.5 mm (*Figure 2.1*B). The 5x5 array of square air pockets uses the same layout and dimensions as the 5x5 array of plates in the microchannel layer.

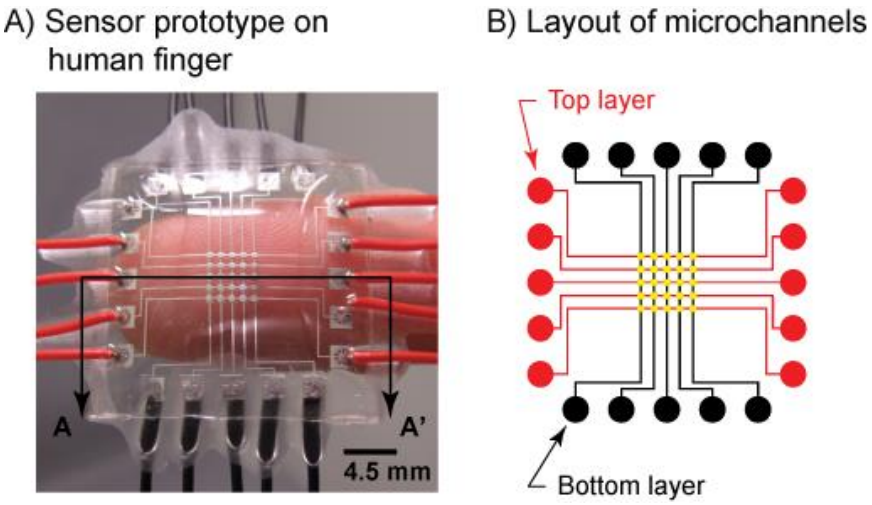

Figure 2.1. Capacitive microfluidic normal force sensor skin. A) A completed prototype shows the Galinstan embedded within the transparent PDMS. The 2D schematics in correspond to the cross-sectional view at A-A' (black line). B) Wire paths from the top half of the sensor run horizontally (red) while those from other the bottom half run vertically (black). The square capacitive taxels (yellow) represent the overlapping areas of the wire paths from both halves of the sensor.

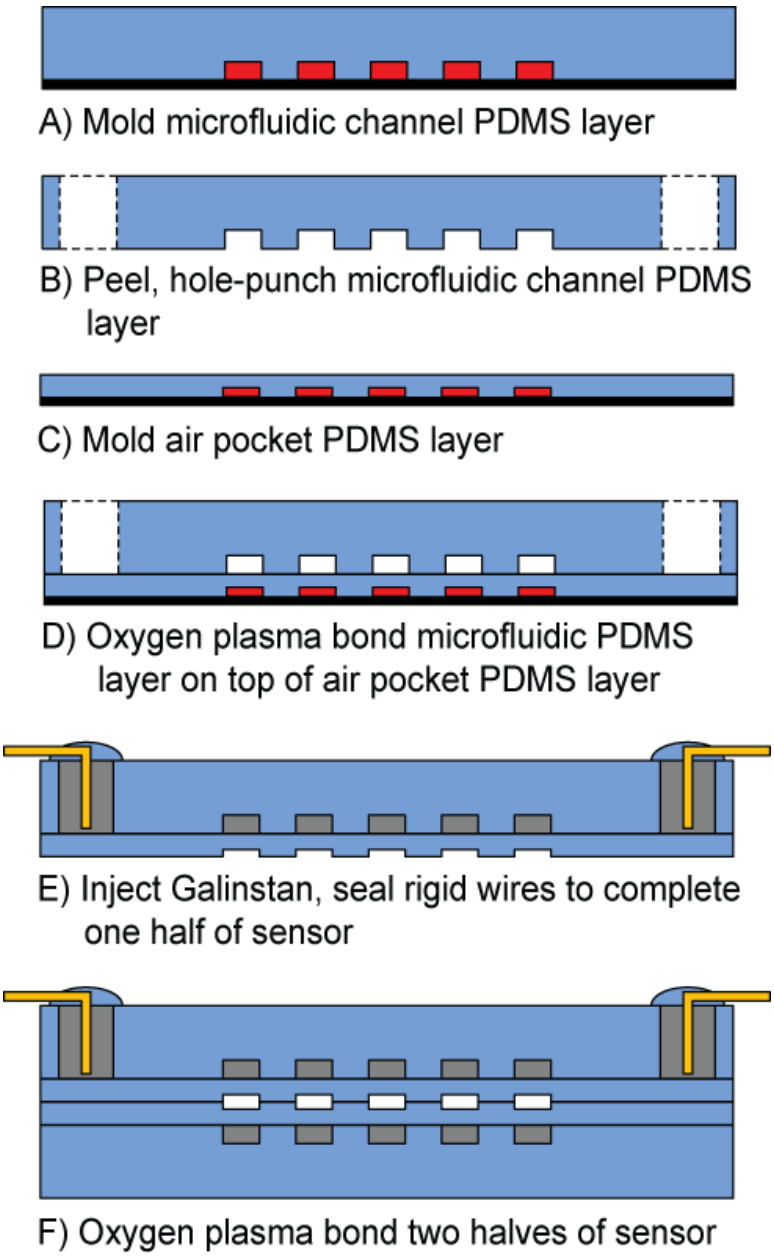

Figure 2.2. The fabrication process for a sensor prototype having a 5x5 array of capacitive taxels. The 2D schematics correspond to the cross-sectional view at A-A' in *Figure 2.1*A. A) The PDMS layer (light blue) having microfluidic channels is created. B) This layer is peeled from the wafer (black) containing the photoresist master (red) and hole-punched. C) The PDMS layer having the air

pockets is created. D) The patterned surface of the microchannel layer is O2 plasma bonded to the exposed surface of the air pocket layer still on the wafer. E) The bonded layers are peeled from the wafer and Galinstan (gray) is injected through the hole-punched inlet holes. Rigid wires (yellow) are carefully placed inside the Galinstan-filled inlet and outlet holes. The wires are sealed by pouring uncured PDMS over the holes and then curing the PDMS in an oven. F) Two separate halves of the sensor are aligned and bonded to create a functional sensor. Wire connects for the bottom PDMS layer are outside the cross-sectional plane and not shown. *Note: schematics not drawn to scale.

Soft lithography is a mature microfabrication strategy but we provide some details specific to our sensor design here. The PDMS masters for the microfluidic layers are fabricated by patterning 40 μm of SU-8 2015 photoresist (Microchem, Newton, MA) onto 4" silicon wafers (*Figure 2.2*A). The air pocket layer masters have 18 μm thick SU-8 2010 photoresist (*Figure 2.2*C). The masters are soft baked at 95^{o}C for 5 minutes and then exposed to 22.5 mW/cm^{2} UV light for 16 seconds using mylar masks. After a 5 minute post-exposure bake on a hot plate at 95^{o}C, the wafer is developed and then hard baked in an oven at 140^{o}C for 5 minutes. The thicknesses of the masters are measured using a profilometer (Dektak IIA, Sloan, Scotia, NY).

We use PDMS with a 10:1 A:B ratio (RTV615, Momentive, Columbus, OH). Each of the two 300 μm thick microfluidic channel layers (*Figure 2.2*A) is fabricated by spin coating PDMS onto the microchannel mold at 500 rpm for 30

seconds, curing it in an oven at 80^{o}C for an hour producing a 150 μm thick layer. This process is repeated a second time to produce 300 μm thick PDMS films (H.-K. Lee et al., 2006). The two ends of each wire-plate path are punched with a 700 μm diameter stainless steel TiN-coated round punch (Technical Innovations, Angleton, TX) to create through-holes that serve as inlets and outlets (*Figure 2.2*B) for the injection of Galinstan. The 25 μm thick air pocket layers are created by spinning PDMS onto the master at 3000 rpm for 30 seconds and curing it in an oven at 80^{o}C for an hour (*Figure 2.2*C). Each microchannel layer is bound to an air pocket layer (*Figure 2.2*D) after oxygen plasma treatment (PDC-001, Harrick Plasma, Ithaca, NY). We use isopropanol (IPA) to wet each layer and align the PDMS layers under a microscope to ensure accurate alignment of the 5x5 arrays of taxel plates and air gaps (Jo et al., 2000; Shifeng Li & Shaochen Chen, 2003). Each of the two-layer sandwiches is placed on a hot plate at 80^{o}C for one hour. We inject the Galinstan into each arm of the five wire-plate paths using a syringe with a 700 μm diameter stainless steel tube attached. Rigid, insulated 500 μm diameter wires are positioned in the inlet and outlet holes and uncured PDMS is poured over the holes. The system is placed in an oven for 2 hours at 80^{o}C to cure the PDMS applied to the channels' inlet and outlet holes. Electrical continuity and resistance of 1.5-2.5 Ω between the inlet and outlet of each wire-plate path are verified with a multimeter. This completes the fabrication of one half of the sensor (*Figure 2.2*E). O_2 plasma-IPA alignment and bonding technique is used to position and bond two halves of a sensor

perpendicular to one another in order to obtain a functional sensor prototype (*Figure 2.2*F).

Experimental Setup and Sensor Calibration. All experiments were performed with the sensor and its electrical circuit inside a Faraday cage for shielding from external electromagnetic noise. A single taxel was loaded by a uniaxial, point-load using a 1.5 mm x 1.5 mm rectangular-shaped tip (*Figure 2.3*). Double-sided sticky mylar tape was used to affix the sensor to a rigid, flat support plate affixed to a six degree-of-freedom force/torque transducer (Nano-17, ATI Industrial Automation, Apex, NC) having resolutions of 1/80 N and 1/16 N-mm for force and torque, respectively. We validated the calibration of the transducer using known weights.

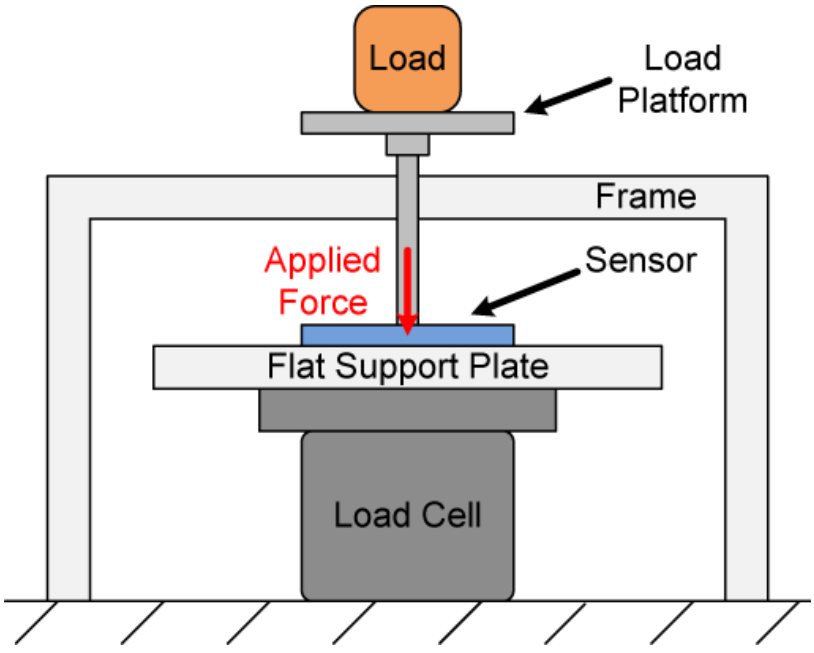

Figure 2.3. Experimental setup for point-loading of the microfluidic normal force sensor. The sensor is secured to a rigid, flat support plate that is attached to a load cell. A frame provides support to the slender post of the load platform and allows

precise alignment of the tip of the load platform over a single taxel. The flat support plate is replaced with a rigid, round support dowel for assessment of the sensor while wrapped around a curved surface. *Note: components not drawn to scale.

At the start of each experimental trial, sensor data were collected with the sensor at rest in an unloaded state. The tip of the load platform was then carefully centered over a single taxel with no overlap of adjacent taxel units and placed over the target taxel. Calibrated masses were added to the load platform to gradually achieve a total of 250 g (2.45 N). The actual transmitted load was determined by the force transducer. The masses and load platform were removed in reverse order (and with different load increments) until the sensor was completely unloaded. The sensor was allowed to equilibrate after each change in external load before data were collected for a 0.1 sec interval. A total of 20 measurements were made for each of ten independent trials. The sensitivity of two closest neighboring taxels to the loaded taxel was also assessed and is reported here. Eight experimental trials were conducted to assess the effect of surface curvature on sensor performance. Four trials were conducted for each of two sensor configurations: secured to a rigid, flat support plate or secured to a rigid, round support dowel having a curvature similar to that of a human finger. A round wood dowel with a radius of 0.635 cm (curvature of 1.575 cm^{-1}) was used as the curved surface.

Electrical Circuitry for Data Collection. We use a standard charge amplifier circuit to measure the capacitance of individual taxels (Jung, 2005). An AC input signal is sent through a capacitive sensing unit to the inverting input of an operational amplifier, and the non-inverting input is connected to ground. An external feedback capacitor and resistor are connected across the op amp's inverting input and output. While the input voltage across the external feedback capacitor remains constant, changes in taxel capacitance produces changes in charge, which translates to changes in the op amp's output voltage amplitude (Jung, 2005). Thus, the gain in amplitude of the AC input signal depends solely on the ratio of capacitance between the constant external capacitor and the variable capacitive sensing unit. Under the assumption of an ideal op amp, nodal analysis can be performed on the circuit to obtain,

$$V_{out} = -V_{in}\left(\frac{j\omega R_{out}C_{in}}{j\omega R_{out}C_{out}+1}\right), \tag{2.1}$$

where V_{out} is the output voltage amplitude, V_{in} is the input voltage amplitude, ω is the excitation frequency of the input signal, R_{out} is the external feedback resistance, C_{in} is the capacitance of a single taxel (connected to the op amp's inverting input), and C_{out} is the external feedback capacitance. If $\omega R_{out}C_{out} >> 1$, then Eqn. 2.1 simplifies to

$$V_{out} = -V_{in}\frac{C_{in}}{C_{out}} \tag{2.2}$$

By setting the input signal frequency f to 10 kHz, R_{out} to 200 MΩ, and C_{out} to 1 pF, the expression $\omega R_{out}C_{out}$ has a value of 12.566 and allows the use of Eqn. 2.2. In response to mechanical deformation under load, changes in taxel

capacitance C_{in} can be measured through changes in output voltage amplitude V_{out}. Equation 2.2 was confirmed by experimentally measuring V_{out} using known C_{in}, C_{out}, and V_{in}.values. This circuit is simple, has relatively fast response time, and filters the output signal to yield a high signal to noise ratio (Da Silva et al., 2007; Hyung-Kew Lee et al., 2008; H.-K. Lee et al., 2006; Sergio et al., 2002)

We used data acquisition boards (NI-6255 and NI-6211 National Instruments, Austin, TX) to collect data from the load cell at 1 kHz and a single sensor taxel at 200 kHz. The amplifier circuit input signal was sinusoidal with a peak-to-peak voltage of 1.0 V and frequency of 10 kHz. Sensor taxel data were collected at 20 times the input signal frequency in order to obtain accurate amplitudes from the output signal.

Post-processing of the raw load cell and capacitive sensor signals was performed in Matlab (Mathworks, Natick, MA). The amplitude of the capacitive sensor output voltage was determined for each cycle (using the maximum and minimum value for each wave). The mean load cell readings and mean taxel output amplitudes were computed for each 0.1 sec interval of data. Assuming constant V_{in} and C_{out} values, the changes in taxel capacitance C_{in} are directly reflected by changes in output voltage amplitude V_{out} (Eqn. 2.2). The relative percent change in output voltage amplitude, $\%\Delta V$, was calculated as

$$\%\Delta V = \frac{V_{out,loaded} - V_{out,unloaded}}{V_{out,unloaded}} \times 100\%, \qquad (2.3)$$

where the output voltage amplitude V_{out} is a function of load.

RESULTS AND DISCUSSION

Data were collected from individual taxels of a sensor prototype having a 5x5 array of capacitive taxels as well as the independent force transducer. The results from ten independent loading and unloading trials are shown first, starting with a brief description of the raw data for one trial. The calibration of the sensor is then presented and fit to a nonlinear model. We use the calibrated sensor to assess the reliability of the sensor's force measurements by comparing them to those of a calibrated load cell. Finally, a brief discussion details the sensor's spatial resolution and robust performance when wrapped around a curved surface.

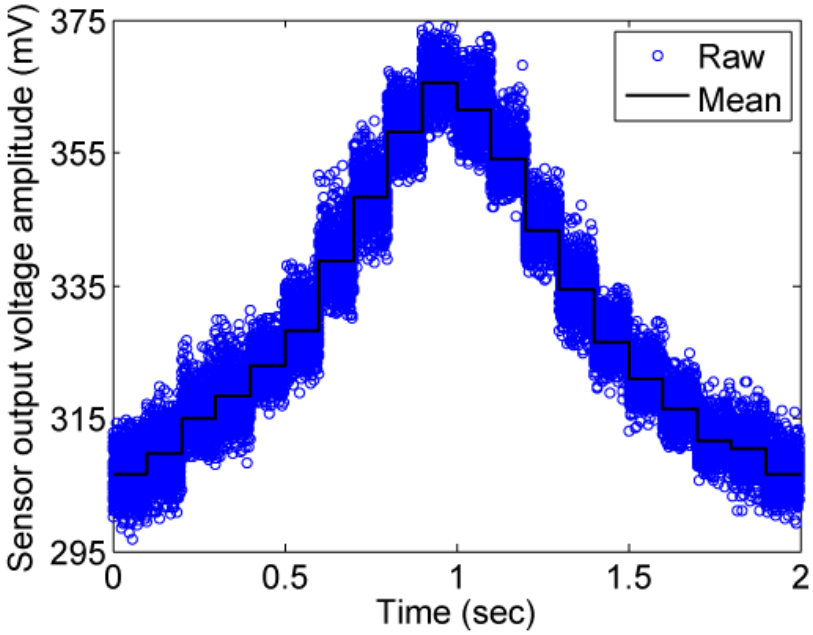

Figure 2.4. Sensor output voltage amplitude for a single calibration trial. The raw amplitudes for all cycles of the sinusoidal output signal (circles) and the mean for every 0.1 sec interval (line) are shown. Sensor output increased and decreased with loading (0-1 sec) and unloading (1-2 sec) as expected.

Direct Point-loading of a Single Taxel. *Figure 2.4* shows the raw sensor output voltage amplitudes and mean values for each 0.1 sec data collection interval varied with the external load. As expected, an increase in load force resulted in an increase in output voltage amplitude. The spread of amplitude points around the mean is approximately ±7 mV and is due to the low capacitance values being measured (on the order of tenths of pF). *Figure 2.5* shows the force measured by the sensor as a function of the measured change in sensor output voltage for ten independent trials on a single taxel under direct point-loading. We fit a power-law curve to the force values as a function of the calculated %ΔV using nonlinear regression analysis. The final regression model is given by

$$F_{fit} = 0.0455(\%\Delta V)^{1.73} - 0.00976(\%\Delta V)^{2.14},\ R^2 = 0.982, \qquad (2.4)$$

where F_{fit} is the force calculated by the curve fit. The regression model performs well at both high and low loads. Two power terms were needed to properly fit the nonlinear relationship between load and $\%\Delta V$ at low loads, and to accommodate the slight increase in the linear slope at higher loads (> approx. 1.2 N). Using the power-law fit, the residual plot in *Figure 2.5* shows that nine data points out of two hundred (4.5% of the data) fall outside the 95% confidence interval.

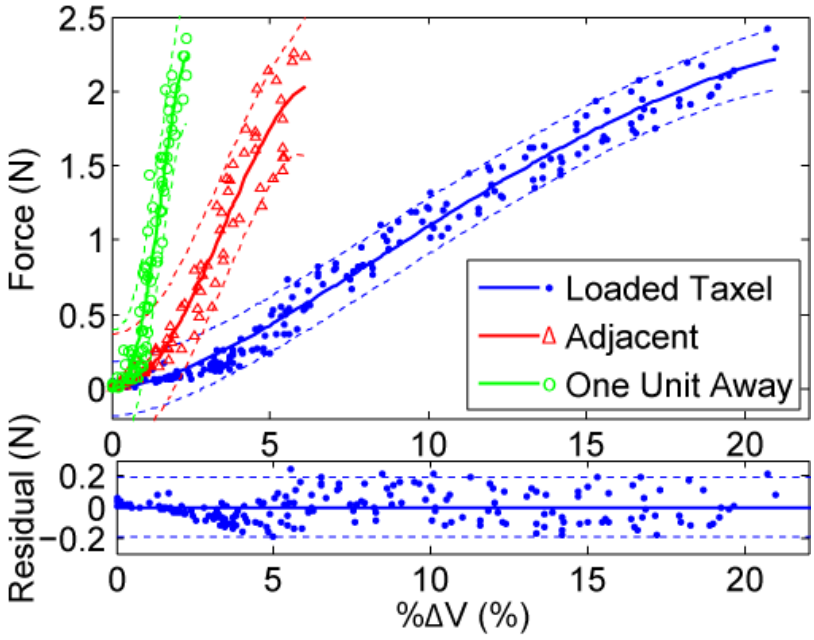

Figure 2.5. Sensitivity of taxels to direct and indirect loading. Calibration curves for a directly point-loaded taxel (blue dots and curve fit, Eqn. 2.4), an adjacent taxel (red triangles and curve fit), and a taxel one unit away (green circles and curve fit) during direct loading of a single taxel. The relative percent changes in output voltage amplitude (data points) were computed using Eqn. 2.3. Regression analysis using the sum of two power functions model was performed to calculate the calibration curves (solid lines) and 95% confidence bounds (dashed lines). The residual plot corresponds to the directly loaded taxel and shows that only 9 of 200 data points fell outside the 95% confidence bounds. Taxel response decreased substantially as distance from the point of load application increased, which suggests that the sensor has a spatial resolution of approximately 0.5 mm.

We only present data for loads under 2.5 N. We experimentally determined that a single taxel saturates at roughly a 500 g (4.9 N) load. At this

load, the innermost air pocket layers may have collapsed, causing the outermost microfluidic channel layers to touch. At this point, the fluidic capacitive plates would no longer be able to move closer to one another, and the capacitance would achieve a steady state value. It was noted that with masses of 350 grams or greater, the small tip of the load platform tended to become misaligned with respect to the target taxel thereby reducing the accuracy of the calibration between the load cell and taxel force readings. Considering the limitations of the experimental setup and our interest in characterizing sensor performance for forces associated with manipulation (approx. 0.15-0.90 N (Dahiya et al., 2010)), we used an upper limit of 250 g for the uniaxial loading of a single taxel.

Our sensor response to loading in the 0-2.5 N range is nonlinear at low loads, linear at moderate loads, and slightly nonlinear again at high loads. This nonlinear response can be attributed to many factors associated with the complex mechanical and electrical nature of the device. The primary sources of the nonlinear response are likely the curved deformations of the fluidic capacitance plates and the heterogeneous, deformable dielectric medium consisting of three sub-layers (i.e., two PDMS and one air). This structure and the nonuniform deformation of the capacitor plates result in complex variations in capacitance as the sensor is deformed. In addition, the viscoelastic nature of PDMS is characterized by highly nonlinear stress-strain curves (Goyal et al., 2009; Khanafer, Duprey, Schlicht, & Berguer, 2008; Mark, 2007; Schneider et al., 2008) which could also introduce some nonlinearity into the sensor output. Overall, the nonlinear behavior is a confluence of several physical effects which are difficult

to predict with simple analytical models and so we are investigating these effects further with coupled physics finite element models. Our multilayer sensor exhibits greater sensitivity at low loads, which can be exploited for robotic applications such as semi-autonomous haptic exploration in which light touch is important for the physical examination of objects. The multilayer design enables nonlinear tuning of the sensitivity over a wide range of forces which can be used to tailor the sensor response to the application of interest.

We evaluate the calibration curve fit (Eqn. 2.4) by directly comparing taxel force measurements to load cell force measurements as shown in *Figure 2.6*. This plot shows that there is nearly perfect agreement between the calibrated sensor and the independently measured load as demonstrated by the linear line having a slope near unity. A linear regression of the taxel's curve fit (F_{fit}) and load cell (F_{LC}) data yielded the following equation

$$F_{fit} = 0.973F_{LC} + 0.0264,\ R^2 = 0.9821 \tag{2.5}$$

The slope and y-intercept had values near one and zero, respectively, indicating that the calibration curve based on the sum of two power functions (Eqn. 2.4) is effective and that the capacitive sensor can measure forces in the 0-2.5 N range reliably. The 95% confidence bounds (±0.184 N) and residuals were also calculated for the comparison of taxel and load cell force measurements.

Due to the need for dynamic sensing in robotics and other applications, the experimental setup was modified slightly in order to apply a sinusoidal dynamic load to a single taxel. Forces up to approximately 2.5 N were applied at frequencies ranging from 0.4 to 4 Hz. Preliminary results show that sensor output

and load cell signals matched well in the loading and unloading phases since no significant lag could be perceived. It is widely known that the fast-adapting type II (FA-II) afferents in the human hand are capable of detecting vibrations ranging from 40 to 400 Hz (Johansson & Flanagan, 2008). Although, vibration detection is beyond the scope of the current prototype, the sensor appears to be capable of measuring low frequency dynamic loads and transient changes in loading, as when contact with an object is being made or released. Such capabilities are similar to those of fast-adapting type I (FA-I) afferents in the human hand which are maximally sensitive to vibrations ranging from 3 to 40 Hz, although responses to frequencies as low as 0.5 Hz have been reported (Jones & Lederman, 2006).

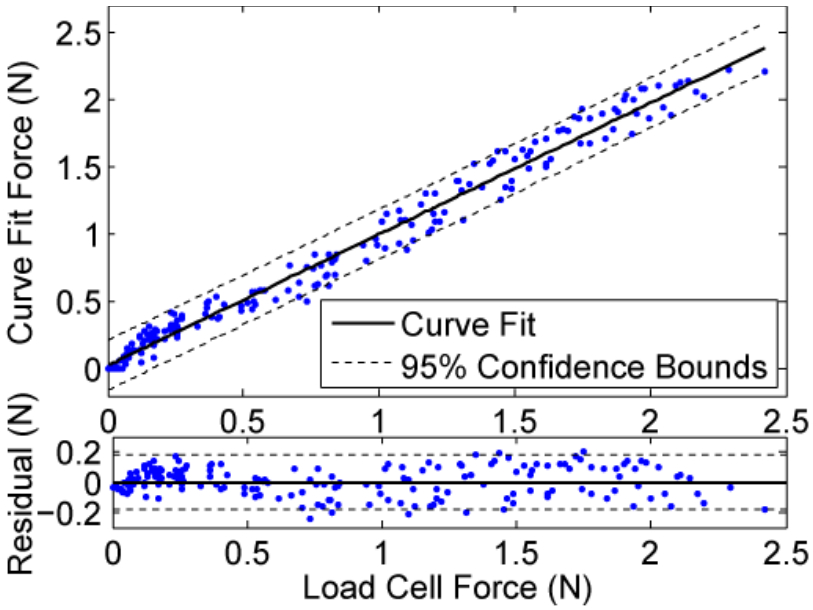

Figure 2.6. Comparison of force measurements for a directly loaded taxel as given by the sensor calibration curve and load cell. The relative percent change in output voltage amplitudes was used to calculate curve fit forces F_{fit} (dots) using the calibration equation. The linear regression (solid line; Eqn. 2.5) revealed a near one-to-one relationship between the microfluidic sensor and load cell

measurements. The residual plot shows that only 6 of 200 data points fell outside the 95% confidence bounds (dashed lines).

Spatial Resolution and Robustness to Bending. The small tip of the load platform enabled the external load to be centered directly over a single taxel. However, force from the applied load is transmitted to neighboring taxels. To assess the sensitivity of taxels to indirect loading, four experimental trials were conducted for each of the two neighboring taxels: a taxel immediately adjacent to the taxel under direct loading and another taxel one unit away (*Figure 2.5*). As expected, the sensitivity to load for the unloaded taxels decreased with distance from the point of load application. The change in capacitance for a given load is much smaller for the unloaded neighboring taxels than that for the taxel under direct loading (*Figure 2.5*). At a load of 2.25 N, the directly loaded taxel had a $\%\Delta V$ value of 20.26%. The adjacent taxel and the taxel one unit away had $\%\Delta V$ values of 5.59% and 2.15%, respectively, which represent reductions in the $\%\Delta V$ values of 72.4% and 89% with respect to the directly loaded taxel. Thus, the sensor prototype has a spatial resolution of approximately 0.5 mm, which would enable precise measurement of bounding areas and center of pressure locations of applied forces.

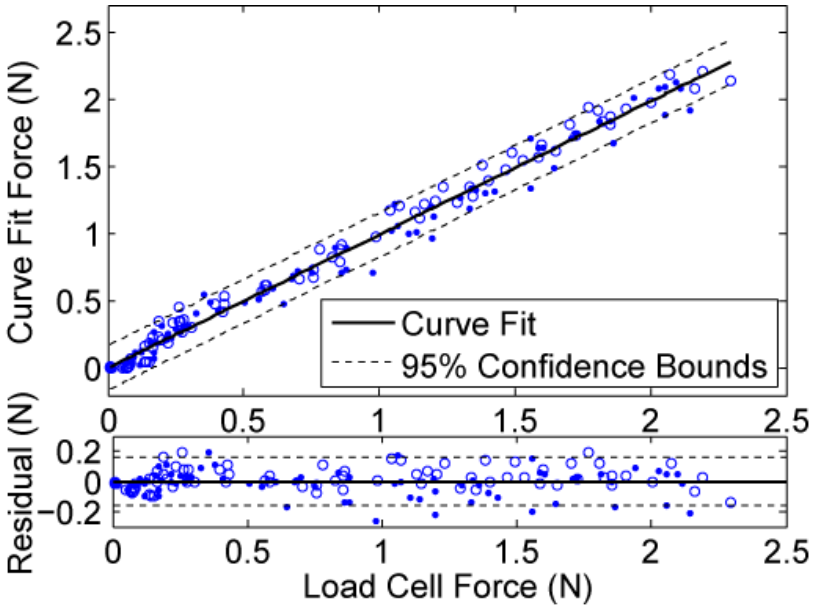

Figure 2.7. Assessment of a single taxel's performance on surfaces with different curvatures. Data collected with the sensor attached to a rigid, flat support plate (solid dots) and wrapped around a rigid, round support dowel (open circles) show similar responses. A single calibration curve (Eqn. 2.6) was used to fit both data sets. A linear regression (solid line, Eqn. 2.7) revealed a near one-to-one relationship between the microfluidic sensor and load cell measurements. The residual plot shows that 10 of 200 data points fell outside the 95% confidence bounds (dashed lines).

Figure 2.7 shows that the sensor performs similarly and reliably whether mounted to flat or cylindrical support surfaces, suggesting that a single calibration curve might suffice. As with the flat surface condition, a sum of two power functions fit the data from the curved surface condition well. The calibration curve for data pooled from the flat and curved surface conditions and the linear

regression of the taxel's curve fit and load cell data are given by the following equations, respectively,

$$F_{fit} = -0.478(\%\Delta V)^{2.00} + 0.506(\%\Delta V)^{1.98},\ R^2 = 0.986, \quad (2.6)$$

$$F_{fit} = 0.99F_{LC} - 0.00454,\ R^2 = 0.986 \quad (2.7)$$

The 95% confidence bounds (±0.165 N) show a force range similar to the one obtained from the previously calibrated taxel (*Figure 2.6*). No major performance difference was observed, suggesting that this particular sensor prototype functions similarly regardless of surface curvature. This finding is likely related to the dimensional relationships between the individual taxels, their spacing, and the curvature of the round support dowel. If small enough, a taxel will act as if mounted to flat surface because even a curved surface will appear locally flat. In addition to the presented results, testing was performed on surfaces with larger curvatures to see if any curvature limits could be detected. The sensor was wrapped around four dowels with radii of 0.397 cm, 0.318 cm, 0.238 cm, and 0.159 cm (curvatures of 2.519 cm^{-1}, 3.145 cm^{-1}, 4.202 cm^{-1}, and 6.289 cm^{-1}, respectively). The sensor tolerated the increased curvature and remained functional as force was applied on a single taxel, further supporting the findings from the finger-sized dowel. These results show that this multilayer microfluidic tactile sensor is flexible and functions well on surfaces having curvatures consistent with artificial fingers and much higher.

SUMMARY

In this work, we have created a functional prototype of a microfluidic normal force sensor that uses a liquid metal alloy for its internal circuitry. The novel use of conductive fluids as deformable capacitive plates and wire paths offers significant advantages over the use of standard solid components such as robustness to cracking and fatigue. The multilayer design utilizing PDMS and air sub-layers allows for the tuning of mechanical and electrical properties, particularly for the heterogeneous, deformable dielectric medium. The sensor also offers advantages such as ease of fabrication, low cost and non-toxic components, large degree of flexibility, robustness, and repeatable measurements. Our work expands the design space for flexible MEMS sensors by demonstrating that liquid metal alloys such as Galinstan can be used as both flexible capacitor plates and wire paths (Hu et al., 2007b; H.-J. Kim et al., 2008). Our microfluidic PDMS sensor remained functional after being wrapped around a surface having a small curvature similar to that of a human finger and showed indications of being capable of measuring low frequency dynamic loads. Additional testing is needed to determine whether the sensor remains functional despite twisting and stretching. Our sensor performed reliably during static loading and unloading trials for forces up to 2.5 N and exhibited 0.5 mm spatial resolution. A functional artificial sensor skin would consist of a larger sensor (eight inch wafers are state of the art) or several of these sensor prototypes covering a large area. Sensing units and sensor resolution can be modified according to the surface area and application of interest.

The primary motivation for this work is tactile sensing for robotics applications. Our current experimental setup and prototype are not well suited for complete dynamic analysis and shear force measurements required for use on an artificial hand. However, it reliably measures normal forces with a spatial resolution appropriate for artificial grasping, is robust, and is flexible in order to be conformally wrapped around curved objects such as artificial fingers. The deformable elastomeric skin could enhance grip by cushioning impacts, increasing the effective contact area, and increasing friction at the hand-object interface during grasp. The sensor's nonlinear response, which can be attributed to its complex mechanical and electrical design, is advantageous for tactile sensing due to its greater sensitivity at low loads and ability to withstand large force ranges. The multilayer design can be modified to tune the nonlinear sensor response according to application-specific design criteria. In addition, MEMS applications that require sensors capable of withstanding elastic deformations, such as bending and stretching, could benefit from replacing rigid metal components with conductive fluids, as described in this work. While the sensor skin was initially conceived for robotic hands, the sensor could easily be applied to other robotic and haptic applications. For instance, the skin could be applied to large surface areas (e.g., wrapped around robot arms (Mukai, Onishi, Odashima, Hirano, & Zhiwei Luo, 2008)) for safe human-robot interactions, or applied to human-machine interfaces for haptic applications.

Our future work will focus first on enhancing the experimental setup for complete dynamic characterization of the sensor skin. We will also implement

multiplexing of the data collection circuitry to enable simultaneous measurement of signals from multiple taxels to identify features of loads such as center of pressure location. A common challenge for capacitive sensors is noise due to proximity to external sources of electromagnetic interference. One potential solution for ensuring acceptable signal to noise ratios is to use commercially available electromagnetic noise shielding films (e.g. SF PC5000 (Tatsuta Film)) used on printed circuit boards of cell phones and digital video cameras.

In addition, coupled physics finite element models will be developed such that the sensor design (e.g., thickness of PDMS layers, dimensions and placement of air pockets, etc.) can be tuned for specific sensing design requirements (e.g., range, dynamic response). Previous works (Hyung-Kew Lee et al., 2008; Koterba & Matsuoka, 2006) have demonstrated that arrays of normal force sensing units can be used to approximate shear by simply adding bumps or pillars on the exposed PDMS surface and looking at the relative signal response between adjacent sensing elements. Similar strategies could be attempted with our microfluidic force sensor to expand the sensing capabilities to include shear forces.

CHAPTER 3

HAPTIC EXPLORATION OF EDGES WITH RESPECT TO A FINGERTIP-FIXED REFERENCE FRAME USING A MULTIMODAL TACTILE SENSOR

INRODUCTION

The intimate connection between an amputee and his or her upper limb prosthesis brings together two complex systems that speak different languages at different timescales. Communication delays inherent to human-machine systems result from the necessary translation between the biological and artificial systems for both afferent and efferent signals (Cipriani et al., 2009). The cognitive burden on an amputee can be minimized by making the prosthesis more intuitive to use and minimizing the details that the amputee must consider in light of such delays. Subtle details of control include determining which of the multitude of joints to actuate, when and how hard to grasp an object, and how to adjust fingertip forces to maintain a stable grasp during object use.

Invasive techniques such as targeted muscle reinnervation (Schultz, Marasco, & Kuiken, 2009), peripheral nerve stimulation (Dhillon & Horch, 2005), and intracortical microstimulation (O'Doherty et al., 2011; Overstreet, Klein, & Helms Tillery, 2013; Romo, Hernández, Zainos, & Salinas, 1998) hold the promise of bringing a conscious perception of tactile feedback to the user and increasing the number of channels with which a user can intuitively control a high degree-of-freedom (DOF) prosthesis (see (Belter & Dollar, 2011) for a nice review of anthropomorphic prosthetic hands). Even when such techniques become

clinically viable and commonplace, amputees may still not be able to respond quickly enough through the human-machine interface to counter unexpected perturbations or perform tasks requiring quick dexterous adjustments.

Amputees could benefit from the use of a "sense-think-act" circuit (M. Siegel, 2003) within the prosthesis itself that automatically addresses millisecond-to-millisecond details of finger-object actions, and buys time for cognitive processing and generation of a voluntary response. Complex behaviors could also be semi-automated so that the user could focus on high level decisions so long as the semi-automation is context-appropriate, reliable, and does not alienate the user.

Currently, amputees who use commercially available upper extremity prostheses rely solely upon visual feedback when physically interacting with others or objects in their environment (Cipriani et al., 2009). Visual feedback can provide preliminary information about an object that can be used to pre-shape grasp (Ciocarlie & Allen, 2008) and plan digit placement (Miller & Allen, 2004). However, visual feedback alone cannot provide all essential information for successful physical hand-object interactions. This is especially true when object scenes are cluttered, pre-planned digit placement is erroneous when executed, digits are occluded by the grasped object itself, or when the hand-object interaction is completely out of view. Everyday examples include searching for a light switch in the dark, wrapping a belt around oneself, or reaching for a cellphone in one's pocket.

Reliance upon visual feedback alone is also challenging for unimpaired individuals because many activities of daily living do not afford a complete line-of-sight or require precise control of fingertip forces whose effects are unseen. Performance of activities of daily living with a prosthesis requires extensive concentration which can be mentally taxing, especially for a bilateral amputee who cannot compensate for a missing limb with an unimpaired limb. A survey of amputees who use transradial electric-powered prostheses reiterated that they would prefer that less visual attention be required to perform functions (Atkins, Heard, & Donovan, 1996). This desirable feature was ranked third out of 17 choices, behind basic kinematic preferences for fingers that can bend and a thumb that can move out to the side.

A study on three-dimensional (3D) haptic shape perception investigated the influence of object features such as curvature, aspect ratio, and edges on the ability of unimpaired subjects to quickly and accurately identify objects through touch alone (Plaisier et al., 2009). Subjects were allowed to use a variety of "exploratory procedures" (EP) (Lederman & Klatzky, 1987) in order to extract object properties. One conclusion of the study was that edges and vertices were the most salient local features of 3D shape and that haptic searches were performed efficiently when the target object had edges (Lederman & Klatzky, 1997; Plaisier et al., 2009).

Given the usefulness of edges in human studies on shape perception, it could be worthwhile to develop artificial capabilities for edge perception in artificial systems, such as prosthetic or robotic hands. While enclosure could be

used for estimating global shape, enclosure has yet not been used for edge perception by artificial hands, possibly due to limitations in tactile sensing technology. Rather, enclosure has been used to simplify the grasp planning problem, particularly with underactuated hand designs (e.g., (Ma, Odhner, & Dollar, 2013; Massa, Roccella, Carrozza, & Dario, 2002)). Contour-following has been demonstrated for industrial applications, but simultaneous force and vision sensing were required (Johan Baeten, Verdonck, Bruyninckx, & De Schutter, 2000; Koch, Konig, Weigl-Seitz, Kleinmann, & Suchy, 2013). Edge detection has been demonstrated for artificial fingers, but the typical approach of using raster-like patterns of static contact with the object to build a composite "tactile image" (Berger & Khosla, 1991; H.-K. Lee et al., 2006; Mei et al., 2000; Petriu, McMath, Yeung, & Trif, 1992) does not reflect strategies used by humans (Huynh, Stepp, White, Colgate, & Matsuoka, 2010; Plaisier et al., 2009).

Whether conveying a sense of touch to an amputee or making a split-second semi-autonomous decision on the amputee's behalf, a prosthesis must have an ability to relate finger-object interactions to a hand-centric reference frame. The objective of this work was to use a multimodal tactile sensor to establish the orientation of a salient local feature of an object (an edge) with respect to a body-fixed reference frame in the artificial finger through haptic exploration. The ability to predict edge orientation with respect to the fingertip through active touch could enable task-appropriate manipulations of an object and complex exploratory procedures such as contour-following (Lederman & Klatzky, 1987) in the absence of visual feedback.

METHODS

Apparatus

Robot testbed. The robot testbed consists of a 7 degree-of-freedom Barrett Whole Arm Manipulator (WAM) and BarrettHand (Barrett Technology, Cambridge, MA) in which the middle digit has been outfitted with a BioTac sensor (SynTouch, Los Angeles, CA) (*Figure 3.1*). The BioTac enables simultaneous measurement of multiple tactile sensing modalities that mimic slow- and fast-adapting mechanoreceptors in the human fingertip and has been used to identify material type (Lin, Erickson, Fishel, Wettels, & Loeb, 2009), compliance (Su et al., 2012), and texture (J. A. Fishel & Loeb, 2012), to relate haptic adjectives to objects (McMahon et al., 2012), and to identify objects (Xu et al., 2013). The multimodal tactile sensor consists of a fingertip-shaped rigid core that houses an array of 19 electrodes, a pressure sensor, and a thermistor (Nicholas Wettels et al., 2008). An elastomeric skin, patterned externally with fingerprint-like ridges surrounds the rigid core (J. A. Fishel & Loeb, 2012). A weakly conductive fluid injected between the core and elastic skin serves as the fluidic mechanotransduction medium.

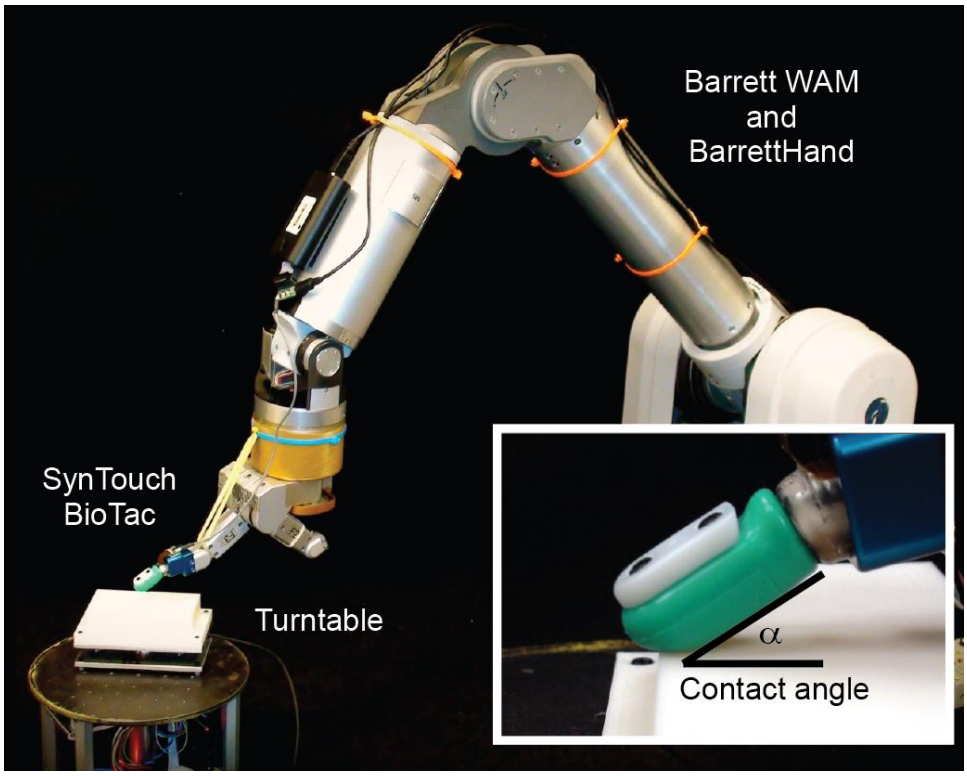

Figure 3.1. Experimental setup for the edge characterization study. The Barrett WAM, BarrettHand, and BioTac were used to explore edge stimuli presented at random orientations with respect to the fingertip reference frame by a motor-driven turntable.

While the mechanotransduction mechanisms differ from those of the human fingertip, the electrodes of the BioTac serve as low spatial resolution proxies for SA I Merkel's endings, slowly adapting cutaneous mechanoreceptors in the human finger that respond to local, low-frequency skin deformations (Johansson & Flanagan, 2009). At low sampling rates, the pressure sensor serves as a proxy for SA II Ruffini-like endings, slowly adapting mechanoreceptors that respond remotely to static forces. At high sampling rates, the pressure sensor

mimics the dynamic range (but not the spatial resolution) of FA I Meissner endings and FA II Pacini endings, fast-adapting mechanoreceptors in the human fingertip that respond to high frequency vibrations and mechanical transients (J. A. Fishel & Loeb, 2012; J. Fishel & Loeb, 2012).

We recorded tactile signals related to elastomeric skin deformation relative to the rigid core (1 impedance sample from each of 19 electrodes), overall internal fluid pressure (1 sample), and fluid vibration (22 samples) for each 10 ms batch of data. The effective sampling rates are 100 Hz for electrode impedance and overall fluid pressure, and 2200 Hz for vibratory signals (J. Fishel, Lin, & Loeb, 2013). Temperature data were not used in this work.

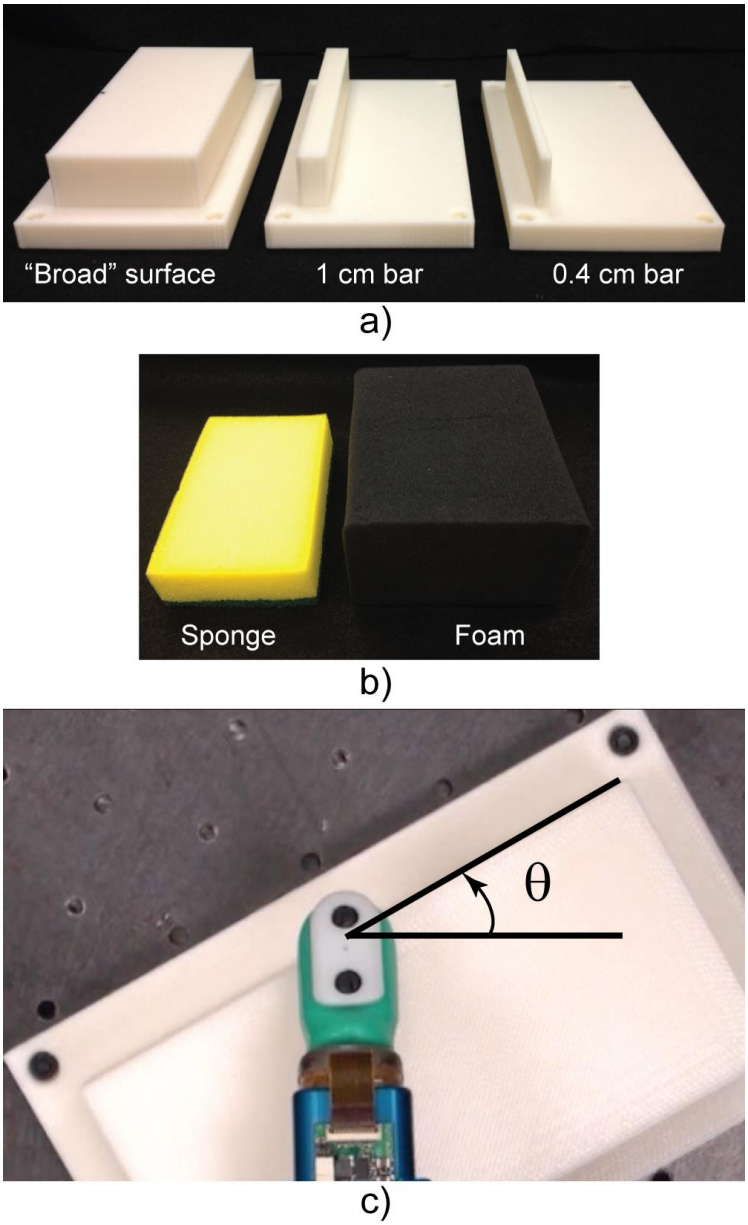

Figure 3.2. Tactile stimuli used during the study on characterization of edge orientation. a) Study 1: Rigid edge stimuli of three different widths were presented at c) different orientation angles θ with respect to a body-fixed fingertip reference frame. b) Study 2: Compliant edge stimuli shown (L-R) in order of increasing stiffness.

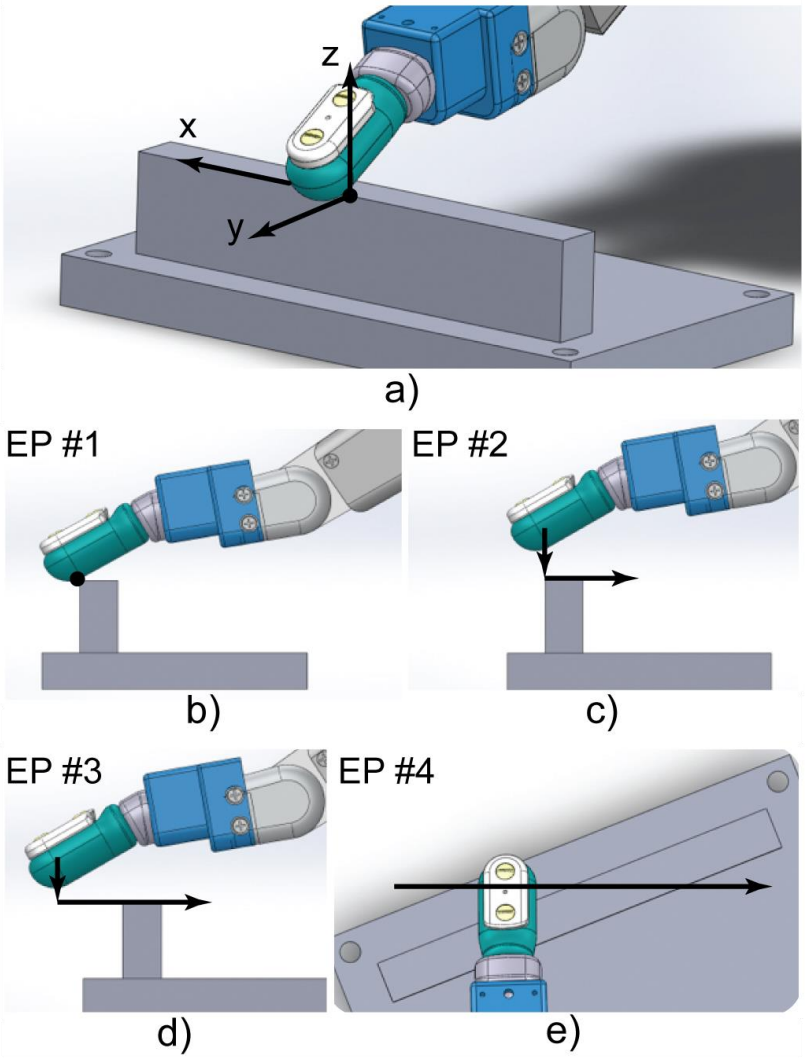

Figure 3.3. The different exploratory procedures implemented to explore an edge. . a) During each exploratory procedure, the WAM maintained a constant BioTac contact angle relative to the horizontal x-y plane. b) EP #1: static contact, c) EP #2: distal to proximal stroke with an approach normal to the stimulus surface, d) EP #3: distal to proximal stroke with an approach tangential to the stimulus surface, and e) EP #4: radial to ulnar stroke.

Tactile stimuli. We hypothesized that the multimodal tactile sensor would encode the orientation angle θ of an edge with respect to a body-fixed reference

frame in the artificial finger. For instance, exploratory movements perpendicular to an edge might generate subtle vibrations at the skin-object interface with a different frequency "signature" than those generated by movements aligned with an edge, just as subtle vibrations associated with sharpness have been related to FA I responses (Robert H. LaMotte & Srinivasan, 1987).

In order to develop a generalizable Support Vector Regression (SVR) model capable of estimating edge orientation regardless of surface width, we collected data for three different surface widths using rigid stimuli *(Study 1)*. Three 2 cm-tall, 3D printed (ABS plastic), rigid edge stimuli were used: a 5 cm-wide "broad surface," a 1 cm-wide "thick rectangular bar," and a 0.4 cm-wide "thin rectangular bar," (*Figure 3.2*a). Each stimulus was rigidly attached to a 6 DOF load cell (ATI Nano-17), which was attached to a steel turntable. In a brief follow-up experiment *(Study 2)*, we collected data for two compliant broad surfaces: a polyurethane sponge and a foam block (*Figure 3.2*c). Velcro strips were used to affix the compliant stimuli to the steel turntable.

A DC motor (Maxon Precision Motors, Inc., EC-max 30) and motor controller (Maxon EPOS2 24/5) were used to orient edges in the horizontal plane at angles ranging from -90° to 90° (quadrants I and IV) in 1° increments. Edge orientation was randomized in order to minimize possible effects of skin wear or other latent variables on the SVR model. Experimental results with angles in quadrants II and III were presumed to be symmetric about the longitudinal axis of the artificial finger and were not investigated. Edge orientation angles were

measured relative to a positive x-axis (0°) pointing in the ulnar direction of a right-hand index finger (*Figure 3.2*c, *Figure 3.3*a).

For each trial, the motor rotated the edge to a prescribed angle with a resolution of 1/2000 counts per revolution, or 0.18°. Just prior to BioTac contact with the stimulus, a pair of electromagnets were activated to lock the turntable position and trigger the temporary powering down of the DC motor. This was done to minimize electromagnetic noise pollution of the 6 DOF load cell data by the nearby DC motor.

Exploratory procedures. Joint space control of the WAM was used to prescribe the trajectory of the BioTac fingertip and its orientation using Barrett Technology's internal C++ library ("libbarrett"). In Study 1, four exploratory procedures were used: 1) static contact with a normal contact force along the z-axis, 2) distal to proximal linear stroke along the y-axis with an approach normal to the stimulus surface, 3) distal to proximal linear stroke along the y-axis with an approach tangential to the stimulus surface, and 4) radial to ulnar linear stroke along the x-axis (*Figure 3.3*). A fixed global reference frame was defined directly above the center of the turntable with its origin placed at the contact height of the stimulus and its x-y plane coincident with the stimulus surface. Axes were defined such that radial to ulnar and distal to proximal fingertip motions could be expressed in terms of x- and y-coordinates while fingertip height could be expressed in z-coordinates (*Figure 3.3*a). Note that this reference frame was adopted for position control of the fingertip because of the nonzero contact angle α of the finger (*Figure 3.1*). Otherwise, a literal distal to proximal movement of

the fingertip would simply result in the immediate loss of contact with the stimulus.

For EP #1 (*Figure 3.3*b), the fingertip was pressed against the edge of the stimulus, at the origin of the global reference frame, at a constant nominal force in the -z direction for a "hold" period of 1.5 sec. For EP #2 (*Figure 3.3*c), the fingertip approached the edge along the z-axis (normal to the surface), made contact with the edge, and then swept across the edge in the -y direction. For EP #3 (*Figure 3.3*d), the fingertip approached the edge from a location distal to the edge along the y-axis (tangential to the surface), and then swept across the edge in the -y direction. For EP #4 (*Figure 3.3*e), the fingertip swept across the stimulus in the ulnar direction along the x-axis. However, the nature of the initial finger-stimulus contact for this EP varied according to edge orientation and surface width. For example, relatively steep negative edge orientations (e.g., -75°) were such that, for thin and thick bars, initial contact was tangential to the stimulus surface while, for broad surfaces, initial contact was normal to the stimulus surface before eventually losing contact with the stimulus. For relatively steep positive edge orientations (e.g., +75°), initial contact with the broad surface was tangential to the stimulus surface and the trial ended with the fingertip still in contact with the stimulus.

A linear stroke of constant speed was used to investigate the quality of tactile information gleaned from a simple motion, as opposed to complex fingertip trajectories or raster-like scanning patterns (Huynh et al., 2010). EP #2 and #3 fingertip trajectories used velocities of v_y = -2 cm/s or -4 cm/s. For EP #2, initial

contact always occurred at the origin of the global reference frame (*Figure 3.3*a) and was followed by a 4 cm stroke in the -y direction. Initial contact for EP #3 occurred at different locations along the edge of the stimulus, depending on edge orientation. However, as with EP #2, the stroke trajectory of EP #3 ended at y = -4 cm. EP #4 fingertip trajectories used velocities of v_x = +2 cm/s or +4 cm/s and were 8 cm long (started at x = -4 cm and ended at x = +4 cm). Scanning speeds were inspired by non-human primate and human subject experiments on sensing and perception of stimulus orientation in which bars and edges were scanned linearly across a passive fingerpad at speeds of 1, 2, 4, and 8 cm/s (S. J. Bensmaia et al., 2008; Sliman J. Bensmaia et al., 2008).

For all four exploratory procedures, the BioTac was oriented at either a 20° or 30° contact angle α with respect to the horizontal x-y plane (*Figure 3.1*). A 30° contact angle was prescribed such that the cluster of four electrodes on the flat face of the BioTac (*Figure 3.4*, Cluster 1) would be parallel to the surface to be explored (*Figure 3.1*, *Figure 3.4*). After a preliminary study, it was hypothesized that a shallower contact angle such as 20° might stimulate a wider range of electrodes, particularly on the proximal aspect of the BioTac.

For the 30° contact angle, the sensor was swept across each stimulus for all four EPs at one of two constant commanded heights from the stimulus surface (z = -4 mm or -6 mm) in order to examine two different nominal contact forces. Fingertip displacements were selected to ensure that the BioTac skin would deform substantially as it swept over each stimulus. A commanded height of z = -4 mm only was used for the 20° BioTac contact angle since a preliminary study

showed that SVR model performance was unaffected by the magnitude of the applied force. This also minimized potential, unnecessary wear of the BioTac skin.

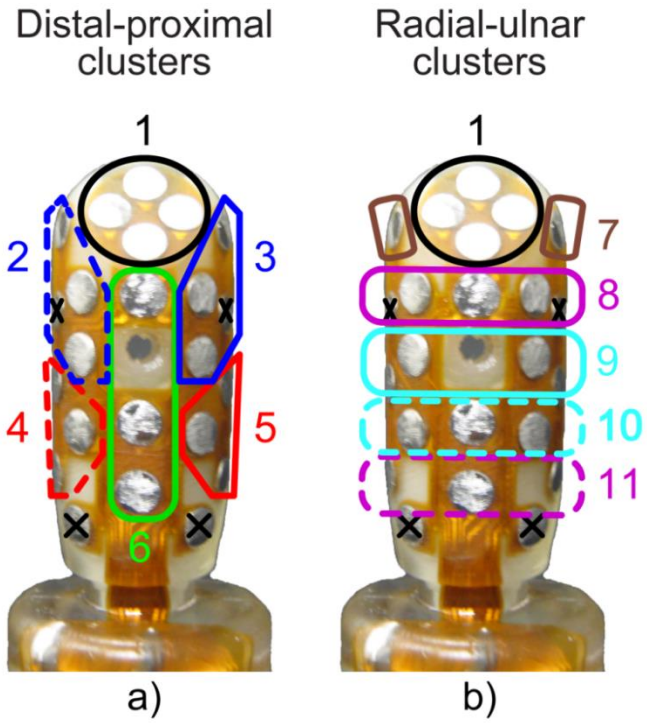

Figure 3.4. Clusters of BioTac electrodes based on their spatial location on the rigid core. Considering the BioTac as a right-hand index finger, palmar views of two type of clusters are shown: a) clusters oriented along the distal-proximal axis and b) clusters oriented along the radial-ulnar axis.

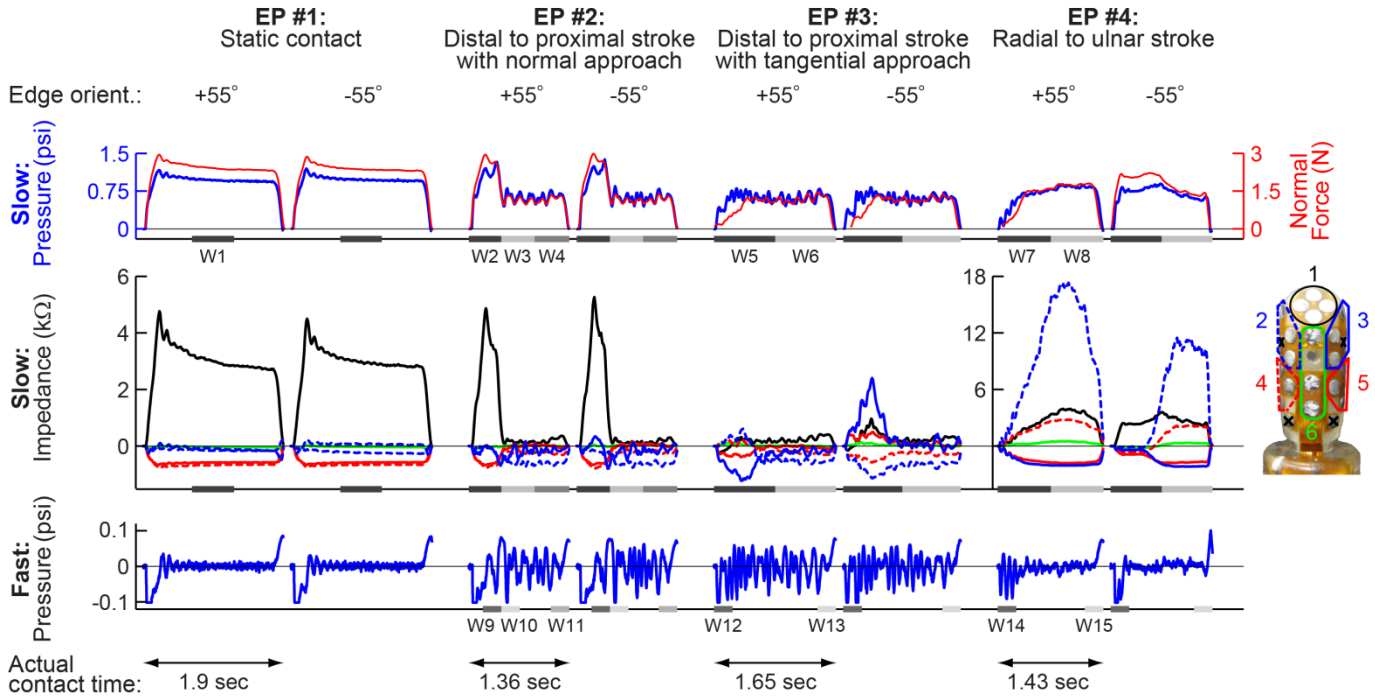

Figure 3.5. Representative multimodal tactile data for edge orientations of +55° and -55° for a rigid broad surface, contact angle of 30°, commanded displacement of z = -4 mm, and scanning speed of 4 cm/s. Overall fluid pressure (row 1, blue) was used to determine initial contact and loss of contact. Inputs to the SVR model were calculated from windows of time (W1-W15) that were specific to each exploratory procedure.

For Study 2 with the compliant stimuli, only EP #1 and EP #3 were used. The contact angle α was 30°, stroke speed was 4 cm/s, and the commanded height was z = -6 mm.

Processing of tactile sensor data. Similar to the human fingertip, the BioTac is sensitive to both sustained (slow) and transient (fast) stimuli. We hypothesized that key information about finger-object interactions would be encoded in both slow and fast tactile signals during different phases of each contact. Thus, different "windows" of tactile data, specific to the exploratory procedure, were used to train the SVR model.

Overall fluid pressure. For each trial, a threshold of a 3% increase from baseline overall fluid pressure was used to determine initial contact and loss of contact. Since the SVR model was to be based on stimuli having different surface widths, contact time was normalized by converting each contact period into a percentage where 0% and 100% denoted initial contact and loss of contact, respectively.

For EP #1 (static contact), the middle 30% of contact ("window 1" or W1) was used to calculate inputs to the SVR model (*Figure 3.5*). It was observed that EP #2 (normal approach, *Figure 3.3*c) generated tactile data that resembled the concatenation of a static contact (as with EP #1) followed by a stroking motion. As a result, data from the stroke with the normal approach were split into three windows: brief static contact (W2), first half of the remaining motion (W3), and second half of the remaining motion (W4). For EP #3 and #4, the data were split into two equal windows of contact (W5 and W6 for EP #3, W7 and W8 for EP

#4). Windows were selected in order to capture coarsely the trends during each contact period (sustained values during static contact, dynamics at the start and end of strokes).

A mean overall pressure value was calculated for each window of time W1-W8 for use as inputs to the SVR model. In addition, rates of change were provided to the model. Fluid pressure data were low-pass filtered with a 2nd order Butterworth filter having a cut-off frequency of 10 Hz prior to numerical differentiation. Mean rates of change were calculated for the brief period of initial contact (first 25% of windows W2, W5, and W7).

Skin deformation. In an independent study, a cluster of four electrodes on the fingertip and a lateral electrode enabled estimation of material compliance (Su et al., 2012). Thus, although the BioTac provides independent impedance values for each of 19 electrodes, we used clusters of electrodes defined according to spatial location on the fingertip and either oriented along the distal-proximal axis (*Figure 3.4*a) or along the radial-ulnar axis (*Figure 3.4*b).

Mean electrode impedances were calculated for each cluster (for windows W1-W8) in order to reduce the number of inputs of the SVR model, problem complexity, and computational expense. Rates of change for each cluster were also provided to the model using the methods previously described for determining the rates of change in overall fluid pressure. Ratios of electrode impedance values were considered, but preliminary analyses suggested that model performance did not improve despite the additional model inputs. Therefore, potentially redundant ratio data were not used in this work.

Fluid vibration. With the exception of EP #1 (static contact), each window of fluid vibration data was analyzed using a Hilbert-Huang Transform (HHT) (Huang, 2005; Huang et al., 1998). Like the Fast Fourier Transform (FFT), the HHT converts data from the time domain to the frequency domain. While HHT is more computationally intensive than FFT, a major advantage is that HHT is applicable to data sets that do not satisfy assumptions of linearity and stationarity (Donnelly, 2006). The transient and discontinuous nature of the tactile data generated from a stroke across an edge, for example, makes the HHT a more appropriate frequency analysis technique for this work than FFT.

The HHT process deconstructs the original signal into intrinsic mode functions (IMFs), each of which has its own energy content and frequency spectrum, by applying Empirical Mode Decomposition. The first IMF component contains the highest frequencies of the original signal, the second IMF contains the next highest frequencies, and so on (Huang et al., 1998; W. Liu, Yan, & Wang, 2011).

Hypothesizing that information related to edge orientation might be encoded in the high frequency range, we selected the first IMF for extracting input parameters for the SVR model for EP #2, #3, and #4. For EP #2, an attempt was made to capture the dynamics at the start and end of the stroke by defining windows W9, W10, and W11 as the last 250 ms of W2, the first 250 ms of W3, and the last 250 ms of W4, respectively (*Figure 3.5*). For EP #3 and #4, the dynamics at initial contact and loss of contact were investigated. Windows W12 and W13 were defined as the first 250 ms of W5 and the last 250 ms of W6,

respectively, for EP #3 while W14 and W15 were defined as the first 250 ms of W7 and the last 250 ms of W8, respectively, for EP #4. For those cases (e.g., thin bar) in which windows W9-W15 may have been shorter than 250 ms in duration, the entire window of data was used. For each of windows W9-W15, the mean instantaneous frequency of the first IMF was used as an input to the SVR model.

Support vector regression model. A support vector machine (SVM) is a well-established supervised learning technique for classification and regression, with advantages such as robustness to outliers and convergence to a global minimum, and great applicability to a wide range of types of data (Tan, Steinbach, & Kumar, 2006). To enhance the practical utility of our work, we elected to develop a support vector regression model that estimates a value from a continuous number line as opposed to a support vector classifier. While useful, a support vector classified is limited in that it will simply identify a single class from a limited set of discrete classes selected *a priori* which may not generalize to data on which the classifier was never trained. Cross-validation is used during the model-building process to evaluate the effects of learning parameters. Models can then be built with the selected learning parameters and user-specified input parameters. Model performance is assessed using an entirely novel test data set that was not used during the training or building of the model.

For Study 1 with rigid stimuli, we collected two trials of tactile data for each of 181 randomized edge orientations and for each of 18 distinct block conditions (three stimuli surface widths, two contact angles, two stroke speeds, two commanded displacement heights for the 30° contact angle and one height for

the 20° contact angle). Each individual trial consisted of data resulting from all four exploratory procedures. For each block condition, data were split randomly into a training set (~90% of total trials) and test set (~10% of total trials). Ultimately, 5849 trials were used for training an SVR model while 648 trials were saved for testing of the final model. Cross-validation to select learning parameters (kernel function, complexity term) was performed on the training data only.

For Study 2 with compliant stimuli, three distinct block conditions were evaluated (three materials having different compliance levels, one surface width (broad), one contact angle, one stroke speed, one commanded displacement height). The two compliant stimuli were a polyurethane sponge and a foam block (*Figure 3.2*). The third stimulus was the rigid, 3D printed (ABS plastic) "broad surface" from Study 1. Each individual trial consisted of tactile data resulting from EP #1 and EP #3. A total of 1301 trials were used for training an SVR model while 144 trials were saved for testing of the final model.

When building the SVR models using Weka (Hall et al., 2009), we considered up to 85 input parameters (Table 3.1). Besides the tactile signals described previously, stroke speed was used as an input parameter because of the relationships that presumably exist between active fingertip motions (easily quantified for robotic systems) and sensations elicited at the fingertip. Normal contact forces and contact angles were left out of the SVR models as these parameters would depend on the compliance and shape of the object and would likely be unknown in practice.

Table 3.1

SVR Model Input Parameters

Type of info	Input to SVR model	EP #1 (static contact)	EP #2 (distal to proximal stroke – normal)	EP #3 (distal to proximal stroke - tangential)	EP #4 (radial to ulnar stroke)
Voluntary motion	Stroke speed	---	(1) Single value for entire trial		
Slow tactile signals	Overall fluid pressure	(1) W1	(3) W2-W4	(2) W5, W6	(2) W7, W8
	Initial rates of change of overall fluid pressure	---	(1) W2	(1) W5	(1) W7
	Electrode impedance	(6) W1 for Clusters 1-6	(18) W2-W4 for Clusters 1-6	(12) W5, W6 for Clusters 1-6	(12) W7, W8 for Clusters 1-6 *or* 1,7-11
	Initial rates of change of electrode impedance	---	(6) W2 for Clusters 1-6	(6) W5 for Clusters 1-6	(6) W7 for Clusters 1-6 *or* 1,7-11
Fast tactile signals	Instant. freq. (of 1st IMF) of vibrations	---	(3) W9-W11	(2) W12, W13	(2) W14, W15

Note. Parenthetical values in red indicate the number of inputs for each type of parameter.

RESULTS

Tactile data

Study 1 with rigid stimuli. Representative multimodal tactile sensor signals are shown in *Figure 3.5* for all four exploratory procedures for two different edge orientations that are symmetric about the radial-ulnar x-axis: +55° and -55°. Baseline (pre-contact) values were subtracted for all tactile signals on a trial-by-trial basis. For each exploratory procedure, the overall fluid pressure (*Figure 3.5*, row 1, blue) and normal contact force (*Figure 3.5*, row 1, red) increase and decrease as would be expected with initial contact and loss of contact, respectively. The stroking motion of the fingertip results in lower overall fluid pressures (*Figure 3.5*, row 1, W3-W8) and increased fluid vibration amplitudes (*Figure 3.5*, row 3). Interestingly, despite their nearly identical distal to proximal fingertip motions, EP #2 and #3 generated qualitatively different tactile signals due to their different approaches to the stimulus surface (normal or tangential, respectively).

Each of the clusters of electrodes measures skin deformation near a specific region of the BioTac's 3D, curved core. For the distal-proximal clusters (*Figure 3.4*a) whose data are presented in *Figure 3.5*, clusters that were not located along the long axis of symmetry of the sensor (clusters 2-5) displayed an asymmetric response in electrode impedance values for EP #3. Compression of the skin against the rigid core resulted in an increase in impedance on one side of the finger, such as the radial aspect for a -55° orientation. This trend was mirrored by a simultaneous bulging of the skin away from the rigid core and resulted in a

decrease in impedance on the other side of the finger, such as the ulnar aspect for the -55° orientation (*Figure 3.5*, dashed lines in row 2). For EP #4 (radial to ulnar stroke), shear forces caused a compression of the skin against the rigid core on the ulnar aspect and a bulging of the skin on the radial aspect.

Study 2 with compliant stimuli. The stiffness of the two compliant stimuli (sponge, foam) and the BioTac (inflated with fluid according to the vendor's specifications) were quantified using a custom setup. Shore 00 durometers are typically used to measure the hardness of soft materials such as gels and rubbers. However, the stimuli in this study have hardness values that fall well below the Shore 00 durometer's sensing range. In addition, the small measurement tip would penetrate the sponge and foam's porous surfaces, resulting in erroneous indentation readings of zero.

Our custom setup was constructed with a CNC mill dial indicator with a resolution of 0.001 inches (Part #2925, Little Machine Shop, Pasadena, CA) (Figure A.1). The flat face of the cylindrical 5.5 mm diameter dial indicator tip was indented into the sponge and foam samples with calibrated masses. The indentation is allowed to stabilize for at least 5 minutes before the tip's displacement from the unindented surface height was recorded. The mass of the indicator tip was 50 g, which served as the smallest mass that could be applied to the compliant samples. Additional calibrated masses of 20, 50, 100, 150, and 200 g were used. The resulting displacement versus mass curves are shown in *Figure 3.6*. The BioTac skin was much stiffer than the sponge or foam.

Haptic exploration of the compliant stimuli (*Figure 3.7*) resulted in trends different from those for the rigid stimuli (*Figure 3.5*). In addition, for both exploratory procedures (EP #1 and EP #3), the amplitudes of all tactile signals were much smaller for the compliant stimuli than for the rigid, broad surface stimulus. In contrast with Study 1, the difference in stiffness between the edge stimuli and the BioTac skin was much less in Study 2. In Study 2, both the BioTac and compliant edge stimuli deformed during loading, resulting in conformation of the compliant stimuli around the fingertip, less overall skin deformation, and electrode impedance values that were approximately an order of magnitude less than those for the rigid stimulus.

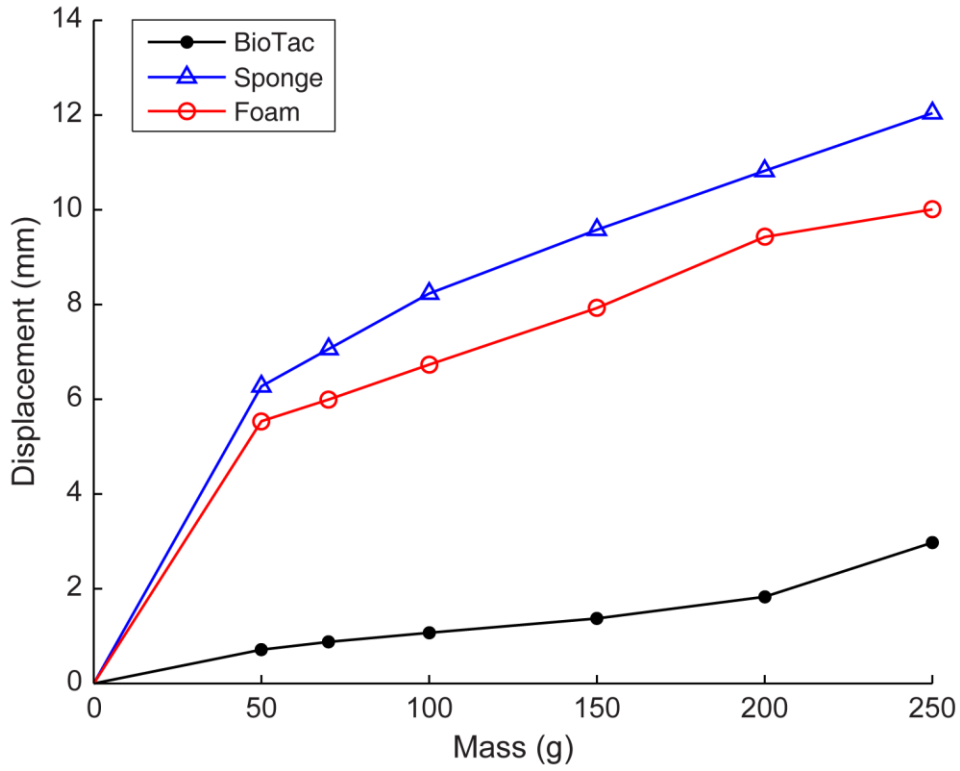

Figure 3.6. Compliance curves for the soft stimuli. The BioTac was stiffer than the sponge and foam, but was still compliant itself.

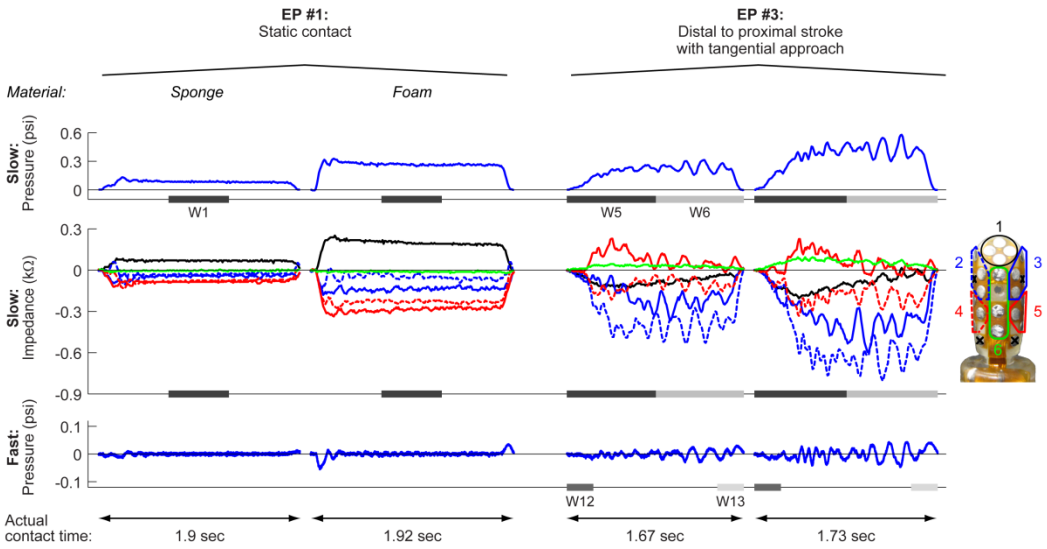

Figure 3.7. Representative multimodal tactile data for edge orientations of +55° for the sponge and foam block. The contact angle was 30°, stroke speed was 4 cm/s, and the commanded height was z = -6 mm.

Model performance

Study 1 with rigid stimuli. From cross-validation observations, the kernel function and complexity term of the SVR model were set to a quadratic polynomial and a value of 1, respectively. The low model complexity term minimizes overfitting of the model to the training data. Despite the low complexity of the model, these learning parameter settings yielded accurate predictions (Table 3.2).

An SVR model using all 85 inputs took approximately 20 hours and 5 min to be trained and built on a PC with two Intel Xeon 2 GHz quad core processors. Once the regression model was built, predictions on all 648 trials of test data set took approximately 4 sec total.

When all 85 inputs were used in the SVR model, a regression of the model predictions on the true edge orientations for the test data set yielded an R^2 of 0.991 (Table 3.2, *Figure 3.8*). The user can decide whether it is more important to have a complex regression model with many input parameters and a high level of accuracy or a simpler regression model with acceptable accuracy. Appealing model options, based on accuracy with respect to the number of input parameters, appear in red in Table 3.2.

Table 3.2

Edge Characterization Study 1: SVR Model Performance Using Different Sets of Inputs

Focus of Comparisons	EP #	# of Inputs	R^2	Mean abs. error (°)	RMS error (°)
Exploratory procedures (using all available input parameters for each EP)	1-4	85	0.991	2.893	5.076
	1	7	0.441	30.719	39.685
	2	32	0.712	18.531	28.409
	3	24	0.960	5.177	10.668
	4	24	0.725	17.338	27.908
	3, 4	47	0.980	3.457	7.511
Removal of scanning speed, overall fluid pressure, and vibration inputs	1-4	66	0.987	3.205	6.114
	3	18	0.931	6.632	4.015
	4	18	0.686	19.258	29.800
Removal of initial rates of change of overall fluid pressure and electrode impedance*	1-4	48	0.858	12.720	19.904
	3	12	0.795	15.892	24.091
Removal of specific distal-proximal clusters (*Figure 3.4*a)*					
- Centerline (Clusters 1, 6) removed	3	12	0.784	16.991	25.093
- Ulnar aspect (Clusters 2, 4) removed	3	12	0.792	16.902	24.102
- Radial aspect (Clusters 3, 5) removed	3	12	0.777	17.679	25.095
Radial-ulnar clusters (*Figure 3.4*b)					
- All available input parameters	4	24	0.709	17.724	28.836
- Electrode impedance values only*	4	18	0.500	26.157	37.353

Note. Appealing models based on accuracy with respect to the number of input parameters are shown in red. EP#3 and electrode impedance signals provided the most useful inputs for this edge orientation perception task.

*With scanning speed, overall fluid pressure, and vibration inputs also removed.

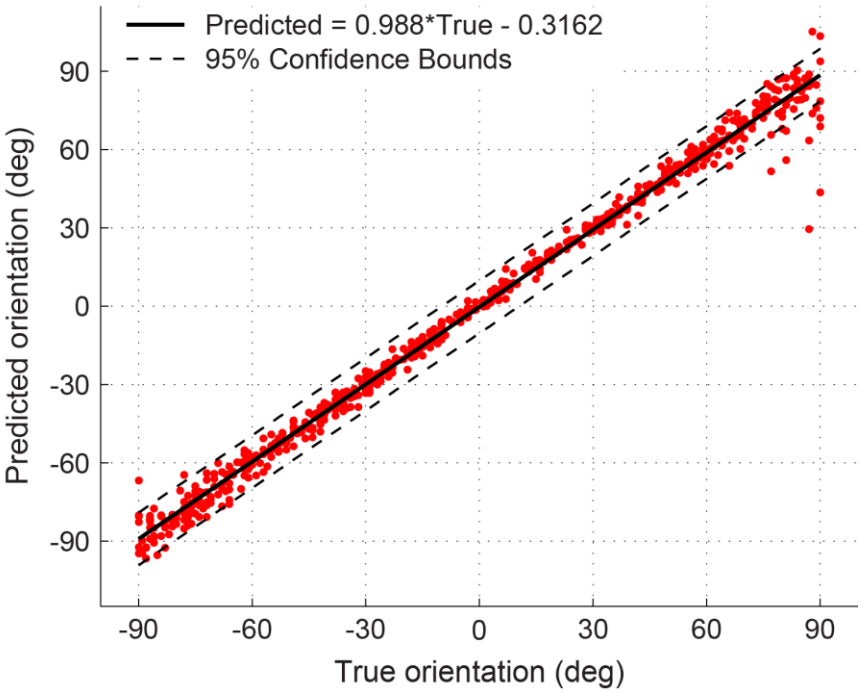

Figure 3.8. Study 1 edge orientation predictions from an SVR model using all 85 inputs. The model performed well on the test data set (648 trials, ~10% of total trials, R^2 of 0.99, RMS error of 5.08°), which included various edge orientations, stimulus widths, normal contact forces, contact angles, and scanning speeds.

Study 2 with compliant stimuli. Training and building an SVR model using only inputs from EP #3 took approximately 37 seconds. Predictions on the test data set with the trained SVR model took less than 1 second for all 144 trials. Using all 24 EP #3 inputs, a regression on the prediction of the true orientations resulted in a resulted in an R^2 of 0.958 (Table 3.3, *Figure 3.11*).

Table 3.3

Edge Characterization Study 2: SVR Model Performance Using Different Sets of Inputs

Data Set	EP #	Kernel Order	# of Inputs	R^2	Mean abs. Error (°)	RMS error (°)
Sponge #1	1	1	7	0.974	6.402	8.547
	1	2	7	0.980	5.306	7.624
	3	1	24	0.984	4.215	6.561
	3	2	24	0.980	3.526	7.484
Foam Block	1	1	7	0.961	8.089	10.319
	1	2	7	0.975	5.356	8.057
	3	1	24	0.995	3.390	3.980
	3	2	24	0.999	1.523	2.043
ABS	1	1	7	0.803	16.964	23.287
	1	2	7	0.885	13.065	17.720
	3	1	24	0.991	3.106	4.924
	3	2	24	0.994	2.127	4.002
All three	1	1	7	0.539	27.114	37.600
materials	1	2	7	0.891	13.543	17.814
	3	1	24	0.719	20.091	27.630
	3	2	24	0.954	5.683	11.299

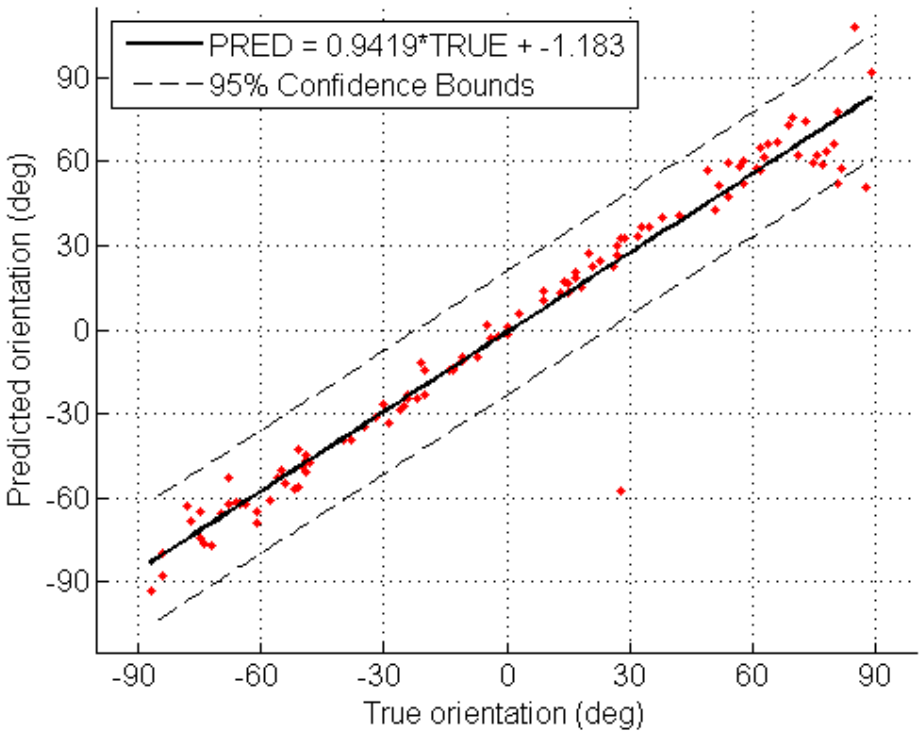

Figure 3.9. Study 2 edge orientation predictions from an SVR model using only the 24 inputs from EP #3 for all three materials with varying stiffness. The model performed well on the test data set despite the differences in compliance.

DISCUSSION

Prediction of edge orientation. We used support vector machines due to the desirable qualities that make them some of the most widely used classification algorithms today (Tan et al., 2006). Given the high levels of accuracy of the developed SVR model, we did not attempt any other algorithms. Nonetheless, other popular supervised learning techniques such as random forests, AdaBoost, and artificial neural networks could be implemented to directly compare trade-offs between different types of models.

In Study 1, we trained a support vector regression model with data from thousands of interactions with edge stimuli having three different surface widths, at two different contact angles, at two different nominal contact forces, and with two different stroke speeds. Accurate predictions of edge orientation were possible even without providing the SVR model with information on stimulus width, fingertip displacement in the z-direction, or contact angle (Table 3.1, Table 3.2). In practice, the only movement-related information one to provide the SVR model is the known stroke speed of the artificial fingertip.

As shown in Table 3.2, when comparing SVR models based on different exploratory procedures, most models having R^2 values greater than approximately 0.8 yielded mean absolute and RMS errors that fell within the [2.5°, 25°] range of human perception thresholds for tactile perception of edge and bar orientation (S. J. Bensmaia et al., 2008). This suggests that the accuracy of the SVR model for perception of edge orientation in a plane is comparable to that of humans, so long as appropriate inputs are provided to the regression model.

Model performance was worst when predicting larger magnitude angles (namely, above 55°) regardless of their sense (+ or -) (*Figure 3.8*). One possibility is that there was increased variability in the stroking motions for larger magnitude angles, which would lead to variability in the training data and inaccuracy in model predictions for large angles. For instance, when steep angles were encountered in which the edge was nearly aligned with the long axis of the finger, the BioTac would sometimes move alongside the edge during EP #3 before stroking the top surface of the stimulus.

Interestingly, our edge orientation predictions also featured a tactile spatial anisotropy similar to that observed in human subjects (described in Chapter 1). Our results, being the least accurate for edge orientations of higher magnitude (above +55° and below -55°), are consistent with the notion that prediction accuracy is better for horizontal orientations along the short axis of the fingertip (S. J. Bensmaia et al., 2008; Lechelt, 1988).

In Study 2, we investigated SVR model performance for stimuli with various levels of compliance (sponge, foam, and rigid ABS plastic). Similar to Study 1, model accuracy was lower for larger magnitude, steeper angles. One outlier degraded overall model performance (*Figure 3.9*). Nevertheless, prediction accuracy (R^2 of 0.95 and RMS error of 11.3°) was still comparable to that of humans (S. J. Bensmaia et al., 2008), even though only input parameters from EP #3 were provided during training of the model.

Effects of contact angle (Study 1). The primary effect of reducing the contact angle from 30° to 20° was that the normal contact force dropped dramatically, resulting in smaller overall fluid pressure and electrode impedance values. For a commanded height of z = -4 mm, the normal contact forces (mean ± standard dev.) during the middle 30% of EP #1 (W1) dropped from 2.72 ± 0.58 N to 1.30 ± 0.46 N. For a commanded height of z = -6 mm (only for the 30° contact angle case), the normal contact forces were 3.48 ± 0.70 N.

Our original hypothesis was that a shallower contact angle of 20° might stimulate a wider range of electrodes. However, all else being equal, the 30° contact angle produced larger skin deformations and, thus, larger changes in

electrode impedance values. Despite the drop in magnitudes across the different tactile data modes for the 20° contact angle case, information about edge orientation remained encoded in the tactile data, especially the electrode impedance time histories (*Figure 3.10*).

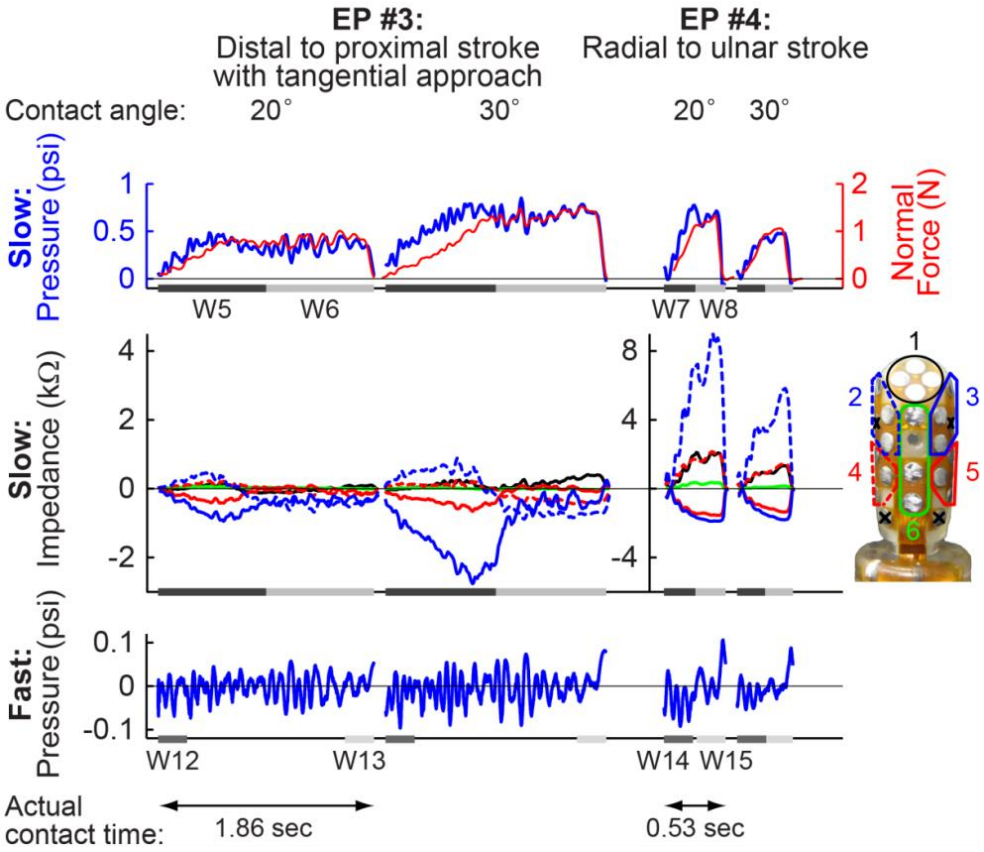

Figure 3.10. Representative multimodal tactile data for the 20° and 30° contact angles during EP #3 and #4 for a thick bar oriented at +75°, commanded displacement of z = -4 mm, and scanning speed of 4 cm/s. Although the 20° contact angle resulted in lower normal contact forces than the 30° contact angle, the electrode impedance values still captured useful spatiotemporal information related to edge orientation.

Effects of the exploratory procedure (Study 1). *Figure 3.5* illustrates how the choice of exploratory procedure can affect qualitatively the multimodal tactile data. EP #1 (static contact) provides a sustained period of overall fluid pressure and electrode impedance data. A comparison of EP #2 and EP #3 quickly reveals how even a subtle difference in approach direction (normal or tangential, respectively) between the two otherwise identical stroking motions can affect the tactile data. For example, there are stark differences in electrode impedance trends for lateral clusters 2-5 between EP #2 (*Figure 3.5*, row 2, W2-W4) and EP #3 (*Figure 3.5*, row 2, W5 and W6). It is hypothesized that the initial contact of the BioTac skin against the stimulus determines how the skin will deform for the remainder of the stroking motion. When the approach to the surface is along the normal direction as with EP #2, the fingertip makes static contact first, which compresses electrode cluster 1 and constrains radial-ulnar pairs of clusters (2-3 and 4-5) to change in concert during initial contact. When the approach is tangential to the surface as with EP #3, the skin is free to deform according to the orientation of the leading edge of the stimulus. As a result, the radial-ulnar pairs of clusters reflect opposite trends in electrode impedance upon contact. Skin deformation during initial contact seems to play a predominant role on the trends of the sensor signals.

In addition, EP #2 results in an overall fluid pressure that begins relatively high and then drops when fingertip motion is initiated. EP #3, in contrast, results in a gradual increase in overall fluid pressure as the fingertip is moved along its stroke trajectory and has completely traversed the edge.

When building a model using EP #1 (static contact) only, the R^2 value was 0.441 and mean absolute and RMS errors were 30.72° and 39.69°, respectively (Table 3.2). When a stroking motion was used, model performance increased substantially (R^2 of 0.712, 0.960, and 0.725 for EP #2, #3, and #4, respectively). For the edge orientation task and SVR model input parameters considered in this work, EP #3 (distal to proximal stroke with a tangential approach) led to the most accurate model with an R^2 value of 0.96 and mean absolute and RMS errors of 5.18° and 10.67°, respectively (Table 3.2).

For EP #3, the fingertip tangentially approached all stimuli, but this was not the case for EP #4. When exploring a broad surface at a negative edge orientation using EP #4, the physical interaction with the edge occurred during loss of contact as opposed to during initial contact. Thus, EP #4 was sometimes similar to EP #2 (normal approach) and sometimes similar to EP #3 (tangential approach) depending on the surface width and edge orientation. Exploration of an edge during initial contact produced more useful tactile data than exploration during loss of contact. During initial contact, the trends in skin deformation were more gradual and present for a longer percentage of the contact period (*Figure 3.5*, row 2, EP #3, W5) than for the abrupt transition at loss of contact (*Figure 3.5*, row 2, EP #4, end of W8).

It was also observed that electrode impedance values were much larger for EP #4 than for EP #3 (rows 2 of *Figure 3.5* and *Figure 3.10*). This may be due to an increase in skin contact area for the radial to ulnar stroke of EP #4 as compared to the distal to proximal stroke of EP #3. Another possibility is that the robot

testbed, specifically the basal joint of the fixed middle BarrettHand finger, was less compliant during collisions with edges when the fingertip moved along the x-axis.

When the two motions with tangential approaches are combined (distal to proximal EP #3 and radial to ulnar EP #4), the predictive power of the SVR model improves to an R^2 value of 0.98 and mean absolute and RMS errors of 3.46° and 7.51°, respectively. If one chooses to use all four exploratory procedures in practice, the R^2 value can be as high as 0.99 and the mean absolute and RMS errors can be as low as 2.89° and 5.08°, respectively. However, the trade-off for such an accurate model is the need to collect tactile data for all exploratory procedures for each trial and the increased complexity of the SVR model (85 inputs). The system designer must assess whether the slight increase in predictive power is worth the additional exploratory procedures, computational expense of tactile data post-processing, and model complexity (beyond the 24 inputs for EP #3 only).

Efficient sets of model input parameters (Study 1). We built multiple SVR models with different input parameters in order to gauge the importance of different inputs and find efficient sets of inputs. As stated previously, EP #3 was found to be the most useful single exploratory procedure (R^2 value of 0.96 and RMS error of 10.67°). Interestingly, a model that used both EP #3 and EP #4 outperformed models based on any single EP (R^2 value of 0.98 and RMS error of 7.51°).

After removing stroke speed, overall fluid pressure, and vibration input parameters, the R^2 value only dropped from 0.991 to 0.987 when all four EPs were considered (removal of 19 input parameters) and from 0.960 to 0.931 when only EP #3 was considered (removal of 6 input parameters). This suggests that the electrode impedance data provide the most useful information for predicting edge orientation. Stroke speed does not seem to be critical since we have already normalized contact time to a percentage during post-processing. Although useful in detecting contact and delineating windows of time, overall fluid pressure does not seem to provide information that is not already included in the impedance signals. As in a preliminary study, the fluid vibration data provided some information about edge orientation magnitude, but not much about direction. Since they were not localized to any specific part of the fingertip, the vibration data were not critical to the prediction of both edge orientation magnitude and direction.

The initial rates of change of the electrode impedance signals were found to be useful. When reducing the model inputs further, the R^2 value dropped from 0.987 to 0.858 when all four EPs were considered (removal of 18 more inputs) and from 0.931 to 0.795 when only EP #3 was considered (removal of 6 more inputs). In a preliminary study, we investigated the usefulness of initial rates of change of the electrode impedance signals for a contact angle of 30° only and concluded that these data only slightly improved model performance. The present study suggests that predicting edge orientation with the fingertip at two different

contact angles is more challenging and that initial rates of change of electrode impedance can be useful.

We also investigated the relative importance of spatial location of electrode impedance data. First, distal-proximal clusters of electrodes were considered (*Figure 3.4*a). Focusing on EP #3, the R^2 value for a model without stroke speed, overall fluid pressure, or vibration data dropped from 0.93 to 0.78, 0.79, and 0.78 after removing electrode impedance data from clusters along the centerline (clusters 1 and 6), ulnar aspects (clusters 2 and 4), and radial aspects (clusters 3 and 5), respectively (Table 3.2). Thus, spatial asymmetry in the tactile data appears to be especially important for this task of predicting edge orientation.

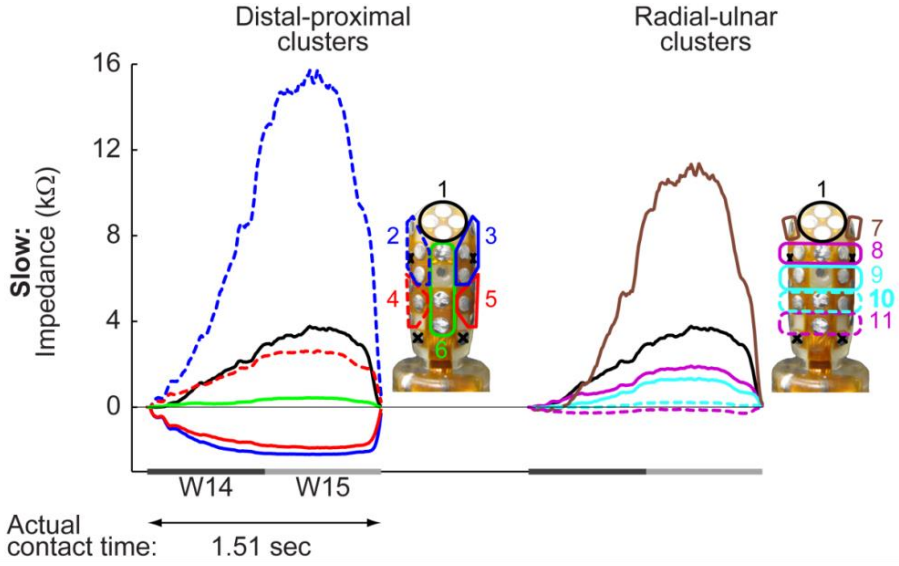

Figure 3.11. Representative electrode impedance data for distal-proximal clusters and radial-ulnar clusters. Data are shown for EP #4, a broad surface oriented at +35°, a 30° contact angle, a commanded displacement of z = -4mm, and scanning speed of 4 cm/s. Distal-proximal clusters appear to better capture skin deformation towards and away from the rigid core.

Notable trends in the tactile data

Usefulness of spatial asymmetry in the tactile sensor signals. For the edge orientation task of this work, it appears that the predictive power of the SVR model is owed primarily to the asymmetry of the slow tactile data (electrode impedance values) with respect to the long axis of the finger. Through both normal and shear forces, electrode impedance increased when the elastomeric skin was compressed against the rigid core of the sensor. Simultaneously, another part of the skin would bulge away from the core. The distal to proximal motion of EP #3 resulted in opposite trends in electrode impedance for clusters on the radial and ulnar aspects of the fingertip (*Figure 3.4*a; solid vs. dashed lines in *Figure 3.5* and *Figure 3.10*).

Considering that the radial to ulnar motion of EP #4 might be better represented by clusters specific to the distal and proximal aspects of the fingertip (*Figure 3.4*), a direct comparison was made between the two different cluster scenarios (*Figure 3.11*). Distal-proximal clusters appear to better capture bulging of the skin away from the sensor core, as evidenced by relatively large negative electrode impedance values. Radial-ulnar clusters typically yield primarily positive impedance values (*Figure 3.11*). It appears as if the skin compression and bulging effects on the radial and ulnar aspects of the fingertip get nullified mathematically when radial-ulnar clusters are used. Without stroke speed, overall fluid pressure, and vibration input parameters, models with radial-ulnar clusters had an R^2 value of 0.50 and RMS error of 37.4° for EP #4 as compared to models with distal-proximal clusters which had an R^2 value of 0.69 and RMS error of

29.8° (Table 3.2). These results suggest that clusters that effectively capture skin deformation can be selected independently of the fingertip velocity vector.

Effects of object compliance (Study 2). Stark differences in the BioTac signals when exploring objects of different stiffnesses are evident when comparing *Figure 3.5* (rigid broad surface) and *Figure 3.7* (compliant broad surfaces). Even with a greater commanded displacement height for the compliant stimuli (z = -6 mm for compliant stimuli, z = -4 mm for rigid stimulus), the electrode impedance values were approximately an order of magnitude less for the compliant stimuli. Furthermore, the skin deformation trends were quite different. The prominent opposing electrode impedance trends for the ulnar and radial clusters observed during haptic exploration of rigid stimuli with EP #3 were no longer evident during haptic exploration of the compliant stimuli.

Table 3.3 indicates that EP #1 was more useful for compliant stimuli than for rigid stimuli. In Study 1, the SVR model trained with EP #1 inputs predicted edge orientation on rigid stimuli having different widths with an R^2 of 0.44 and RMS error of 40°. In Study 2, an SVR model similarly trained with EP #1 inputs performed with an R^2 of 0.89 and RMS error of 18°. The improved performance of EP #1 in Study 2 could be due to the compliant stimuli conforming more to the BioTac, thereby producing more informative, albeit smaller magnitude, patterns of tactile signals. For both compliant stimuli, performance was similar for EP #1 (R^2 values of 0.98 each for the sponge and foam block) and EP #3 (R^2 values of 0.98 and 0.99 for the sponge and foam, respectively). For the ABS plastic, performance with EP #3 inputs (R^2 of 0.99, RMSE of 4.0°) was better than with

EP #1 inputs (R^2 of 0.89, RMSE of 18°). Our results suggest that edge orientation predictions are more sensitive to exploratory procedure for rigid stimuli than compliant stimuli.

A single SVR model created using tactile data from materials with different stiffnesses (sponge, foam, and ABS plastic) performed well (R^2 of 0.95 and RMS error of 11.3° when providing EP #3 inputs) even though trends in the tactile signals were different for compliant and rigid stimuli (*Figure 3.5* and *Figure 3.7*). Independent SVR models created for a single sample (sponge, foam, or ABS plastic) performed even better (Table 3.3). If such levels of accuracy are desired, it would be straightforward to first implement an EP to estimate stiffness (e.g., static contact EP #1 or the method presented in (Su et al., 2012)), which could then be used to select a stiffness-specific SVR model.

Models with linear kernels performed much better for the sponge and foam stimuli than for the ABS plastic (Table 3.3). Conformation of the compliant stimuli around the BioTac sensor likely increased contact area and may have resulted in richer skin deformation information (R. L. Klatzky & Lederman, 1999; Su et al., 2012) . Interestingly, the BioTac sensor was capable of estimating edge orientation for stimuli that were more stiff as well as less stiff than itself. The deformable skin and bladder-type design of the BioTac likely contributed to this capability.

Effects of a bladder-type tactile sensor construction. The richness of the tactile data generated from EP #3 alone highlights the usefulness of simple finger-object interactions and how tactile sensors that make use of deformable skins as

part of the mechanotransduction process (e.g., (De Maria, Natale, & Pirozzi, 2012; Hristu, Ferrier, & Brockett, 2000; Ponce Wong, Posner, & Santos, 2012; Nicholas Wettels et al., 2008)) may yield advantages beyond shock absorption, increased contact area, and tackiness of the grip. A typical robotics approach of mounting rigid, 6 DOF force transducers on artificial fingertips might be straightforward from a traditional modeling and grasp planning perspective (Prattichizzo & Trinkle, 2008), but such an approach may be inappropriate for obtaining insight into human finger-object interactions with deformable skin and multimodal tactile sensing capabilities.

An interesting finding is that the tactile data that enabled accurate prediction of edge orientation were generated by regions of the tactile sensor that were not in direct contact with the stimulus. For the fingertip orientation used in the experiments, electrode clusters 2-5 (*Figure 3.4*) were not always compressed by the finger-object interaction. Rather it was the free surface of the skin that was able to bulge away from the rigid core of the sensor.

This finding has interesting consequences for the development of tactile sensing systems for artificial hands. Traditionally, for reasons of cost and simplicity, a designer might place tactile sensor arrays only on those surfaces of the artificial hand that might contact an object during grasp such as the palmar aspects of the digits and palm. However, if a bladder-like sensor system (e.g., (Hristu et al., 2000; Nicholas Wettels et al., 2008)) is implemented such that skin deformation at finger-object contacts can affect skin deformation at non-contact regions (radial or ulnar regions in this work), the non-contact regions can provide

a surprising wealth of information about finger-object contacts. While we and others have previously related electrode impedance data to contact forces (J. A. Fishel & Loeb, 2012; Lin et al., 2009; Nicholas Wettels et al., 2008), this work suggests that it may be useful to relate electrode impedance to skin deformation. For instance, compression of skin against the rigid core can occur even when a compressive force is not applied directly to that region of the skin because shear forces elsewhere can deform the continuous skin.

Moving beyond tactile images generated by static contact with objects. The standard robotics approach to tactile sensing of shapes and edges is to create a "tactile image" (e.g., (Berger & Khosla, 1991; H.-K. Lee et al., 2006; Mei et al., 2000; Petriu et al., 1992)) from a series of static contacts with an object. As such, tactile sensor designs have often focused on achieving fine spatial resolution so that accurate reconstructions of images can be built through static contacts alone (Dahiya et al., 2010). Despite the fact that biological fingertips have fine spatial resolution capabilities (Johansson & Flanagan, 2009), humans elect to use dynamic fingertip motions when identifying local features such as edges (Huynh et al., 2010; Lederman & Klatzky, 1987). Consider an example such as identifying the edge of your cellphone in your pocket. It is nearly impossible to force oneself to perform this task using a series of static contacts alone. While the completion of the task may be successful with static contacts, confirmation of edge orientation via contour-following is somehow more satisfying.

By including different windows of contact phases in our regression model, both spatial and temporal changes in tactile signals were taken into account as

opposed to a single static "snapshot" of finger-object contact. Emphasis was placed on efficient use of tactile data from different windows of time as a function of exploratory procedure.

While the results presented here are specific to the data provided by the BioTac sensor, the general approach to artificial perception is applicable to any robotic or prosthetic system that is designed to measure both slow and fast types of tactile data and to interact dynamically with the physical world. Interestingly, we purposely degraded the spatial resolution of the tactile data by taking means of electrode impedance values. Furthermore, for simplicity and proof-of-concept, we restricted exploratory motions to linear strokes with constant speeds, as opposed to raster-like, scanning procedures employed by some blindfolded human subjects when locating features on novel objects (Huynh et al., 2010). Despite these self-imposed limitations, the SVR model performed well (Table 3.2).

Limitations. Prior to data collection, automated tendon re-tensioning and recalibration of the WAM was conducted. Nonetheless, due to its cable driven nature and lack of absolute position encoders at each joint, position and orientation control with the Barrett WAM can be imperfect, resulting in variability in the execution of the exploratory procedures. Variability in the training data may be slightly advantageous in that artificial systems will always have variability in practice, models trained on distributions of data will be robust to some small but nonzero variability, and Bayesian approaches to learning can use these distributions of sensory responses as prior distributions. Variability in motor actions (and subsequent variability in sensory feedback) may help to

facilitate motor learning, as it appears to do so in humans (Riley & Turvey, 2002; Sternad & Abe, 2010). Variability in sensory feedback could also be used to reweight the reliability of different tactile datastreams or affect subsequent motor actions during active sensing (Stamper, Roth, Cowan, & Fortune, 2012).

FUTURE WORK

If one desired to establish edge orientation of rigid stimuli more efficiently, it may be possible to modify the post-processing protocol for the static contact exploratory procedure (EP #1). In a preliminary study performed without the benefit of a robot testbed, we manually performed the static contact procedure on thin blades having different orientations with respect to the fingertip. Even when using all 19 electrode impedance signals separately, the sensor was unable to accurately predict edge orientation. However, our manual setup lacked precision and repeatability. It is possible that better model performance could be achieved with EP #1 if we used a robot testbed and did not reduce the spatial resolution of the sensor by creating clusters of electrodes during signal post-processing. In the presented work, we voluntarily decreased our spatial resolution to reduce computation time. If we released this artificial constraint on spatial resolution, we may find that some electrodes could provide more useful information than others or that individual electrodes encode more useful information for predicting edge orientation than clusters of electrodes. Finally, additional exploratory procedures such as “finger roll” (which will be introduced

in the Methods section of Chapter 4) could be attempted for predicting edge orientation.

If additional model accuracy or alternate input parameters are desired, modifications to the SVR models can be considered. For instance, one could decompose tactile signals into smaller windows of time or consider differences in impedance across pairs of electrodes (Su et al., 2012). The delays imposed by tactile data post-processing, analysis of fast tactile signals via HHT, and extraction of SVR input parameters on online estimation of edge orientation and, eventually, contour-following require further investigation.

For the purposes of establishing the orientation of a feature such as an edge with respect to a body-fixed reference frame, the models described in this work may suffice. Establishing a model of object orientation within the hand would be useful for designing artificial reflexes for the prevention of slip or planning the manipulation of the grasped object within one's own hand, with the environment, or with another hand (bimanual manipulation or physical interaction through the object with another agent).

For the purposes of a more advanced behavior such as contour-following, it may be necessary to develop models in which the fingertip trajectory length is shorter. This might better reflect a contour-following strategy in which the finger is never (or infrequently) lifted from the surface of the 3D object. In this case, the previous incremental movement of the fingertip and the estimated model of the object shape up to that timepoint would be used to inform the next incremental movement of the fingertip. It may be that an exploratory procedure that begins

with a static contact, such as EP #2, turns out to be particularly useful for contour-following.

Next steps include the use of an edge orientation model to inform a decision-making process for autonomous contour-following algorithms for 2D shapes, initially. It may be useful to build multiple SVR models and to invoke a specific one depending upon the exploratory procedure that was implemented. Further, it may be necessary to build a library of haptic experiences with vertices for contour-following of shapes with corners (J. Baeten & De Schutter, 2002).

CHAPTER 4

HAPTIC EXPLORATION OF FINGERTIP-SIZED GEOMETRIC FEATURES USING A MULTIMODAL TACTILE SENSOR

INTRODUCTION

Tactile sensing is especially useful in scenarios where vision is inadequate such as in low lighting or when line of sight is obstructed. For instance, reaching into backpacks or pockets typically involves exploring an unstructured environment with our hands until we identify, grasp, and manipulate the object of interest. Objects typically have distinguishing geometric features that can be used to identify objects or their orientation with respect to the hand. One everyday example is the use of a TV remote without vision. After becoming familiar with the remote, one knows how to haptically identify the different buttons by recognizing their planar shape and location.

A seminal psychophysics study identified haptic exploratory procedures that humans use when extracting object properties through touch (Lederman & Klatzky, 1987). Whole-hand enclosure of the object and single-digit contour-following along the object's surface can be used to estimate global and local geometric properties, respectively. These actions combined with thousands of specialized mechanoreceptors (Johansson & Vallbo, 1983) give the human hand haptic perception capabilities that remain the gold standard to this day. It remains a grand challenge for roboticists to develop artificial hands with similar levels of haptic intelligence.

Human Discrimination of Curvature. Although the most salient geometric properties of a 3D object have been found to be edges and vertices (Plaisier et al., 2009), curvature plays an important role when exploring objects through contour-following. Multiple human studies have focused on curvature discrimination of objects that span the length of the finger. One study showed that regardless of whether a static or dynamic approach to estimate curvature was employed, haptic curvature discrimination was based on differences in attitude (or slope) (Pont, Kappers, & Koenderink, 1999). The static condition tested various scenarios in which only the fingerpad of one to three fingers were placed on at specific locations on geometrically different stimuli. In order to study how differences in curvature are perceived, stimuli were designed to be 0^{th} order, 1^{st} order, and 2^{nd} order with corresponding changes in height, slope, and curvature, respectively. For the dynamic condition, the index finger stroked along 2^{nd} order stimuli (moving along the short axis of the finger). The subject had to report which of a presented pair was more convex.

Another study investigated the discrimination of curvature of objects with Gaussian protrusions varying in height and width (Louw, Kappers, & Koenderink, 2002). Subjects had to determine which of a presented pair of stimuli was more like a reference stimulus. Subject were allowed to scan stimuli by moving their fingers from one end to the other. In general, subjects were better at discriminating sharp Gaussian surfaces (large height, small width) from smooth ones (small height, large width). Worse performance resulted when discriminating small surfaces (small height and width) from large surfaces (large

height and width). In other words, if the proportion of both variables of the Gaussian profile are similar, human discrimination of geometrical features is poor.

One study investigated differences in human perception of curvature when tactile and visual means were used (Ittyerah & Marks, 2008). Two concave objects were presented simultaneously, and subjects were asked to identify the objects as being the same or different. During the haptic condition, subjects were instructed to move two fingers across the objects simultaneously. The modalities had the following ranking of from highest to lowest accuracy: vision only, paired vision and touch, and touch alone. At such large object dimensions relative to the human fingertip, the large overall size of the objects (radii of curvature ranging from 13.2 to 34.1 cm and from 3.81 and 10.16 mm) might have been better suited for vision than touch. For accurate curvature perception, memory at the start and end locations of the linear movement is needed (Millar, 1994). Thus, for large surfaces, vision has the advantage of having a global representation and touch has the disadvantage of need memory retention throughout the scanning motion.

Another human study investigated the information necessary to identify a target object in a grid of cubes (Overvliet, Smeets, & Brenner, 2008). Blindfolded, subjects could accurately find a cylinder within the grid of cubes using a single digit due to curvature discriminability. However, detecting a rotated cube or a rectangular bar (same as the cube but with one larger dimension) was more challenging as it required the use of proprioception. In the case of the rotated cube, proprioceptive information such as hand and finger orientations

would be needed. For the bar, the proprioceptive information of the distance traveled during dynamic touch or that of multiple fingers would be needed.

Artificial Haptic Perception of Object Shape. Previously, artificial tactile sensors with high spatial resolution have been used to track edges (Berger & Khosla, 1991) and estimate the shapes of alphabet characters inscribed in rubber stamps (H.-K. Lee et al., 2006), planar polyhedron faces (Petriu et al., 1992) and keys (Mei et al., 2000) by creating static tactile images. However, the objects typically explored were large relative to the tactile sensor and flat.

Numerous works have sought to incorporate human haptic exploration strategies and capabilities into the robotics domain. An active touch sensing framework involved a hierarchical approach in which coarse properties, such as overall dimension with respect to a robotic hand, were first determined via whole-hand enclosure (Allen & Michelman, 1990). This was followed by procedures referred to as "planar surface explorer" and surface contour following. Artificial proprioceptive feedback (joint angles, tendon forces) and tactile feedback were used to model 3D object shape.

A comprehensive study was done on the detection and characterization of curvature features from a robotic perspective (Okamura & Cutkosky, 2001). Geometric features were defined based on the two principal curvatures in their contour and were assumed to have dimensions comparable to that of the artificial fingertip. Two algorithms for feature detection involving tactile feedback and two without tactile feedback were described. An experiment was performed in which a rigid spherical fingertip moved over 0.5-1.5 mm diameter wires (representing

bumps). The study showed that the algorithms incorporating tactile sensing performed worse than those who did not. Poorer performance was attributed to the more noisy measurements of points of contact of the tactile sensor compared to the proprioceptive fingertip position. Nevertheless, the authors recognized that the way their robotic system detected features most accurately was not similar to the way humans perform such tasks with their superior biological tactile sensors. The spherical, non-deformable nature of the robot fingertip likely limited the ability of the tactile sensor to provide rich information on curvature. Simultaneously, the rigidity of the fingertip may have contributed to reliable proprioceptive feedback since the robot testbed could be viewed as having digitizer-like functionality.

Haptic Perception of Finger-sized Geometric Features. Literature on haptic exploration of small, finger-sized geometric features is scarce. The multimodal BioTac sensor has been used to estimate radius of curvature of finger-sized spherical features via machine learning techniques (N. Wettels & Loeb, 2011) and mathematical models (Su, Li, & Loeb, 2011). However, only four discrete classes were used by the machine learning techniques.

When vision and proprioception are inadequate for characterizing finger-sized geometric features, tactile sensing becomes especially useful, especially with the small dimensions of the feature preclude the use of multiple digits to extract information such as order of curvature. The objective of this work was to explore geometric features whose dimensions are on the same scale as the human fingertip in order to extract important properties such as type (bump, pit), order of

curvature (planar, conical, spherical), and overall width. Different bio-inspired exploratory procedures were investigated in order to determine their efficiency and accuracy for extracting geometric properties. The ability to determine local shape information with a single fingertip could be used to provide haptic feedback to a robot operator, a sense of touch to an amputee, or tactile feedback for semi-autonomous grasp and manipulation controllers for teleoperated robots, such as wheelchair-mounted robot arms.

METHODS

Robot Testbed and Tactile Stimuli. The robot testbed is the same one used in the edge orientation study (Chapter 3): a BioTac sensor was attached to the BarrettHand and WAM robotic system (*Figure 4.1*). As before, while the BioTac's overall fluid pressure signal and 19 impedance signals were sampled at 100 Hz, the vibration signal was sampled at 2200 Hz. Since we are primarily interested in mechanical stimuli for this study, the temperature measurements were not considered in the data analysis. For greater detail, please refer to the Methods section in Chapter 3.

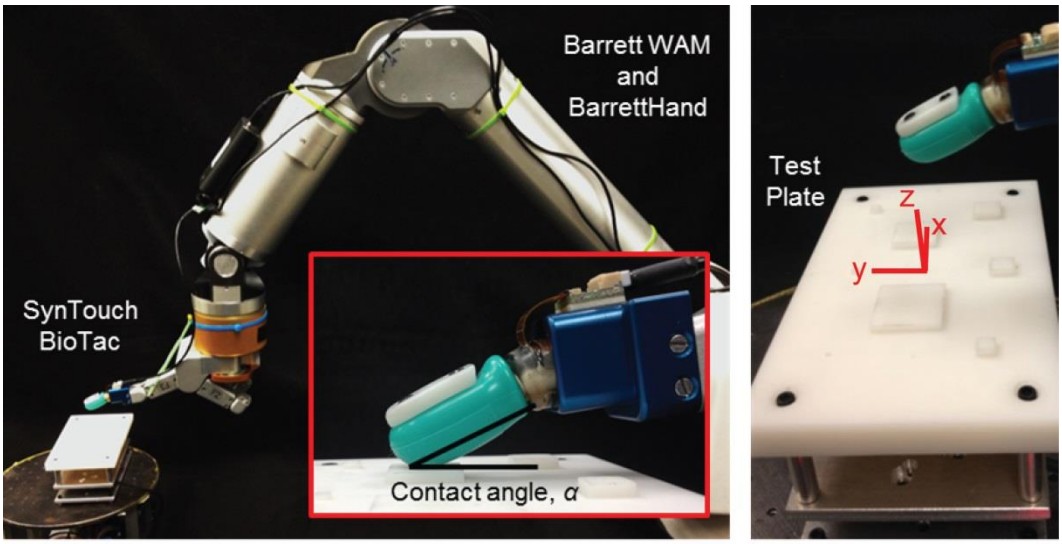

Figure 4.1. The experimental setup in which the Barrett WAM, BarrettHand, and BioTac were used to explore fingertip-sized geometric features. a) The BioTac was held at either a contact angle α of 25° or 30°. b) The test plate with tactile stimuli maintained a constant orientation with respect to the fingertip reference frame. The largest feature has 'footprint' dimensions less than twice the width of the BioTac. The global reference frame is shown in red.

We hypothesized that properties of small geometric features, including order of curvature and footprint overall dimension, could be extracted from the tactile signals alone. Three different 3D printed test objects, each of which had a face with bumps (protrusion in the (+) z-direction) and an opposing face with pits (depression in the (–) z-direction), were used (*Figure 4.2*). The face of each test object contained eight distinct features with a specific degree of curvature: 0^{th} order or planar features, 1^{st} order or conical features, and 2^{nd} order or spherical features. Length for planar features and diameter for conical and spherical

features were 1.25, 2.5, 3.75, 5, 7.5, 10, 15, and 20 mm (see *Figure B.1*). The five largest features had a constant height or depth of 2.5 mm. The three smallest features had heights or depths equal to half their footprint dimension. Note that in order to maintain consistent heights across features having different orders of curvature, the equators of the spherical features where not at z = 0, the datum of the test plate (*Figure 4.2*). The tactile stimulus was rigidly attached on top of a 6 DOF load cell (ATI Industrial Automation, Nano-17, *Figure 4.1*). The plate was designed such that x- and y-axis spacing between features would allow for haptic exploration of a single feature with one haptic exploratory movement (*Figure 4.2*).

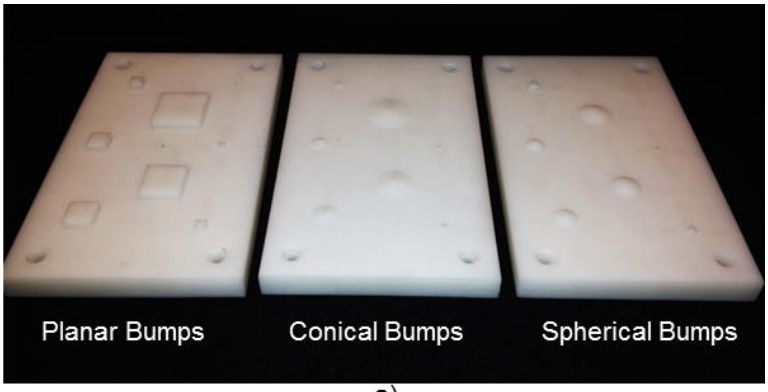

a)

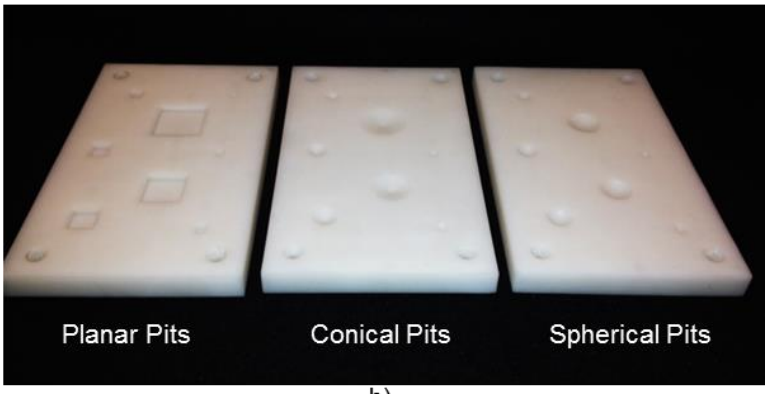

b)

Figure 4.2.Test plates containing small geometric features with varying orders of curvature and size. A total of three plates were used, each of which contains a)

bumps on one face and b) pits on the opposing face. Each plate had features with eight different footprint dimensions: 1.25, 2.5, 3.75, 5, 7.5, 10, 15, and 20 mm.

Haptic Exploratory Procedures. The WAM trajectories were commanded by prescribing joint angles through the internal "libbarrett" library. Similar exploratory procedures (EPs) to those introduced in Chapter 3 (*Figure 3.3*) were implemented. Namely, static contact (EP #1), distal-proximal stroke along the y-axis (EP #3), and radial-ulnar stroke along the x-axis (EP #4) were used. An additional bio-inspired exploratory procedure was implemented in which the finger was rotated about its longitudinal axis in order to roll back and forth over the geometric feature (EP #5). EP #5 was designed to approximate wrist supination and pronation, although actual implementation of the motion was more complex because the longitudinal axis of the BioTac sensor was not aligned with the wrist axis. Snapshots of the different EPs are shown in Fig. 4.3, in which movements are indicated by red arrows. A fixed global reference frame was defined with its origin at the (x, y) center of the plane and z = 0 such that the x-y plane was concident with the flat open area of the plate (*Figure 4.1*b). As with the edge orientation study (Chapter 3), the x-axis was defined as the direction for the radial-ulnar stroke, and the y-axis as the direction for the distal-proximal stroke.

For EP #1, the fingertip approached the feature directly from above along the z-axis, pressed statically against the feature for 1.5 seconds, and moved away along the z-axis to release contact (*Figure 4.3*a). EP #3 consisted of the fingertip being aligned to the center of the feature along the y-axis at a location distal to the

feature (*Figure 4.3*b). The fingertip would approach the test plate until a predefined z-position has been reached, making contact with the plate's surface. The fingertip would then move along the negative y-direction, stroking along the whole length of the feature until it returns back to the plate's bare surface. Similarly, for EP #4 the fingertip was aligned along the x-axis at a location radial to the center of the feature (*Figure 4.3*c). The sensor would first make contact with the plate's surface and then stoke along the positive x-direction until the entire feature has been explored. For EP #5, the fingertip approached the feature directly from above along the z-axis (*Figure 4.3*d). Wrist supination of 45° took place while maintaining the fingertip's x- and y-positions centered on the feature. Wrist pronation pronated in order to return to the fingertip to its original orientation, and the fingertip was moved away along the z-axis to release contact.

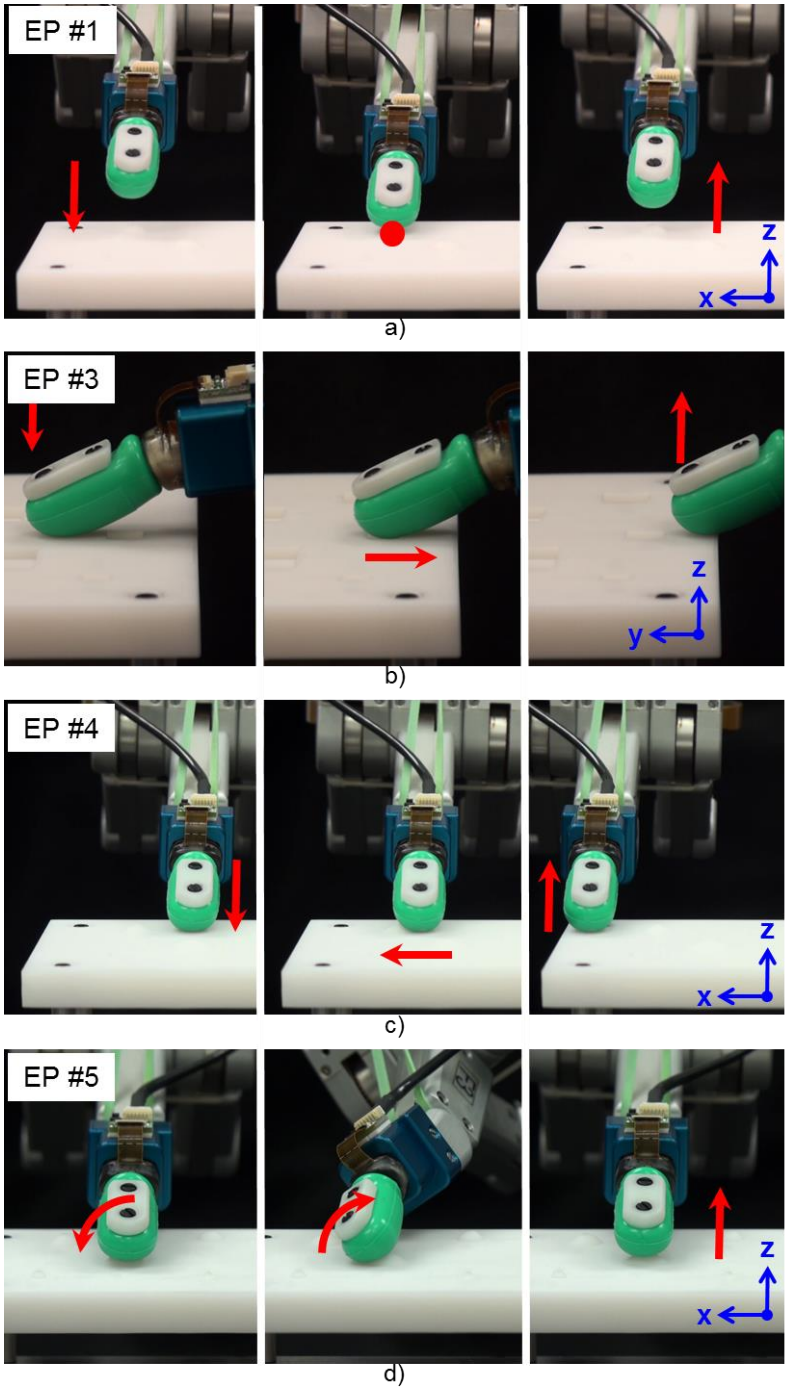

Figure 4.3. Haptic exploratory procedures. a) EP #1: static contact, b) EP #3: distal to proximal linear stroke along the y-axis, c) EP #4: radial to ulnar linear stroke along the x-axis, and d) EP #5: roll of the fingertip about its longitudinal axis. Fingertip movements are indicated by the red arrows. Note that x-, y-, and

z-axis directions are accurately shown, but the origin of the global reference frame has been displaced for visualization purposes.

As before, the contact angle α was defined as the orientation of the BioTac's longitudinal axis with respect to the horizontal x-y plane (*Figure 4.1*a). A contact angle of 25° was chosen in order to maximize the contact area between the BioTac's deformable skin and the tactile stimulus while simultaneously avoiding undesirable contact of the BarrettHand with the test plate for EP #1, EP #3, and EP #4. A contact angle of 30° was used for EP #5. Inspired by previous human studies (S. J. Bensmaia et al., 2008) and given the small dimensions of the geometric features, scanning speed was 1 cm/s for linear stroking motions. Thus, the fingertip trajectory velocity for EP #3 was v_y = -1 cm/s while that for EP #4 was v_x = +1 cm/s.

For all four exploratory procedures, the commanded height for the fingertip was z = -5.5 mm such that contact was consistently made with the bottoms of large pits but did not get stuck on large bumps. Given the low precision and large variability of the robot testbed at millimeter scales, the command height value was determined by trial and error prior to data collection.

Features within each plate face were explored in a random order to minimize the introduction of any bias due to systematic variations, such as wear of the tactile sensor skin. The test plates were presented in the following order: planar pits, planar bumps, spherical pits, spherical bumps, conical pits, and conical bumps. A total of 20 replicate trials per feature on each test plate were

collected before changing the plate. The BioTac skin was constantly monitored to ensure that the fingerprints had not worn out. The skin only required replacement once due to noticeable wear of the tactile ridges.

Processing of tactile signals. As with the edge orientation study (Chapter 3), it was hypothesized that various types of signals could provide insights into different properties of the geometric feature being explored. For the edge characterization study, all tactile data between the start and loss of contact were used to extract input parameters for supervised learning models. However, this approach could not be used for this study on geometric features. In particular, linear stroking motions (EP #3 and #4) were such that initial contact and loss of contact with the plate occurred at the flat, open regions in between features of interest. For the purposes of modeling specific geometric features, it was important to extract tactile signals that related directly to the geometric feature (bump or pit) as opposed to just any arbitrary contact with the test plate.

Identifying initial contact and loss of contact with a geometric feature. For each trial, initial contact and loss of contact with the test plate were determined as the time points at which the sensor's overall fluid pressure first exceeded and last fell below a threshold of 0.2% from baseline (non-contact state), respectively. This threshold was smaller than that for the edge orientation study because haptic exploration of pits resulted in much smaller changes in overall fluid pressure.

For EP #3 and #4, in particular, it was necessary to further differentiate tactile data associated with the geometric features from those during arbitrary

contact with the open test plate surface. For EP #3, initial contact with the feature was defined as the time point at which electrode Cluster #1 (the most distal cluster at the fingertip, *Figure 3.4*a) changed after its initial rise and plateau (*Figure 4.6*). The sharp rise in this impedance signal occurred in all trials since the fingertip always contacted the plate's surface first. Once the desired commanded height of the fingertiphad been achieved, the impedance signal remained stable, even as the fingertip was stroked across the open, flat surface of the plate, until initial contact with a geometric feature was made. For EP #4, initial contact with the feature was defined as the time point at which electrode Cluster #2 (the ulnar cluster on the distal aspect of the fingertip, *Figure 3.4*a) exceeded an impedance threshold of 1 kΩ. The rise in this impedance signal occurred in all trials since the fingertip was stroked in a radial to ulnar manner. For both EP #3 and #4, loss of contact with the feature was defined as the time point at which electrode Clusters #1, #2, and #3 (the most distal clusters, *Figure 3.4*a) stabilized for the remainder of each trial. This stabilization of impedance signals signified that the fingertip had completely traversed the geometric feature of interest and was simply stroking along the plate's flat, open surface.

For EP #5, the Barrett WAM proprioception data (joint angles) were used to estimate the angle of roll of the finger about its longitudinal axis. To ensure that only data from the rolling motion were provided to the supervised learning models, a rotation threshold of 10° of supination was used to define the start and end time points of rolling contact with the feature. Brief periods of static contact

with the feature at the start and end of the entire trial were not used, as they were not representative of tactile data generated during roll of the finger.

It should be noted that the Barrett WAM proprioception data for fingertip z-position were not precise enough to establish the presence or properties of the small geometric features. This suggests that tactile sensing is better suited for haptic exploration of small geometric features, especially when the robot testbed features deformable fingertips and a robot arm with gear lash and limited precision at millimeter scales.

Establishing windows of interest within the feature contact period. As in the edge orientation study, the contact period was subdivided into smaller windows of time in order to capture trends in the tactile signals at different stages of each exploratory procedure (*Figure 4.7*, Table 4.1). "Window 1" (W1) was defined as the middle 30% of contact for EP #1. For EP #3 and EP#4, the contact period with the geometric feature was split into two equal windows of time (W2 and W3 for EP #3, W4 and W5 for EP #4). Since EP #5 consisted of a symmetric rotation about the longitudinal axis of the fingertip, the contact period was also split into two equal windows (W6 and W7). For each of these windows W1-W7, mean overall pressure values were used as inputs to the supervised learning models. In addition, mean rates of change in overall pressure for the first 25% of windows W2, W4, and W6 were calculated.

Sensor skin deformation was captured by changes in electrode impedance values. Clusters of electrodes along the BioTac's distal-proximal axis defined in the edge orientation study (*Figure 3.4*) were also used in this study in order to

minimize the number of model input parameters and computational expense. For windows W1-W7, mean electrode impedances for each cluster were provided to the model. Mean rates of change in electrode impedance for each cluster for the first 25% of windows W2, W4, and W6 were calculated.

The contact dynamics at initial contact and loss of contact with the feature was captured by the fluid vibration data. For EP #3, W8 and W9 were defined as the first 250 ms of W2 and final 250 ms of W3. For EP #4, W10 and W11 were defined as the first 250 ms of W4 and final 250 ms of W5. For EP #5, W12 and W13 were defined as the first 250 ms of W6 and final 250 ms of W7. For features that resulted in windows W2-W7 being shorter than 250 ms, the entire window of data was used to extract the model inputs. As in the edge orientation study, the Hilbert-Huang Transform (HHT) was used to determine the mean instantaneous frequency of the first intrinsic mode function for use as model inputs. For more details, please refer to the Methods section of Chapter 3.

Supervised Learning Models. The small geometric features used in this study (*Figure 4.2*) have various properties that could be determined. For instance, each feature could be simply identified as either a bump or a pit. The feature's order of curvature could also be classified into three possibilities (i.e. 0^{th}, 1^{st}, and 2^{nd} order), which differentiates the feature's shape as planar, conical, or spherical. In addition, the "footprint" (or x-y plane) dimension can be estimated. The specific height or depth (z-dimension) of the feature was not estimated in this work, but could be incorporated into future modeling efforts.

Identification of order of curvature and footprint dimensions of the geometric features could be accomplished in a few different ways, including those shown via flow diagrams in *Figure 4.4*. A support vector classifier (SVC) was used to identify one of three discrete classes of order of curvature (0^{th}, 1^{st}, 2^{nd}). A support vector regression (SVR) was used to estimate the footprint of the feature from a continuous number line. Although only eight distinct footprint dimensions were tested due to practical reasons, we believe that regression models can be generalized to other feature dimensions while a classifier model would be limited to only those eight footprint dimensions. We used the sign of the footprint dimension to embed information about whether the feature was a bump or a pit. A positive sign was used to indicate that the feature was a bump, while a negative sign was used to indicate that the feature was a pit.

In flow diagram #1, a 3-class SVC model and an SVR model could be conducted in parallel and independently (*Figure 4.4*a). The SVR model would have been trained on tactile data from all features. In flow diagram #2, an SVC could be used to first identify the order of curvature, which could then be provided as an additional input to an SVR model (*Figure 4.4*b). Again, the SVR model would have been trained on tactile data from all features. In flow diagram #3, an SVC prediction could be used to select an SVR model that was trained on features with specific orders of curvature (*Figure 4.4*c). The serial approach of Fig. 4.4c could also be conducted in parallel if independent computational threads were used. In the presented work, we focused on the parallel configuration of Fig. 4.4a and the series configuration of *Figure 4.4*c.

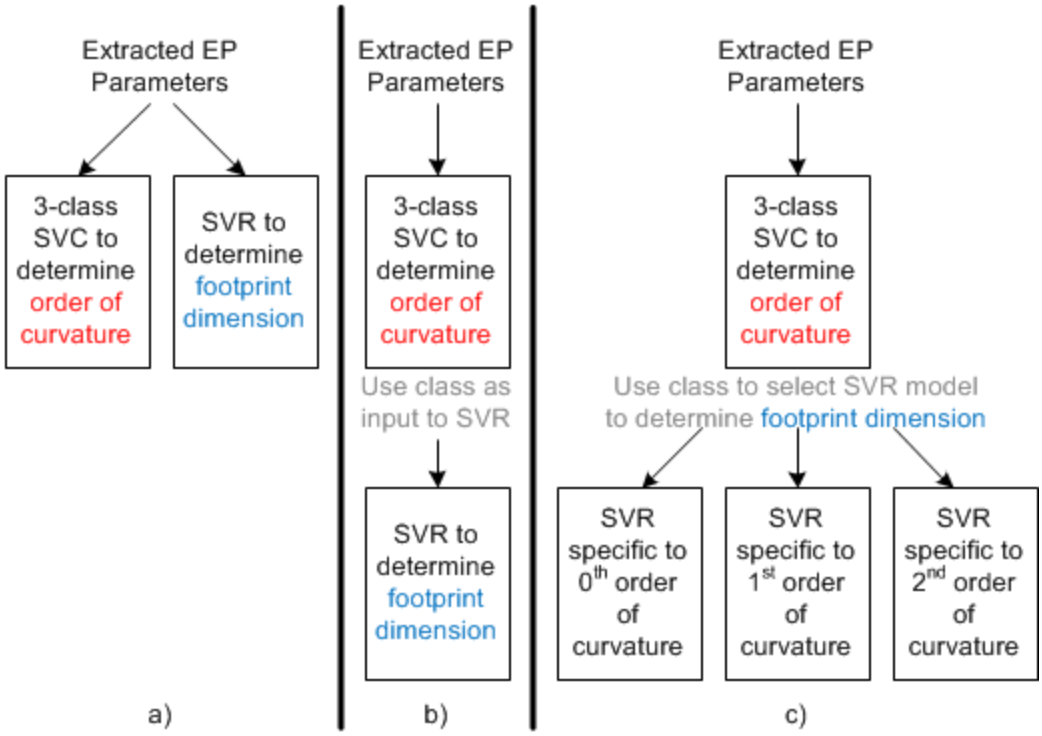

Figure 4.4. Alternative flow diagrams to determine the order of curvature and the feature's footprint dimension. a) Flow diagram #1: a 3-class SVC and an SVR are run in parallel and independently. b) Flow diagram #2: an SVC is followed by an SVR using the classifier prediction as an input. c) Flow diagram #3: an SVC prediction determines which of the SVR models, specific to the order of curvature, to implement in the next step.

When building the models, the complexity term was set to 1 in order to compare results from the two modeling approaches (*Figure 4.4*a, *Figure 4.4*c). Two types of polynomial kernels were used: a linear kernel and a quadratic kernel. The performance of each model was assessed using a novel test data set that was not used during training of the model. WEKA was used to create these models using up to 76 input parameters (Table 4.1). Although WAM

proprioception data were used to determine the initial contact and loss of contact with each feature, no proprioceptive data were provided as model inputs. Furthermore, no information about the exploratory procedure (EP # or fingertip scanning speed) was provided to the models. For the SVC model, the prediction variable was the order of curvature of the feature. For the SVR model, the prediction variable was the footprint dimension of the feature.

In order to minimize time spent on reconfiguring the experimental set-up, trials were blocked by test plate surface. Each of the six test plate surfaces contained one of three orders of curvature (0^{th}, 1^{st}, 2^{nd}) and one of two types of features (bump or pit). We collected 20 trials of tactile data for each of the eight features having different footprint dimensions. For each of the six experimental blocks, the tactile data were randomly split into a training set (90% of total trials, or 144 trials) and into a testing set (10% of total trials, or 16 trials). For the parallel modeling approach of *Figure 4.4*a, the SVC and SVR models were trained with the training data sets and testing data sets from all six block conditions (i.e. 864 trials for training and 96 trials for testing). For the serial modeling approach of *Figure 4.4*c, the SVC was trained as in the parallel modeling approach. However, SVR models specific to the three different orders of curvature were each trained and tested with the appropriate subset of the data (288 training trials, 32 testing trials) since only two block conditions were used for each order of curvature case.

Table 4.1

SVC and SVR Model Input Parameters for Haptic Exploration of Small Geometric Features

Type of info	**Input to SVR model**	**EP #1 (static contact)**	**EP #3 (distal to proximal stroke)**	**EP #4 (radial to ulnar stroke)**	**EP #5 (finger roll)**
Slow tactile signals	Overall fluid pressure	(1) W1	(2) W2, W3	(2) W4, W5	(2) W6, W7
	Initial rates of change of overall fluid pressure	---	(1) W2	(1) W4	(1) W6
	Electrode impedance	(6) W1 for Clusters 1-6	(12) W2, W3 for Clusters 1-6	(12) W4, W5 for Clusters 1-6	(12) W6, W7 for Clusters 1-6
	Initial rates of change of electrode impedance	---	(6) W2 for Clusters 1-6	(6) W4 for Clusters 1-6	(6) W6 for Clusters 1-6
Fast tactile signals	Instant. freq. (of 1st IMF) of vibrations	---	(2) W8, W9	(2) W10, W11	(2) W12, W13

Note. Parenthetical values in red indicate the number of inputs for each type of parameter.

RESULTS

Alignment of the fingertip frame and global reference frame in the test plate. During set-up of the experiment, we found inaccuracies between the commanded and actual 3D Cartesian positions of the fingertip. Given the small dimensions of the features and their fixed locations on the 3D printed test plates, it was important that the fingertip reference frame be aligned with the global

reference frame located on the test plate. Since our proof-of-concept approach relied on centering the fingertip directly above each feature of interest for haptic exploration, an initial calibration was performed. The alignment process used a 3D printed BioTac proxy with a screw attached to its tip (*Figure 4.5*) and a test plate with conical bumps having much larger dimensions for calibration purposes (compare the plate in *Figure 4.5* with that in *Figure 4.2*). A heat shrink tubing was used to wrap the tip of the screw in order to avoid damage to the test plate.

The aim of the calibration process was to determine a homogeneous transformation matrix to relate the robot's command reference frame to the global reference frame fixed to the test plate such that a commanded movement along the robot's y-axis would align with the test plate y-axis, for example. The homogeneous transformation provided a rotation matrix and translation vector to relate the two reference frames. The Cartesian positions of the peaks of the conical bumps were known from their SolidWorks drawings. By trial and error, the commanded robot positions necessary to touch the tip of the screw to each peak (green dots in *Figure 4.5*) were recorded. Both datasets of Cartesian points were then provided to an algorithm that finds the optimal homogeneous transformation from the dataset's centroid (Besl & McKay, 1992). The proxy was later replaced with a real BioTac for data collection, and the translation vector to the fingertip was adjusted accordingly. The resulting transformation resulted in commanded WAM trajectories that accurately explored the geometric features with the BioTac using the EPs previously described.

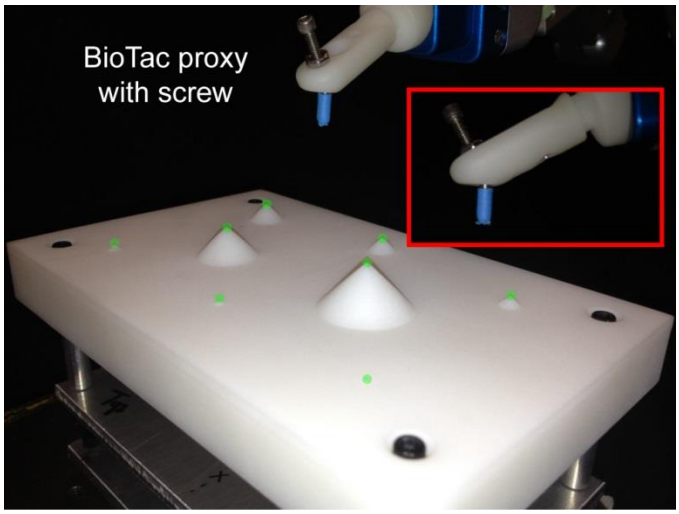

Figure 4.5. Calibration setup to determine the homogeneous transformation that relates the fingertip and test plate frames of reference. A screw was attached to a 3D printed BioTac proxy and made to touch the peak of each conical bump (green dots) as commanded Cartesian positions in the robot reference frame were recorded.

Tactile Data. Representative tactile sensor signals are shown in Fig. 4.6 for all four exploratory procedures for features of all three orders of curvatures. Data correspond to bumps having a footprint dimension of 7.5 mm. Baseline (pre-contact) values were subtracted for all signals on a trial-by-trial basis. For EP #1, the green and red dots indicate the start and end of the middle 30% of contact (*Figure 4.6*). For EP #3, #4, and #5, the green and red dots indicate the initial contact and loss of contact with the geometric feature. Tactile data corresponding to contact with the plate's flat, open surfaces (to the left of the green dot and to the right of the red dot in *Figure 4.6*) were truncated before model input parameters were extracted (*Figure 4.7*). Tactile data for pits having a footprint dimension of 7.5 mm are shown in Appendix *Figure B.2* and *Figure B.3*.

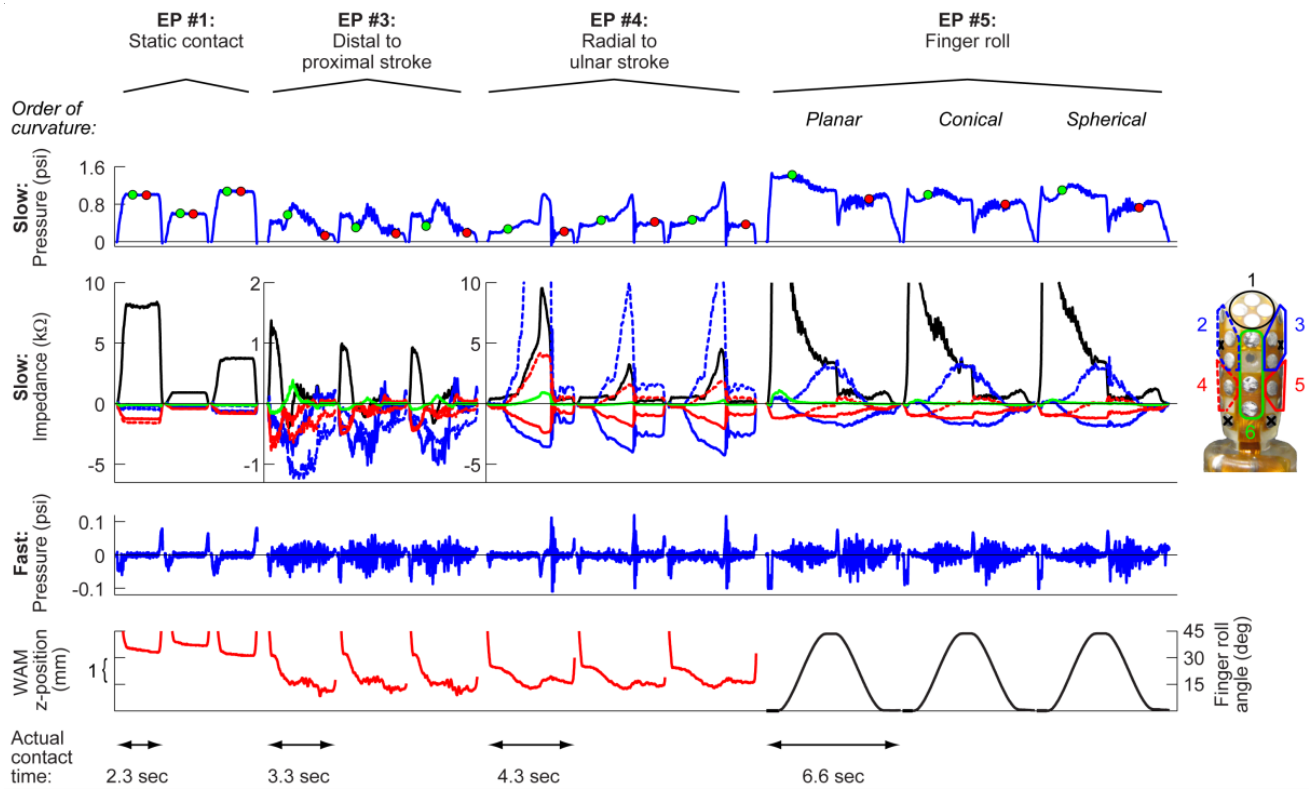

Figure 4.6. Representative multimodal tactile data for a planar, conical, and spherical 7.5 mm bump. Overall fluid pressure (row 1) was used to determine initial contact and loss of contact with the test plate. Only periods of contact with the geometric features (between the green and red dots in row 1) were used to extract model input parameters.

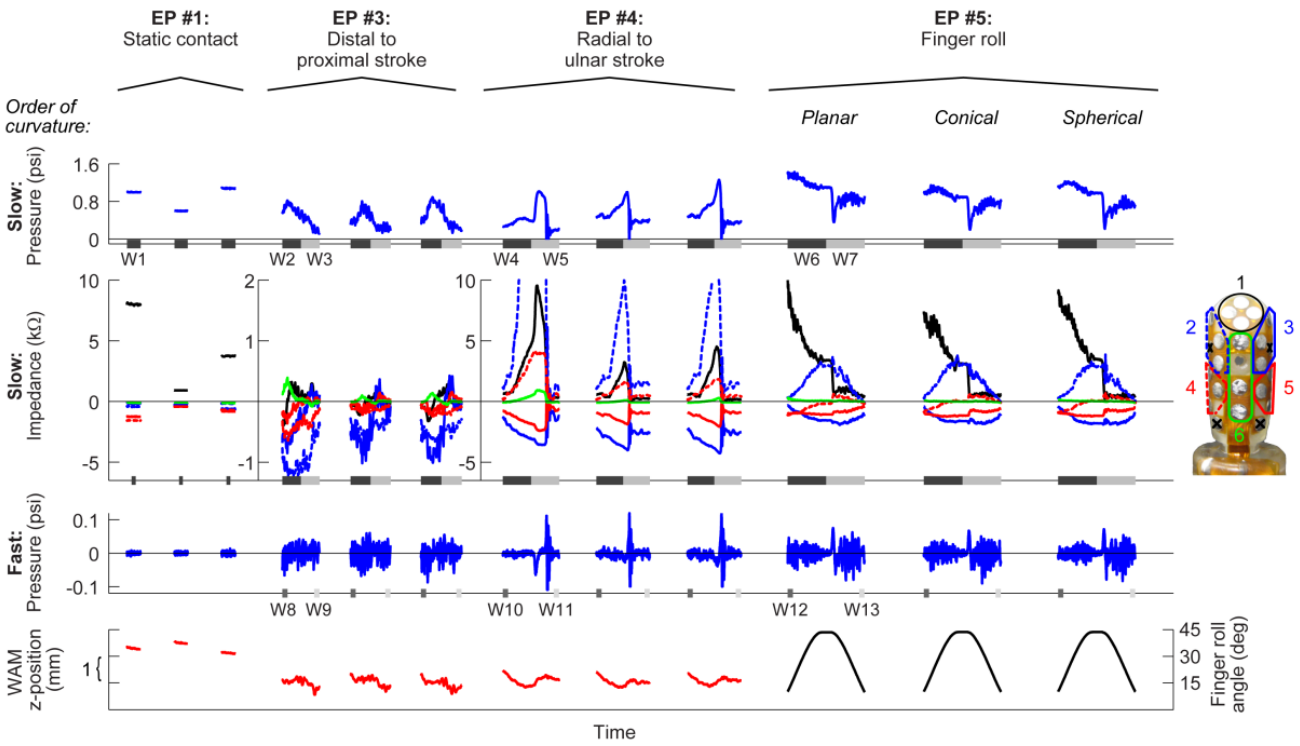

Figure 4.7. Truncated multimodal tactile data for a planar, conical, and spherical 7.5 mm bump. Tactile signals were truncated (from *Figure 4.6*) such that only periods of contact with geometric features were used for modeling. Inputs to the SVC and SVR models were calculated from windows of time (W1-W13) that were specific to each exploratory procedure.

Overall fluid pressure (row 1, *Figure 4.7*) increases as the fingertip makes greater contact with the feature. The stroking exploratory procedures (EP #3, #4) show increases in the pressure signal as the fingertip traverses the bump. Interestingly, the direction of the fingertip trajectory directly affects the trends in the tactile data. The distal-proximal strokes of EP #3 have similar pressure magnitudes with slightly different downward slopes for each order of curvature. The radial-ulnar strokes of EP #4 have different magnitudes and trends for each order of curvature. The finger roll for all orders of curvature yielded similar trends for W6. Fluid pressure dropped sharply at the beginning of W7 when the finger started to roll back to its original 0° orientation.

The electrode impedance data (row 2, *Figure 4.7*) provide information of skin deformation. While an increase in kΩ corresponds to skin compression towards the core, a decrease in kΩ indicates bulging of the skin away from the core. The static contact of EP #1 produced different magnitudes of skin deformation for the different orders of curvature. The linear strokes of EP #3 and #4, the electrode impedance values for the distal clusters differed based on the order of curvature. For the finger roll of EP #5, electrode impedance values were not noticeably affected by order of curvature. The vibration signals (row 3, *Figure 4.7*) were also not noticeably affected by order of curvature or footprint dimension (not shown).

SVC and SVR Model Performance. Table 4.2 consists of model performance results for flow diagram #1 (*Figure 4.4*a) in which SVC and SVR models are run in parallel with all tactile data pooled. The SVC results also apply

to the first step of flow diagram #3 (*Figure 4.4*c). When all 76 inputs are used, both models perform well with the classifier having no misclassification of order of curvature, and the regression model having an R^2 greater than 0.98 and RMS errors smaller than 1.5 mm for footprint dimension.

The SVC created with only EP #3 (distal to proximal linear stroke) performed very well (Table 4.2). Only three trials were misclassified when using a linear kernel, and only two were misclassified when using a quadratic kernel (Table 4.3). These misclassifications resulted from spherical features being predicted as conical features. This was not too surprising given the similarity in the EP #3 tactile data for the conical and spherical bump (*Figure 4.7*). More specifically, a 7.5 mm spherical bump, a 7.5 mm spherical pit, and a 5 mm spherical pit were misclassified in the SVC using a linear kernel. The first two features were misclassified again when using the quadratic kernel. The most accurate SVR model was built when providing input parameters from EP #4 (radial to ulnar linear stroke). When utilizing a linear kernel, the model performed fairly well (*Figure 4.8*a). Using a quadratic kernel improved model performance substantially (Table 4.2).

Table 4.2

SVC and SVR Model Performance for Flow Diagram #1 and Step 1 of Flow Diagram #3

			Classification		**Regression**	
			Order of Curvature		**Dimension (sign indicates bump or pit)**	
EP #	**Polynomial Kernel Order**	**# of Inputs**	**Correctly Classified**	**Accuracy**	**R^2**	**RMS error (mm)**
1	1	7	74/96	0.771	0.866	4.11
1	2	7	80/96	0.833	0.923	3.12
3	1	23	93/96	0.969	0.832	4.63
3	2	23	94/96	0.979	0.958	2.33
4	1	23	83/96	0.865	0.895	3.66
4	2	23	93/96	0.969	0.982	1.49
5	1	23	70/96	0.729	0.853	4.55
5	2	23	83/96	0.865	0.973	1.91
1,3,4,5	1	76	96/96	1.000	0.982	1.48
1,3,4,5	2	76	96/96	1.000	0.997	0.60

Note. Values in red indicate performance of the most accurate linear kernel models when using inputs from only one EP.

Table 4.3

Confusion Matrices for an SVC Model Based on One EP and a Linear Kernel

With inputs from EP #1

0^{th}	1^{st}	2^{nd}	Classified as
26	6	0	0^{th}
0	24	8	1^{st}
0	8	24	2^{nd}

With inputs from EP #3

0^{th}	1^{st}	2^{nd}	Classified as
32	0	0	0^{th}
0	32	0	1^{st}
0	3	29	2^{nd}

With inputs from EP #4

0^{th}	1^{st}	2^{nd}	Classified as
32	0	0	0^{th}
0	22	10	1^{st}
0	3	29	2^{nd}

With inputs from EP #5

0^{th}	1^{st}	2^{nd}	Classified as
25	0	7	0^{th}
3	24	5	1^{st}
10	1	21	2^{nd}

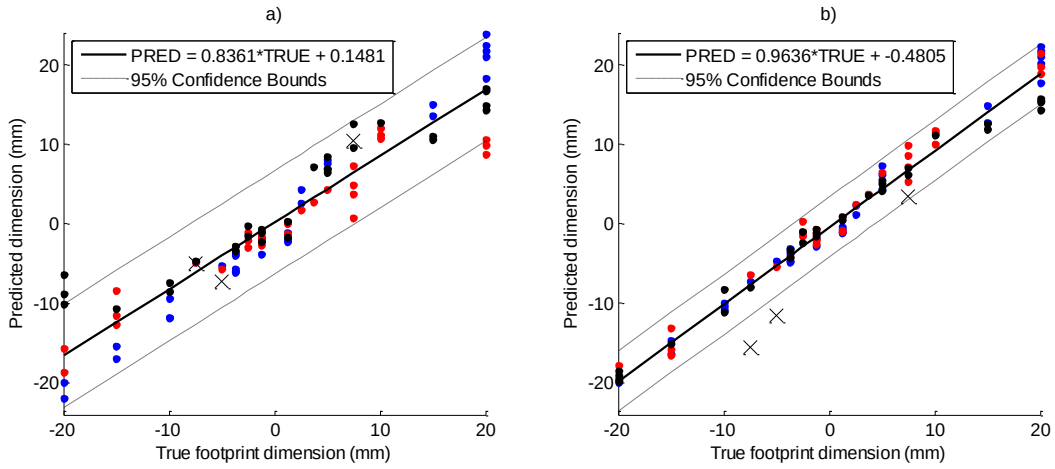

Figure 4.8. SVR model predictions of footprint dimension. a) Predictions corresponding to flow diagram #1 (*Figure 4.4*a), created from a model using a linear kernel and inputs from EP #4 only (results shown in red in Table 4.2). b) Predictions corresponding to flow diagram #3 in which results from three independent SVR models based on order of curvature and using a linear kernel were plotted simultaneously (rows shown in red in Table 4.4). Blue, red, and

black data points correspond to planar, conical, and spherical features. Data points marked with an 'x' had misclassified orders of curvature.

Model performance for the second step of flow diagram #3 (*Figure 4.4*) are shown in Table 4.4. As expected, Table 4.4 shows that curvature-specific SVR models were much more accurate. Figure 4.8b compiles the predictions from all three models, which results in an R^2 of 0.981, and an RMS error in footprint dimension of 1.2 mm. The 95% confidence bounds were tighter for flow diagram #3 than flow diagram #1 (*Figure 4.8*), indicating that predictions were more accurate for the models developed for a specific order of curvature.

Table 4.4

SVR Model Prediction for Data Pooled by Order of Curvature (Step 2 of Flow Diagram #3)

			Regression - Dimension (sign indicates bump or pit)					
			0th Order		**1st Order**		**2nd Order**	
EP #	**Polynomial Kernel Order**	**# of Inputs**	**R^2**	**RMS error (mm)**	**R^2**	**RMS error (mm)**	**R^2**	**RMS error (mm)**
1	1	7	0.895	3.75	0.951	2.42	0.963	2.29
1	2	7	0.939	3.01	0.956	2.18	0.975	1.89
3	1	23	0.868	4.56	0.920	3.00	0.910	3.76
3	2	23	0.992	1.05	0.973	1.65	0.963	2.39
4	1	23	0.988	1.32	0.929	2.81	0.956	2.57
4	2	23	0.998	0.52	0.979	1.49	0.992	1.05
5	1	23	0.926	3.51	0.953	2.29	0.985	2.11
5	2	23	0.973	1.97	0.989	1.06	0.997	0.74
1,3,4,5	1	76	0.995	0.86	0.987	1.15	0.995	0.87
1,3,4,5	2	76	0.998	0.58	0.994	0.79	0.999	0.45

Note. Values in red indicate performance of the most accurate linear kernel models when using inputs from only one EP.

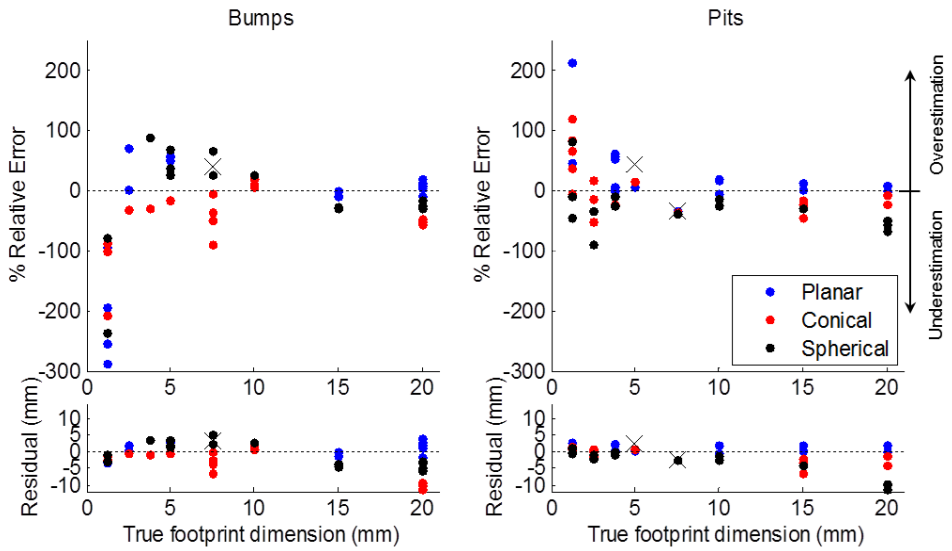

Figure 4.9. Performance metrics for the SVR model predictions corresponding to flow diagram #1 (*Figure 4.4*a). The magnitude of the percent relative error was largest for features (bumps and pits) with the smallest footprint dimensions, with bumps having a maximum underestimation of 300% and pits a maximum overestimation of 200%. Residuals were the largest for features with the largest footprint dimensions with maximum underestimations of 12 mm for bumps and pits. Trials whose order of curvature was misclassified are marked with an 'x.'

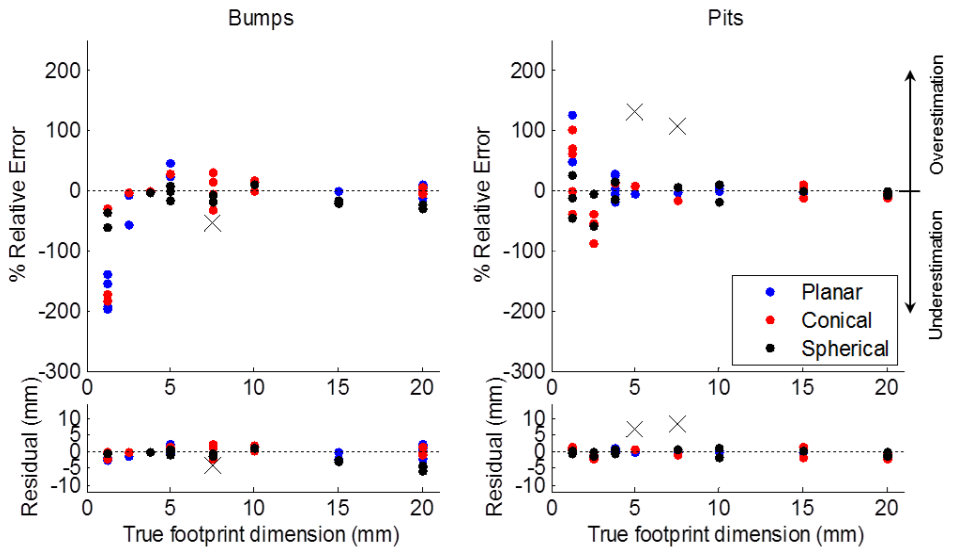

Figure 4.10. Performance metrics for the SVR model predictions corresponding to flow diagram #3 (*Figure 4.4*c). The magnitude of the percent relative error was largest for features (bumps and pits) with the smallest footprint dimensions, with bumps having a maximum underestimation of 200% and pits a maximum overestimation of 125%. Residuals were the largest for features with the largest footprint dimensions with maximum underestimation of bumps of 5.8 mm. Trials whose order of curvature was misclassified are marked with an 'x.'

DISCUSSION

Given the good model performance achieved with simple linear kernels and the fact that these could be used to derive simple equations for faster online predictions in the future, much of the discussion is focused on the results when using the linear kernel.

SVC Prediction of Order of Curvature. We trained 3-class support vector classifiers with tactile data from haptic interactions with features having

three levels of curvature and eight footprint dimensions. The most accurate linear kernel classifiers of curvature were obtained when training the models with inputs from the stroking exploratory procedures, especially the distal-proximal stroke EP #3 (Table 4.2). The two stroking exploratory procedures resulted in misclassifications between conical and spherical features while static contact and finger roll led to errors when classifying the planar features (Table 4.3). This finding suggests that fingertip motion across features provides more information about geometry than keeping the fingertip in a fixed location. It should be noted that, for the purposes of reducing model complexity, spatial resolution of the skin deformation data was purposely reduced by creating clusters of electrodes. It may be possible that static contact could have performed better if all individual electrode impedance values had been provided to the model.

Tactile data obtained from stroking motions were most noticeably affected by order of curvature (*Figure 4.7*). For instance, with EP #3, electrode impedance magnitudes (whether (+) for compression of the skin or (-) for skin bulging) for clusters 1 and 6, along the long axis of the finger, were larger for planar bumps. Cluster 2 on the ulnar side of the finger seemed to be helpful for distinguishing between conical and spherical bumps. Lower accuracies in predictions using EP #3 as compared to EP #4 could be due to the nature of the robot testbed and sensor. Regardless of the feature being explored, a large amount of skin bulging could mask subtle changes in skin deformation associated with order of curvature (see EP #3, cluster 1, 1^{st} and 2^{nd} order curvature). Tactile signals obtained from finger roll were very similar to one another, likely resulting in models with the

least accurate predictions of order of curvature. In the case of static contact, differences in tactile data due to order of curvature became confounded by simultaneous changes in footprint dimension.

SVR Prediction of Footprint Dimension

Flow Diagram #1 (one model using pooled order of curvature data). When comparing SVR models with linear kernels based on pooled order of curvature data, all models had R^2 values greater than 0.83 and RMS errors smaller than 4.6 mm (Table 4.2). Although these models might be acceptable, there is room for improvement. *Figure 4.8*a shows the predictions when using only inputs from EP #4. When using all 76 inputs from all four exploratory procedures, a much greater accuracy is obtained. However, in practice, this suggests that all the exploratory procedures would need to be performed on a feature and all their data post-processed accordingly, in order to achieve high accuracies with a linear model. Thus, flow diagram #1 might not be recommendable.

The percent relative error (*Figure 4.9*) for the footprint dimension predictions were the largest for the bumps and pits with the smallest footprint dimensions. This was not surprising given that the small sizes of these footprint dimensions required accurate predictions in order to avoid large relative errors (due to division by a very small number). The smaller the footprint dimension, the smaller the contact area of the feature with the fingertip, and the smaller the degree of stimulation of the tactile sensor. As a result, trends in the electrode impedance signals were not as distinctive for features with smaller footprint dimensions, which likely resulted in greater relative errors.

Flow Diagram #3 (separate models that are specific to order of curvature). Prediction accuracy for footprint dimension increased dramatically if we first use the SVC predictions to choose one of three curvature-specific SVR models (Table 4.4, *Figure 4.8*b). For instance, if a sample was classified as 0^{th} order, the sample would be sent to the SVR model specifically for predicting footprint dimensions of 0^{th} order of curvature features. Not surprisingly, the largest prediction errors in footprint dimension occurred when samples were misclassified in the previous step of flow diagram #3 (see "x" markers in *Figure 4.8*b). Nevertheless, the overall SVR prediction accuracy was much greater for flow diagram #1 than for flow diagram #3, as indicated by the near one-to-one relationship between the true and predicted footprint dimensions and the tighter 95% confidence bounds (*Figure 4.8*b).

The independent SVR models performed as well, if not better, with model inputs from a single exploratory procedure as compared to the single SVR model created using all four exploratory procedures. When curvature-specific models were created, EP #4 was most useful for predicting footprint dimensions for 0^{th} order curvature while EP #5 was most useful for 1^{st} and 2^{nd} order curvatures. Apparently, finger roll can be used to estimate footprint dimension well, but not order of curvature (Table 4.2, Table 4.4). Since acceptable curvature-specific models could be developed using inputs from a single exploratory procedure and a linear kernel function, computation time during online tasks should not be an issue. A parallelized version of flow diagram #3 (*Figure 4.4*c) could also be used if parallel computing was incorporated into the robot system.

Similar to the flow diagram #1 predictions, the percent relative error of flow diagram #3 (*Figure 4.10*) for the footprint dimension predictions were largest for features with the smallest footprint dimensions and for those trials whose order of curvature were misclassified. Nevertheless, no prediction exceeded a relative error of 200%, indicating that the curvature-specific SVR predictions of flow diagram #3 (*Figure 4.4*c) were more accurate than those from the flow diagram #1 (*Figure 4.4*a). The residuals were no larger than 5.8 mm for the trials whose order of curvature were correctly classified.

Effects of the Exploratory Procedure. *Figure 4.7* illustrates how each exploratory procedure affects the trends in the tactile data and, subsequently, the performance of the supervised learning models. EP #1 consists of the fingertip moving to a predefined z-position to apply a static force on the feature for a prescribed duration. The slow-adapting overall fluid pressure and electrode impedance signals were affected by the amount of contact area with the feature. The stroking exploratory procedures resulted in wider ranges of tactile signals. The compliance of the BarrettHand combined with the shape of the deformable BioTac skin, allowed much smoother movements along the distal-proximal, y-axis. Due to the kinematics of the BarrettHand finger, the BioTac did not get temporarily stuck against bumps or within pits for distal to proximal EP #3 as much as with radial to ulnar EP #4. The increased resistance that the fingertip had to overcome during the radial to ulnar EP#4 did not allow a smooth exploration of the feature, resulting in errors when discriminating between conical and spherical features. As the finger supinates about its longitudinal axis, the ulnar side of the

fingertip experiences skin compression and the radial side experiences bulging (row 2, *Figure 4.7*).

The distal to proximal stroke (EP #3) was most efficient for predicting the order of curvature of a feature (red SVC results in Table 4.2). Given that this exploratory procedure moved the fingertip across each feature with the least amount of resistance, the order of curvature might be more easily encoded in the BioTac signals compared to the other exploratory procedures. The radial to ulnar stroke (EP #4) performed the second best with an accuracy of 83/96 (86%), with all misclassifications occurring between conical and spherical features. The static contact (EP #1) and finger roll (EP #5) exploratory procedures performed the worst with classification accuracies lower than 78%. Exploratory procedures involving stroking motions seemed better suited for estimation of order of curvature, although the distal to proximal stroke (EP #3) performed slightly better than the radial to ulnar stroke (EP #4).

When no prior information was known about the feature's order of curvature (flow diagram #1, *Figure 4.4*a), EP #4 was most efficient for predicting footprint dimension and whether the feature was a bump or a pit (red SVR results in Table 4.2). This suggests that footprint dimension was encoded in the skin deformation experienced while stroking the feature in the radial to ulnar direction. For order of curvature classification, the distal to proximal stroke was highly preferred over the other three exploratory procedures. For footprint dimension estimation, selection of the exploratory procedure was not as critical. The other three exploratory procedures yielded R^2 values ranging from 0.83 to 0.87 and

RMS errors ranging from 4.1 to 4.6°, which were not very different from the performance metrics for EP #4 (R^2 of 0.90 and RMS error of 3.7°).

The three independent SVR models created for specific order of curvature (flow diagram #3, *Figure 4.4*c) returned some interesting results. While footprint dimensions of planar features were better estimated using a radial to ulnar stroke (EP #4), the footprint dimensions of conical and spherical features were more accurately estimated with finger roll (EP #5). The radial to ulnar stroke may have been most informative for planar features because planar bumps produced the most resistance to fingertip motion and resulted strong skin deformation trendsthat were distinct from those for conical and spherical features (*Figure 4.7*). On the other hand, planar pits produced the least resistance to fingertip movement out of all types of features, but still yielded useful skin deformation trends for planar pits (*Figure B.2* and *Figure B.3*). The amplitude and duration of these step-like changes in electrode impedance apparently encoded footprint dimension of planar features well. The finding that finger roll was the most helpful for estimating footprint dimension for both conical and spherical features (Table 4.3) makes sense considering that the order of curvature of conical and spherical features might be perceived similarly at such small scales.

In terms of the usefulness of each exploratory procedure, the SVR model for 0^{th} order features performed best with model inputs from EP #4. Although the SVR model for 1^{st} order features performed best with model inputs from EP #5 (finger roll), the model was not greatly affected by exploratory procedure. For the 2^{nd} order curvature model, the distal to proximal stroke (EP #3) performed the

worst. Any of the other three exploratory procedures would provide useful inputs for predicting footprint dimensions of 2nd order features, although finger roll (EP #5) was recommended due to its slightly superior performance.

Our results highlight the importance of considering the information content of different exploratory procedures when characterizing small geometric features by touch alone. Static contact alone was not sufficient to estimate order of curvature or footprint dimension while dynamic fingertip motions yielded tactile data that did encode such properties.

WAM Proprioception Data. WAM proprioception data on 3D fingertip position and orientation were recorded in the form of Cartesian positions and quaternion vectors. While the quaternion vectors provided clean signals for finger roll, the z-position data was very noisy. No clear trends were observed in the fingertip position data that could have provided information about footprint dimension or height/depth (z-dimension) of the features. Cartesian position changes at small scales (tallest bumps were 2.5 mm high, and deepest pits were 2.5 mm deep) could not be precisely detected by the WAM. Resolution of the z-position data appeared to be on the order of 2.5 mm. This imprecision is likely due to a combination of factors. The WAM/BarrettHand combination does not seem to be suited for precise characterization of the small geometric features used in this study. In addition, the fingertip sensor was deformable and small features sensed by the BioTac skin would not cause noticeable changes in WAM end-effector position, especially given the degree of gear lash in the BarrettHand.

Despite these limitations in the robot testbed, SVR models could be successfully trained to perform well on the feature characterization task.

Limitations. A main assumption in this proof-of-concept study was that the 3D location and orientation of each feature with respect to the fingertip were known *a priori*. That is, the location of each feature on the test plate, whose global reference frame was aligned to the robot reference frame, was used to define the fingertip motion trajectories. In real world situations with unstructured environments, the location of features would not be known a priori and would need to be estimated using visual feedback or by performing a raster-like scanning for patterns (Huynh et al., 2010). The algorithms presented in this study could then be applied once a crude estimate of the position and orientation of the feature had been determined, and could even be used to update estimates of feature location and orientation with each new haptic experience. Regardless of whether visual feedback was used initially, the fact remains that finger-sized features would be occluded during touch and that real-time visual feedback would be rendered useless at that point.

As with the edge orientation study, the WAM was calibrated and its tendons re-tensioned in order to reduce variability when performing the exploratory procedures. The BarrettHand fingers are compliant due to gear lash in the worm gear mechanism, which results in inadequate precision for haptic exploration of such small geometric features. In addition, the WAM wrist has a lot of lash, which became apparent when performing radial to ulnar strokes. An interesting finding from this work is that the kinematics and compliance of the

actor (robot) itself can affect the implementation of exploratory procedures and, subsequently, the nature of the tactile data obtained via those exploratory procedures. Nevertheless, supervised learning model performance was acceptable despite variability and imprecision in our robot testbed.

While the post-processing methods presented here are admittedly *ad hoc*, it is not unreasonable to process data differently based on the type of exploratory procedure used. For instance, it makes sense to use a fixed period of data for static contact EP #1 because tactile signals would not be expected to change. Rates of skin deformation, however, would be more useful for dynamic fingertip motions. The important process of relating known voluntary actions to perception of tactile stimuli can happen at two different levels: (i) selection of an exploratory procedure based on its efficiency and accuracy for predicting specific properties, and (ii) processing of signals specific to the exploratory procedure that generated them. Such *ad hoc* approaches are used in biological systems all the time in the form of trial and error, model-building based on experience, and learning over one's lifetime about which actions to take, which afferent feedback streams to pay attention to, and how those signals should be processed. For practical reasons, the post-processing methods for this study on geometric features were designed to be identical, or closely related, to those from the study on edge orientation. Thus, if one did not know *a priori* whether an edge or geometric feature would be encountered, the tactile data could be processed similarly for either type of model.

SUMMARY

This study provides insights as to which exploratory procedures (actions) yield the most informative tactile and proprioceptive data for characterization of small, finger-sized geometric features. Understanding the geometric properties of small features would be useful when vision is obstructed (such as when lighting is not appropriate or even when the finger itself blocks the line of vision) and when proprioceptive feedback is inadequate for the characterization task. Haptic perception abilities that we take for granted (e.g., finding a USB port, power button, or screw hole without looking) remain grand challenges for artificial hands. As in the edge orientation study, the use of a deformable, bladder-type sensor seems well-suited for advancing the haptic intelligence of robotic systems. Rigid, planar sensors might not be able to determine the curvature of small bumps or pits, for example. The top surface of conical or spherical features would appear as point-like indentations on a rigid, planar sensor.

Future work includes developing an analytical solution for footprint dimension using some of the input parameters fed into the supervised learning models. Although models using quadratic kernels could provide more accurate predictions, models with linear kernels would allow us to derive linear equations to estimate footprint dimensions. Furthermore, computation time could be decreased by reducing the number of input variables fed to the models. Thus, algorithms could be implemented to find efficient sets of inputs.

In this study, contact time was normalized by splitting the tactile data into separate windows. However, actual contact duration in seconds, coupled with the

known stroking speed, could potentially be used as model inputs to for estimating footprint dimension. Incorporating estimated contact duration into models might be challenging given that accurate predictions of initial contact and loss of contact with features, in particular, may be especially important. Irrelevant tactile data from arbitrary object contact (e.g., flat surfaces in between features of interest) could confuse the models. Thus, it would still be useful to understand the subtleties of the tactile data (especially skin deformation) in order to know when initial contact and loss of contact with a feature occurred.

For implementation in robotics, learning and adaptation approaches are becoming increasingly popular. As such, algorithms such as Bayesian learning (J. A. Fishel & Loeb, 2012) and reinforcement learning (Pape et al., 2012) could be implemented to enhance the presented work. In addition, a wider range of features could be explored to develop more generalizable models. The features used in this study were all symmetric and their heights were constrained to no greater than 2.5 mm. Features with more complex 3D shapes such as elliptical bumps or trapezoidal pits could be explored to develop more general methods. Finally, estimates of height or depth could be used in conjunction with estimates of order of curvature and footprint dimension in order to calculate interior angle of conical features or radius of curvature of spherical features.

CHAPTER 5

SUMMARY AND CONCLUSIONS

We have shown that deformable, fluidic sensors have great potential for use as tactile sensors for artificial fingertips. The microfluidic sensor skin and the multimodal BioTac sensor, had desirable characteristics such as robustness to substantial deformation and sensitivity to light touch. By implementing multiple exploratory procedures with the BioTac, accurate predictions of edge orientation and characterization of finger-sized geometric features were achieved. Enhancing the haptic intelligence of artificial hands would greatly increase their usefulness for quality of life applications such as prosthetics and wheelchair-mounted robots.

The tight relationship between known voluntary actions and perception of tactile stimuli can occur at two different levels. At one level, an exploratory procedure can be selected based on its efficiency and accuracy for predicting specific object properties of interest. For instance, our work suggests that information about a small feature's order of curvature is better estimated with a distal to proximal stroke. At another level, tactile signals can be processed and interpreted as a function of the exploratory procedure that was selected. For example, if a static contact EP had been performed, it may not be worthwhile to interpret fast-adapting tactile signals or rates of change of slow-adapting tactile signals.

Another interesting observation was that haptic perception could be affected by unplanned actions. Our robot haptic perception studies suggest that special attention needs to be placed on the properties of the robot testbed itself.

Specifically for our setup, the kinematics and compliance of the robot coupled with the deformable nature of our tactile sensor affected the implementation of exploratory procedures and, subsequently, the nature of the tactile data obtained via those exploratory procedures. For example, robot stroking motions that were commanded to be identical in terms of stroke speed and smoothness would be different when implemented because of differences in compliance of the BarrettHand finger and wrist for distal to proximal strokes as compared to radial to ulnar strokes. Knowledge of the kinematic capabilities and limitations of one's robot testbed could be used to better understand the usefulness of different exploratory procedures and to select the most efficient action for a given haptic perception task.

BIO-INSPIRED VERSUS BIOMIMETIC APPROACHES

While human capabilities are typically considered as the gold standard for many robotics applications, we recognize that a robot testbed and its sensors do not need to exactly mimic their biological counterparts. Although multimodal, the BioTac is not comparable to the human fingertip with regards to mechanotransduction mechanisms, sensitivity, or range. These limitations are not specific to the BioTac; rather, they exist for all engineered tactile sensors. Nonetheless, we have shown that a multimodal tactile sensor such as the BioTac still provides tactile information (as proxies for biological tactile feedback) that can be used to haptically determine edge orientation and characterize small geometric features.

State-of-the-art artificial tactile sensors are inherently limited, but certain human capabilities can be mimicked with current technology and post-processing algorithms. One tactile sensor has been used to read Braille (Bologna et al., 2012). In an online experiment, 89% of the Braille characters were accurately identified. Firing patterns of a 6 x 4 flat array of capacitive taxels were used to make predictions. Although the tactile sensor was not comparable to the biological mechanotransducers in human fingertips, a pattern recognition, Braille-reading capability was demonstrated.

A general approach of providing human-like tactile capabilities to artificial hands consists of exploiting artificial sensing capabilities and relating them to physical phenomena and high-level abstractions used by humans for decision-making processes. For instance, consider the compression of the BioTac skin towards the sensor core (indicated by an increase in electrode impedance) over an ulnar aspect of the sensor and simultaneous bulging of the skin away from the sensor core (indicated by a decrease in electrode impedance) over a radial aspect of the sensor. The spatiotemporal trends in electrode impedance signals could, as a proxy for skin deformation, indicate shear forces applied to the fingertip in the radial direction. Although not exactly biomimetic, such bio-inspired interpretations of artificial sensory feedback could facilitate inferences about the environment. Other robot testbeds and sensors could implement the methods described in this dissertation as long as they can measure tactile signals that encode the characteristic features of interest. Our experience suggests that signals that can be related to skin deformation and contact force could work well

for tasks such as edge orientation and characterization of small geometric features. The tactile sensor and its raw signals need not be identical to those of the BioTac tactile sensor as long as they can be related to physical phenomena such as those described in our work.

Applications for neuroprosthetics. Neuroprosthetics seek to restore motor or sensory capabilities that have been lost or impaired due to injuries or disease. A grand challenge in the field of neuroprosthetics is the restoration of a conscious perception of touch to amputees (Romo et al., 1998). One technique that is currently being pursued is intracortical microstimulation (ICMS), which consists of repetitive application of electrical pulses via microelectrodes on the somatosensory cortex [Springer Encyclopedia of Neuroscience]. Studies suggest that amputees could benefit from ICMS-driven sensory feedback associated with robotic prostheses (O'Doherty et al., 2011). However, the proper delivery of a meaningful sensor signal to the brain or nervous system remains a challenge. Raw artificial tactile signals, such as those provided by the BioTac sensor or any other engineered tactile sensor, are not equivalent to biological tactile signals.

While humans excel at learning novel tasks, it is likely that artificial tactile signals will still need to be post-processed and interpreted before being sent to the human nervous system. As our studies have shown, physical interpretations of properties such as edge orientation and a feature size could be successfully extracted. Similarly, high-level abstractions could be extracted from raw artificial sensor signals to drive ICMS delivery for neuroprosthetic purposes. There is currently no consensus as to the types of information that should be provided to

an amputee via ICMS, although contact force, contact location, and posture are commonly considered. One study focused on the effectiveness of electrical stimulation in the proprioceptive region of the somatosensory cortex to deliver proprioceptive sensations to a monkey (London, Jordan, Jackson, & Miller, 2008). Although more work is needed for use in human neuroprostheses, the study showed that monkeys were capable of detecting brief stimulus trains and could discriminate between trains of varying frequency as proxies for hand position.

Importance of proprioception in biological systems. Although there is strong evidence that biological tactile sensors play critical roles in detecting local shape and curvature (R. L. Klatzky & Lederman, 1999; R. H. LaMotte & Srinivasan, 1987), it is also possible that biological proprioceptive sensors could contribute as well. Proprioceptive feedback from the human finger is so sensitive that contact by a von Frey hair (with diameters ranging from 0.28 to 0.68 mm) can be detected. One study evaluated the properties of finger contact and the contacted object for postural stabilization in humans (Lackner, Rabin, & DiZio, 2001). Fingertip force levels as low as 10 g contributed to postural stabilization. Tactile sensing, coupled with brachial proprioceptive information about finger position with respect to the torso, enabled subjects to stabilize their posture.

One study found that the availability of receptors in the skin, muscles, and joints give proprioceptive acuity to the distal joint of the middle finger (Gandevia, Hall, McCloskey, & Potter, 1983). A study on the proprioceptive ability of the proximal interphalangeal and metacarpophalangeal joints of the index finger

showed that even sensory input from skin regions that are not stretched or deformed by joint rotation can influence proprioceptive sensibility (Clark, Burgess, & Chapin, 1986). Another study suggested that mechanoreceptors in non-glabrous skin provides information on joint configuration and may play a specific role in proprioception (Edin, 1992). Given the robot testbed used in our studies, it is unlikely that artificial proprioception could have been as useful as biological proprioception for the haptic exploration tasks. However, just because this particular robot testbed was limited in proprioceptive sensitivity for these tasks does not mean that proprioception should be discounted as a viable feedback source entirely.

MAJOR CONTRIBUTIONS

Novel approach for tactile sensor fabrication. Although other sensors had incorporated fluids in various forms, the use of conductive fluids as both electrical interconnects and capacitive sensing units in microfluidic devices had not been attempted before. The journal publication based on material presented in Chapter 2 (Ponce Wong et al., 2012), has been highly cited and highlighted in two recent journal publications (Nawaz, Mao, Stratton, & Huang, 2013; Zuidhoek, Dokmeci, Annabiab, & Khademhosseini, 2012). These articles emphasize the sensor's advantageous characteristics such as tunable sensitivity, flexibility, and robustness. A non-provisional U.S. patent application was also filed earlier this year (Santos, Posner, & Ponce Wong, 2013).

Fluidic capacitive sensing units could also be exploited in other types of electronic devices. With the boom in capacitive touch screen technology, conductive fluids embedded in elastomers could be used for chemically inert, highly flexible tactile displays, for example. The novel use of the non-toxic liquid metal alloy Galinstan could inspire research on material properties of other fluids that might possess desirable characteristics at scales that rigid metals would not.

Dynamic approach to artificial haptic perception. The methods presented in the studies on edge orientation and characterization of finger-sized geometric features are applicable to any tactile sensor designed to measure slow- and fast-adapting stimuli. We suggest that action and perception are so tightly coupled that (i) efficiency and accuracy of different exploratory procedures should be considered, and (ii) post-processing of tactile data can and should be specific to the exploratory action that generated the data. For instance, tactile data generated by actions that are expected to be symmetric, such as roll of a finger to a specific angle and back, might be useful if split into two equal phases of contact with a feature of interest. Instead of using "tactile images" based on a static snapshot of a tactile data stream, tactile data throughout a dynamic fingertip movement were used. By knowing which exploratory procedure was implemented and the type of information sought about the object, we can partition the tactile data into appropriate subphases (windows) and extract haptic cues that are specific to the sensing mode. Furthermore, the fingertip reference frame can be combined with knowledge of the exploratory procedure in order to determine which modes or channels of tactile data would be best suited to encode property

information. For instance, impedance electrodes located on the distal, ulnar aspect of the fingertip are especially useful for radial to ulnar fingertip motions.

One of the most interesting findings was that skin deformation resulting from bulging, especially far from the actual finger-object contact area, can also encode information about geometric features such as edges, bumps, and pits. The kinematics and compliance of the hand itself can affect the quality of the tactile data. Subtle differences in the exploratory procedure, even the nature of the initial finger-object contact, can affect trends in skin deformation signals.

Haptic exploration of object shape. The robotics literature on haptics-based characterization of finger-sized geometric features is scarce. We have shown that it is possible to use tactile data alone in order to accurately identify and characterize small features such as bumps and pits that would be occluded from computer vision systems by the robot finger itself. It is not being suggested that tactile feedback be used in place of visual feedback altogether. Rather, tactile feedback can be used to supplement information obtained visually and is especially effective when visual feedback is inadequate. Proprioceptive feedback also provides alternative, temporally synchronous feedback on physical interactions with the environment and should be considered. However, as shown in Chapter 4, proprioceptive data may be imprecise depending on the composition and capabilities of the robot testbed as well as the nature of the task. Clearly, the combination of the tendon-driven Barrett WAM coupled with the deformable BioTac tactile sensor precluded the use of end-effector position as a means to characterize finger-sized geometric features. We have shown that robotic systems

having deformable, multimodal tactile sensors can be used for haptic perception at levels of accuracy that are comparable to those of humans for edge orientation.

Furthermore, the regression models developed enable estimation of feature properties from a continuous number line. This approach is a methodological departure from the recent publications on classification models, which are used to separate items according to discrete classes and may not generalize to novel experiences that lie on a continuum between classes selected *a priori*. As shown in Chapter 4, there is a time and place for discrete classification (e.g., for 0^{th}, 1^{st}, and 2^{nd} order curvature), but regression should be considered whenever possible.

FUTURE WORK

Expanding the capabilities of the microfluidic tactile sensor skin. As robust and functional as our microfluidic tactile sensor skin is, the current prototype can only measure normal forces. In order to enhance its usefulness as a fingertip sensor, additional modalities could be developed so that the skin can measure shear force, strain, and high frequency vibrations. For instance, the addition of bumps to the sensor's surface could be used for shear stress measurements (Hyung-Kew Lee et al., 2008). While originally designed for normal forces only, by adding bumps to the sensing surface, relative changes in capacitance would quantify shear forces. More complex microchannel patterns could also be designed to measure changes in resistance and capacitance of the fluidic wires that are associated with strain (Fassler & Majidi, 2013; Y.-L. Park et al., 2012). Taxels having different sensing modalities could be interlaced within a

single layer of skin or stacked via multiple modality-specific layers of skin.

Although it is possible, we have not yet attempted to tune the sensor's architecture or PDMS characteristics for improved normal force sensitivity and range. With the presented fabrication protocol, our sensor was sensitive to forces ranging from 0 to 2.5 N. Similar capacitance-based sensors, composed of PDMS and thin metal films, have been created. One sensor designed for use as an artificial skin for robots had a sensitivity of 3%/mN and a sensing range of 0-250 kPa (H.-K. Lee et al., 2006). Another sensor developed for plantar pressure measurements had a sensitivity of 6.8%/N and a sensing range of 0-945 kPa (Lei, Lee, & Lee, 2012). These studies demonstrate that the sensor skin design could be tuned for a wide range of applications and technical specifications. We could attempt to increase normal force sensitivity, for instance, by increasing the height of the air pockets (*Figure 2.2*) to make the taxels even more compliant.

Developing mathematical models of deformable, fluidic tactile sensors. There are currently no finite element or multiphysics models for either the microfluidic tactile sensor skin (Chapter 2) or the BioTac sensor (SynTouch). The structural mechanics of the tactile sensor skin are different to simulate under loading conditions. The complexity arises because an incompressible fluid is encapsulated within microchannels embedded in an elastomer. Fluids are not typically simulated in structural deformation scenarios such as this one.

A similar challenge arises with modeling of the BioTac sensor. A complete analytical, multiphysics model of the BioTac sensor would have to address deformation of an elastic skin, incompressible fluid, electrostatics, and

fluid vibration. Modeling the structural mechanics of the BioTac skin under load would be difficult on its own. A standard approach would be to model how changes in the internal fluid pressure would affect skin deformation. However, the compression and bulging of the skin would depend on contact area and forces associated with the the finger-object interaction. As seen in Chapter 3, the difference in initial contact between the normal and tangential approaches of the fingertip to a stimulus surface greatly affects the subsequent trends in skin deformation. A much simplified model of the BioTac fingerpad could be developed similar to the two-dimensional finite-element model of the non-human primate fingertip (M. A. Srinivasan & Dandekar, 1996). The finite-element model predicted that shear strain sensors would be effective in robot tactile sensing systems if edge detection capabilities were desired. However, a mathematical model is still sought that can effectively relate fingerpad deformation to observed spatial response patterns of the embedded tactile afferents (M. A. Srinivasan & Dandekar, 1992, 1996).

Fitting models based on experimental parameter conditions. The models for the prediction of edge orientation and characterization of small geometric features were trained using only tactile sensor signals and stroke speed (in the case of the edge orientation studies). The resulting models had high levels of accuracy despite the fact that information about experimental conditions, such as fingertip contact angle and contact force, were not provided to the models. This was viewed as a benefit given that less model inputs were required for training and testing, and predictions could be made accurately over a broad range

of experimental conditions without explicit specification of contact force, for example. At least for our studies, features of interest were encoded sufficiently by the multimodal tactile data.

One approach to achieve even greater accuracies would be to train models on specific experimental conditions. This would require establishing an exhaustive library of models before analyzing new data. There would have to be one model for every possible set of experimental conditions. For instance, in the case of our edge orientation study, we would need to create 24 models (three stimulus widths, two contact angles, two stroke speeds, two commanded heights). However, trade-offs for the benefit of greater accuracy include the burden of having to develop *a priori* knowledge of all experimental conditions. It is neither realistic to know all contact conditions for unstructured finger-object interactions *a priori* nor practical to build a multitude of models when one or two models would suffice. Nevertheless, it would be interesting to assess potential improvements in performance attained with such specific models as compared to performance by the models developed in this work. It is expected that performance would improve only slightly. Experimental parameters such as the contact angle and commanded height could be treated as numerical input parameters given the continuum nature of their possible values.

Haptic exploration of complex 3D objects. For practical reasons, the tactile stimuli used in the haptic exploration studies were constrained in the sense that edges were straight, bars were rectangular, surfaces were flat, features were perfectly spherical, etc. It would be interesting to see how the current support

vector models would perform if such constraints were released. For instance, the effect of rounder edges on estimation of edge orientation could be explored. The edge orientation models could also be used for studies on single digit contour-following of straight and curved edges, as well as identification of vertices. The models for finger-sized geometric features could be tested on non-ideal shapes such as buttons and heads of screws.

Once a foundation for single digit haptic exploration is established, haptic information obtained simultaneously from multiple digits will need to be integrated and used to identify and characterize the object on which features such as edges and bumps are actually just subcomponents. Eventually, the methods proposed here will need to be validated on real-world 3D objects used in activities of daily living for translation to applications that can improve quality of life.

A more precise robot testbed could be used to further investigate the usefulness of proprioceptive feedback. For instance, haptic exploration experiments on edge orientation and characterization of finger-sized geometric features could be repeated using a robot arm with direct drive motors at each joint. While nonzero gear lash might still exist, control of end-effector position might be more precise and repeatable. This could enable the use of proprioceptive signals in addition to tactile signals for characterizing geometric features.

Using learning to update models. In this work, we used supervised learning to estimate properties of different object features. Support vector machine models built with training data were accurate, but the models remained

constant. For long term and online implementation of haptic explorations, this is not ideal. The use of incremental support vector machine learning could be implemented so that the model can learn with each new experience (Cauwenberghs & Poggio, 2001) Switching from SVM modeling to a Bayesian approach is another alternative, as it would allow the database of prior information to be updated as in (Xu et al., 2013). The database could be appended for long-term memory of haptic experiences or truncated to most recent trials for short-term memory.

REFERENCES

Abdullah. (2011). Object Exploration Using a Three-Axis Tactile Sensing Information. *Journal of Computer Science, 7*(4), 499–504. doi:10.3844/jcssp.2011.499.504

Adrega, T., & Lacour, S. (2010). Stretchable gold conductors embedded in PDMS and patterned by photolithography: fabrication and electromechanical characterization. *Journal of Micromechanics and Microengineering*, *20*, 055025.

Aiken, L. R. (2004). *Assessment of Intellectual Functioning*. Springer.

Allen, P. K., & Michelman, P. (1990). Acquisition and interpretation of 3-D sensor data from touch. *IEEE Transactions on Robotics and Automation*, *6*(4), 397 –404. doi:10.1109/70.59353

Atkins, D. J., Heard, D. C. Y., & Donovan, W. H. (1996). Epidemiologic Overview of lndividuals with Upper-Limb Loss and Their Reported Research Priorities. *J Prosthetics and Orthotics*, *8*(1), 2–11.

Baeten, J., & De Schutter, J. (2002). Hybrid Vision/Force Control at Corners in Planar Robotic-Contour Following. *IEEE/ASME Transactions on Mechatronics*, *7*(2), 143 –151. doi:10.1109/TMECH.2002.1011251

Baeten, Johan, Verdonck, W., Bruyninckx, H., & De Schutter, J. (2000). Combining Force Control and Visual Servoing for Planar Contour Following. *Int. J. of Machine Intelligence and Robotic Control*, *2*(2), 69–75.

Belter, J. T., & Dollar, A. M. (2011). Performance characteristics of anthropomorphic prosthetic hands. In *Proc IEEE Intl Conf Rehab Robotics* (pp. 1–7). Retrieved from http://ieeexplore.ieee.org/xpls/abs_all.jsp?arnumber=5975476

Bensmaia, S. J., Hsiao, S. S., Denchev, P. V., Killebrew, J. H., & Craig, J. C. (2008). The Tactile Perception of Stimulus Orientation. *Somatosensory & motor research*, *25*(1), 49–59.

Bensmaia, Sliman J., Denchev, P. V., Dammann, J. F., Craig, J. C., & Hsiao, S. S. (2008). The Representation of Stimulus Orientation in the Early Stages of Somatosensory Processing. *The Journal of Neuroscience*, *28*(3), 776–786. doi:10.1523/JNEUROSCI.4162-07.2008

Berger, A. D., & Khosla, P. K. (1991). Using Tactile Data for Real-Time Feedback. *The International Journal of Robotics Research*, *10*(2), 88–102.

doi:10.1177/027836499101000202

Besl, P. J., & McKay, N. D. (1992). A method for registration of 3-D shapes. *IEEE Transactions on Pattern Analysis and Machine Intelligence*, *14*(2), 239–256. doi:10.1109/34.121791

Bologna, L. L., Pinoteau, J., Garrido, J., & Arleo, A. (2012). Active tactile sensing in a neurorobotic Braille-reading system. In *2012 4th IEEE RAS EMBS International Conference on Biomedical Robotics and Biomechatronics (BioRob)* (pp. 1925 –1930). Presented at the 2012 4th IEEE RAS EMBS International Conference on Biomedical Robotics and Biomechatronics (BioRob). doi:10.1109/BioRob.2012.6290937

Cauwenberghs, G., & Poggio, T. (2001). Incremental and decremental support vector machine learning. *Advances in neural information processing systems*, 409–415.

Cheng, M.-Y., Tsao, C.-M., Lai, Y.-Z., & Yang, Y.-J. (2011). The development of a highly twistable tactile sensing array with stretchable helical electrodes. *Sensors and Actuators A: Physical*, *166*(2), 226–233.

Ciocarlie, M. T., & Allen, P. K. (2008). On-Line Interactive Dexterous Grasping. In *Proceedings of the 6th international conference on Haptics: Perception, Devices and Scenarios* (pp. 104–113). Madrid, Spain: Springer-Verlag. Retrieved from http://portal.acm.org/citation.cfm?id=1423785

Cipriani, C., Antfolk, C., Balkenius, C., Rosen, B., Lundborg, G., Carrozza, M. C., & Sebelius, F. (2009). A novel concept for a prosthetic hand with a bidirectional interface: a feasibility study. *IEEE Transactions on Biomedical Engineering*, *56*(11), 2739–2743. doi:10.1109/TBME.2009.2031242

Clark, F. J., Burgess, R. C., & Chapin, J. W. (1986). Proprioception with the Proximal Interphalangeal Joint of the Index Finger Evidence for a Movement Sense Without a Static-Position Sense. *Brain*, *109*(6), 1195–1208. doi:10.1093/brain/109.6.1195

Da Silva, M. J., Schleicher, E., & Hampel, U. (2007). Capacitance wire-mesh sensor for fast measurement of phase fraction distributions. *Measurement Science and Technology*, *18*, 2245.

Dahiya, R., Metta, G., Valle, M., & Sandini, G. (2010). Tactile Sensing---From Humans to Humanoids. *IEEE Transactions on Robotics*, *PP*(99), 20, 1.

Dang, Z.-M., Jiang, M.-J., Xie, D., Yao, S.-H., Zhang, L.-Q., & Bai, J. (2008). Supersensitive linear piezoresistive property in carbon nanotubes/silicone

rubber nanocomposites. *Journal of Applied Physics*, *104*(2), 024114–024114–6. doi:10.1063/1.2956605

Dargahi, J., & Najarian, S. (2005). Advances in tactile sensors design/manufacturing and its impact on robotics applications – a review. *Industrial Robot: An International Journal*, *32*(3), 268 – 281. doi:10.1108/01439910510593965

De Maria, G., Natale, C., & Pirozzi, S. (2012). Force/tactile Sensor for Robotic Applications. *Sensors and Actuators A: Physical*, *175*, 60–72. doi:10.1016/j.sna.2011.12.042

Dhillon, G. S., & Horch, K. W. (2005). Direct neural sensory feedback and control of a prosthetic arm. *IEEE Transactions on Neural Systems and Rehabilitation Engineering*, *13*(4), 468–472. doi:10.1109/TNSRE.2005.856072

Dodson, M. J., Goodwin, A. W., Browning, A. S., & Gehring, H. M. (1998). Peripheral neural mechanisms determining the orientation of cylinders grasped by the digits. *The Journal of Neuroscience*, *18*(1), 521–530.

Donnelly, D. (2006). The Fast Fourier and Hilbert-Huang Transforms: A Comparison. *International Journal of Computers, Communications & Control*, *1*(4), 45–52.

Driels, M. R. (1986). Pose estimation using tactile sensor data for assembly operations. In *1986 IEEE International Conference on Robotics and Automation. Proceedings* (Vol. 3, pp. 1255–1261). Presented at the 1986 IEEE International Conference on Robotics and Automation. Proceedings. doi:10.1109/ROBOT.1986.1087733

Duffy, B. R., & Joue, G. (2000). Intelligent robots: The question of embodiment. In *Proceedings of Brain-Machine*. Presented at the Brain-Machine, Ankara, Turkey.

Edin, B. B. (1992). Quantitative analysis of static strain sensitivity in human mechanoreceptors from hairy skin. *Journal of Neurophysiology*, *67*(5), 1105–1113.

Engel, J., Chen, J., Fan, Z., & Liu, C. (2005). Polymer micromachined multimodal tactile sensors. *Sensors & Actuators: A. Physical*, *117*(1), 50–61.

Engel, J. M., Chen, N., Ryu, K., Pandya, S., Tucker, C., Yang, Y., & Liu, C. (2006). Multi-layer embedment of conductive and non-conductive PDMS for all-elastomer MEMS. In *Solid State Sensors, Actuators, and Microsystems Workshop (Hilton Head, SC, June 2006* (pp. 316–9).

Essock, E. A., Krebs, W. K., & Prather, J. R. (1997). Superior sensitivity for tactile stimuli oriented proximally-distally on the finger: Implications for mixed class 1 and class 2 anisotropies. *Journal of Experimental Psychology: Human Perception and Performance*, *23*, 515–527.

Fassler, A., & Majidi, C. (2013). Soft-matter capacitors and inductors for hyperelastic strain sensing and stretchable electronics. *Smart Materials and Structures*, *22*(5), 055023. doi:10.1088/0964-1726/22/5/055023

Fearing, R. S., & Binford, T. O. (1991). Using a cylindrical tactile sensor for determining curvature. *IEEE Transactions on Robotics and Automation*, *7*(6), 806–817. doi:10.1109/70.105389

Feng, J.-T., & Zhao, Y.-P. (2007). Influence of different amount of Au on the wetting behavior of PDMS membrane. *Biomedical Microdevices*, *10*, 65–72. doi:10.1007/s10544-007-9110-2

Fishel, J. A., & Loeb, G. E. (2012). Bayesian Exploration for Intelligent Identification of Textures. *Frontiers in Neurorobotics*, *6*, 4. doi:10.3389/fnbot.2012.00004

Fishel, J., Lin, G., & Loeb, G. E. (2013, February 25). SynTouch LLC BioTac Product Manual, v.16.

Fishel, J., & Loeb, G. E. (2012). Sensing Tactile Microvibrations with the BioTac – Comparison with Human Sensitivity. In *Proc of IEEE RAS/EMBS Intl Conf on Biomedical Robotics and Biomechatronics* (pp. 1122–1127). Presented at the IEEE RAS/EMBS Intl Conf on Biomedical Robotics and Biomechatronics, Roma, Italy.

Galinstan MSDS. (2006, September 14). Geratherm Medical AG. Retrieved from http://dsc.dixie.edu/physplant/safety/MSDS/PDF/000266.pdf

Gandevia, S. C., Hall, L. A., McCloskey, D. I., & Potter, E. K. (1983). Proprioceptive sensation at the terminal joint of the middle finger. *The Journal of Physiology*, *335*, 507–517.

Goodwin, A. W., John, K. T., & Marceglia, A. H. (1991). Tactile discrimination of curvature by humans using only cutaneous information from the fingerpads. *Experimental Brain Research*, *86*(3), 663–672. doi:10.1007/BF00230540

Goyal, A., Kumar, A., Patra, P. K., Mahendra, S., Tabatabaei, S., Alvarez, P. J. J., … Ajayan, P. M. (2009). In situ Synthesis of Metal Nanoparticle Embedded Free Standing Multifunctional PDMS Films. *Macromolecular Rapid Communications*, *30*(13), 1116–1122. doi:10.1002/marc.200900174

Gray, B. L., & Fearing, R. S. (1996). A surface micromachined microtactile sensor array. In *Robotics and Automation, 1996. Proceedings., 1996 IEEE International Conference on* (Vol. 1, pp. 1–6).

Hall, M., Frank, E., Holmes, G., Pfahringer, B., Reutemann, P., & Witten, I. H. (2009). The WEKA Data Mining Software: An Update. *ACM SIGKDD Explorations Newsletter*, *11*(1), 10–18.

Hristu, D., Ferrier, N., & Brockett, R. W. (2000). The Performance of a Deformable-Membrane Tactile Sensor: Basic Results on Geometrically-Defined Tasks. In *Proc of IEEE Intl Conf Robotics and Automation* (Vol. 1, pp. 508–513 vol.1). Presented at the IEEE Intl Conf Robotics and Automation, San Francisco, CA. doi:10.1109/ROBOT.2000.844105

Hu, H., Shaikh, K., & Liu, C. (2007a). Super flexible sensor skin using liquid metal as interconnect. *2007 IEEE Sensors*, 815–817.

Hu, H., Shaikh, K., & Liu, C. (2007b). Super flexible sensor skin using liquid metal as interconnect. *2007 IEEE Sensors*, 815–817.

Huang, N. E. (2005). Introduction to the Hilbert-Huang Transform and its Related Mathematical Problems. *Interdisciplinary Mathematics*, *5*, 1–26.

Huang, N. E., Shen, Z., Long, S. R., Wu, M. C., Shih, H. H., Zheng, Q., … Liu, H. H. (1998). The Empirical Mode Decomposition and the Hilbert Spectrum for Nonlinear and Non-Stationary Time Series Analysis. *Proceedings of the Royal Society of London. Series A: Mathematical, Physical and Engineering Sciences*, *454*(1971), 903–995. doi:10.1098/rspa.1998.0193

Huynh, K., Stepp, C. E., White, L. W., Colgate, J. E., & Matsuoka, Y. (2010). Finding a Feature on a 3D Object Through Single-digit Haptic Exploration. In *Haptics Symposium, 2010 IEEE* (pp. 83–89). Retrieved from http://ieeexplore.ieee.org/xpls/abs_all.jsp?arnumber=5444672

Hyung-Kew Lee, Jaehoon Chung, Sun-Il Chang, & Euisik Yoon. (2008). Normal and Shear Force Measurement Using a Flexible Polymer Tactile Sensor With Embedded Multiple Capacitors. *Journal of Microelectromechanical Systems*, *17*(4), 934–942. doi:10.1109/JMEMS.2008.921727

Ittyerah, M., & Marks, L. E. (2008). Intramodal and cross-modal discrimination of curvature: Haptic touch versus vision. *Current psychology letters : behaviour, brain & cognition : CPL*, *24*(1), 1–11.

Jo, B. H., Van Lerberghe, L. M., Motsegood, K. M., & Beebe, D. J. (2000). Three-dimensional micro-channel fabrication in polydimethylsiloxane (PDMS) elastomer. *Microelectromechanical Systems, Journal of*, *9*(1),

76–81.

Johansson, R. S., & Flanagan, J. R. (2008). Tactile sensory control of object manipulation in humans. In J. H. Kaas & E. Gardner (Eds.), *Handbook of the Senses* (Vol. 6: Somatosensation, pp. 67–86). San Diego: Academic Press. Retrieved from http://umu.diva-portal.org/smash/record.jsf?searchId=1&pid=diva2:208419

Johansson, R. S., & Flanagan, J. R. (2009). Coding and Use of Tactile Signals from the Fingertips in Object Manipulation Tasks. *Nature Reviews Neuroscience*.

Johansson, R. S., Landstrom, U., & Lundstrom, R. (1982). Sensitivity to edges of mechanoreceptive afferent units innervating the glabrous skin of the human hand. *Brain Research*, *244*, 27–32. doi:10.1016/0006-8993(82)90900-3

Johansson, R. S., & Vallbo, A. B. (1983). Tactile sensory coding in the glabrous skin of the human hand. *Trends in NeuroSciences*, *6*, 27–32.

Johnsson, M., & Balkenius, C. (2007). Neural network models of haptic shape perception. *Robotics and Autonomous Systems*, *55*(9), 720–727. doi:10.1016/j.robot.2007.05.003

Jones, L. A., & Lederman, S. J. (2006). *Human hand function*. Oxford University Press.

Jung, W. G. (2005). *Op Amp applications handbook*. Newnes.

Khalsa, P. S., Friedman, R. M., Srinivasan, M. A., & LaMotte, R. H. (1998). Encoding of shape and orientation of objects indented into the monkey fingerpad by populations of slowly and rapidly adapting mechanoreceptors. *Journal of neurophysiology*, *79*(6), 3238–3251.

Khanafer, K., Duprey, A., Schlicht, M., & Berguer, R. (2008). Effects of strain rate, mixing ratio, and stress–strain definition on the mechanical behavior of the polydimethylsiloxane (PDMS) material as related to its biological applications. *Biomedical Microdevices*, *11*(2), 503–508. doi:10.1007/s10544-008-9256-6

Kim, D. H., Song, J., Choi, W. M., Kim, H. S., Kim, R. H., Liu, Z., … Rogers, J. A. (2008). Materials and noncoplanar mesh designs for integrated circuits with linear elastic responses to extreme mechanical deformations. *Proceedings of the National Academy of Sciences*, *105*(48), 18675.

Kim, H.-J., Son, C., & Ziaie, B. (2008). A multiaxial stretchable interconnect using liquid-alloy-filled elastomeric microchannels. *Applied Physics*

Letters, *92*(1), 011904. doi:10.1063/1.2829595

Kim, K. H., & Seo, Y. H. (2008). Proofmass-less vibration sensor using the motion of self-charged anion and cation in an electrolyte for ultra-high frequency detection. In *Micro Electro Mechanical Systems, 2008. MEMS 2008. IEEE 21st International Conference on* (pp. 94–97).

Klatzky, R. L., & Lederman, S. J. (1999). The haptic glance: A route to rapid object identification and manipulation. In D. Gopher & A. Koriats (Eds.), *Attention and Performance XVII: Cognitive Regulation of Performance: Interaction of Theory and Application*.

Klatzky, Roberta L., & Lederman, S. J. (1992). Stages of manual exploration in haptic object identification. *Perception & Psychophysics*, *52*(6), 661–670. doi:10.3758/BF03211702

Klatzky, Roberta L., Lederman, S. J., & Reed, C. (1987). There's more to touch than meets the eye: The salience of object attributes for haptics with and without vision. *Journal of Experimental Psychology: General*, *116*(4), 356–369. doi:10.1037/0096-3445.116.4.356

Koch, H., Konig, A., Weigl-Seitz, A., Kleinmann, K., & Suchy, J. (2013). Multisensor Contour Following With Vision, Force, and Acceleration Sensors for an Industrial Robot. *IEEE Transactions on Instrumentation and Measurement*, *62*(2), 268–280. doi:10.1109/TIM.2012.2214934

Koterba, S., & Matsuoka, Y. (2006). A triaxial force discernment algorithm for flexible, high density, artificial skin. In *Robotics and Automation, 2006. ICRA 2006. Proceedings 2006 IEEE International Conference on* (pp. 1359–1364).

Kramer, R. K., Majidi, C., Sahai, R., & Wood, R. J. (2011). Soft Curvature Sensors for Joint Angle Proprioception. In *Proc IEEE/RSJ Intl Conf Intelligent Rob Sys* (pp. 1919–1926). San Francisco, CA.

Lackner, J. R., Rabin, E., & DiZio, P. (2001). Stabilization of posture by precision touch of the index finger with rigid and flexible filaments. *Experimental Brain Research*, *139*(4), 454–464. doi:10.1007/s002210100775

LaMotte, R. H., Friedman, R. M., Lu, C., Khalsa, P. S., & Srinivasan, M. A. (1998). Raised object on a planar surface stroked across the fingerpad: Responses of cutaneous mechanoreceptors to shape and orientation. *Journal of Neurophysiology*, *80*(5), 2446–2466.

LaMotte, R. H., & Srinivasan, M. A. (1987). Tactile discrimination of shape: responses of slowly adapting mechanoreceptor afferents to a step stroked across the monkey fingerpad. *Journal of Neuroscience*, *7*(6), 1655–1671.

LaMotte, Robert H., & Srinivasan, M. A. (1987). Tactile discrimination of shape: responses of rapidly adapting mechanoreceptive afferents to a step stroked across the monkey fingerpad. *Journal of Neuroscience*, *7*(6), 1672–1681.

LaMotte, Robert H., & Srinivasan, M. A. (1993). Responses of cutaneous mechanoreceptors to the shape of objects applied to the primate fingerpad. *Acta Psychologica*, *84*(1), 41–51. doi:10.1016/0001-6918(93)90071-X

Lechelt, E. C. (1988). Spatial asymmetries in tactile discrimination of line orientation: a comparison of the sighted, visually impaired, and blind. *Perception*, *17*(5), 579 – 585. doi:10.1068/p170579

Lechelt, E. C. (1992). Tactile spatial anisotropy with static stimulation. *Bulletin of the Psychonomic Society*, *30*(2), 140–142.

Lederman, S. J., & Klatzky, R. L. (1987). Hand Movements: A Window Into Haptic Object Recognition. *Cognitive Psychology*, *19*(3), 342–368.

Lederman, S. J., & Klatzky, R. L. (1997). Relative Availability of Surface and Object Properties During Early Haptic Processing. *Journal of experimental psychology. Human perception and performance*, *23*(6), 1680–1707.

Lee, H.-K., Chang, S.-I., & Yoon, E. (2006). A Flexible Polymer Tactile Sensor: Fabrication and Modular Expandability for Large Area Deployment. *Journal of Microelectromechanical Systems*, *15*(6), 1681–1686. doi:10.1109/JMEMS.2006.886021

Lee, M. H., & Nicholls, H. R. (1999). Tactile sensing for mechatronics—a state of the art survey. *Mechatronics*, *9*(1), 1–31.

Lei, K. F., Lee, K.-F., & Lee, M.-Y. (2012). Development of a flexible PDMS capacitive pressure sensor for plantar pressure measurement. *Microelectronic Engineering*, *99*, 1–5. doi:10.1016/j.mee.2012.06.005

Lin, C. H., Erickson, T. W., Fishel, J. A., Wettels, N., & Loeb, G. E. (2009). Signal Processing and Fabrication of a Biomimetic Tactile Sensor Array with Thermal, Force and Microvibration Modalities. In *Proc of IEEE Intl Conf on Robotics and Biomimetics* (pp. 129–134). Presented at the Proc of IEEE Intl Conf on Robotics and Biomimetics, Guilin, China. doi:10.1109/ROBIO.2009.5420611

Liu, C. (2007). Recent Developments in Polymer MEMS. *Advanced Materials*, *19*(22), 3783–3790. doi:10.1002/adma.200701709

Liu, H., Song, X., Bimbo, J., Seneviratne, L., & Althoefer, K. (2012). Surface material recognition through haptic exploration using an intelligent contact

sensing finger. In *2012 IEEE/RSJ International Conference on Intelligent Robots and Systems (IROS)* (pp. 52–57). Presented at the 2012 IEEE/RSJ International Conference on Intelligent Robots and Systems (IROS). doi:10.1109/IROS.2012.6385815

Liu, W., Yan, Y., & Wang, R. (2011). Application of Hilbert-Huang Transform and SVM to Coal Gangue Interface Detection. *Journal of Computers*, *6*(6). doi:10.4304/jcp.6.6.1262-1269

London, B. M., Jordan, L. R., Jackson, C. R., & Miller, L. E. (2008). Electrical Stimulation of the Proprioceptive Cortex (Area 3a) Used to Instruct a Behaving Monkey. *IEEE Transactions on Neural Systems and Rehabilitation Engineering*, *16*(1), 32–36. doi:10.1109/TNSRE.2007.907544

Lotters, J. C., Olthuis, W., Veltink, P. H., & Bergveld, P. (1997). The mechanical properties of the rubber elastic polymer polydimethylsiloxane for sensor applications. *Journal of Micromechanics and Microengineering*, *7*, 145.

Louw, S., Kappers, A. M., & Koenderink, J. J. (2002). Haptic discrimination of stimuli varying in amplitude and width. *Experimental brain research*, *146*(1), 32–37.

Ma, R. R., Odhner, L. U., & Dollar, A. M. (2013). A Modular, Open-Source 3D Printed Underactuated Hand. In *International Conf on Robotics and Automation*. Presented at the International Conf on Robotics and Automation. Retrieved from http://www.eng.yale.edu/grablab/pubs/Ma_ICRA2013.pdf

Maheshwari, V., & Ravi Saraf. (2008). Tactile Devices To Sense Touch on a Par with a Human Finger. *Angewandte Chemie International Edition*, *47*(41), 7808–7826. doi:10.1002/anie.200703693

Majidi, C., Kramer, R., & Wood, R. (2011). A non-differential elastomer curvature sensor for softer-than-skin electronics. *Smart Materials and Structures*, *20*, 105017.

Mark, J. E. (2007). *Physical properties of polymers handbook*. Springer.

Martinez-Hernandez, U., Dodd, T. J., Natale, L., Metta, G., Prescott, T. J., & Lepora, N. F. (2013). Active contour following to explore object shape with robot touch. Retrieved from http://www.lepora.com/publications/martinez_etal2013whc.pdf

Massa, B., Roccella, S., Carrozza, M. C., & Dario, P. (2002). Design and Development of an Underactuated Prosthetic Hand. In *IEEE International Conference on Robotics and Automation, 2002. Proceedings. ICRA '02*

(Vol. 4, pp. 3374–3379 vol.4). Presented at the IEEE International Conference on Robotics and Automation, 2002. Proceedings. ICRA '02. doi:10.1109/ROBOT.2002.1014232

McMahon, I., Chu, V., Riano, L., McDonald, C. G., He, Q., Perez-Tejada, J. M., … Kuchenbecker, K. J. (2012). Robotic Learning of Haptic Adjectives Through Physical Interaction. In *IROS workshop on Advances in Tactile Sensing and Touch based Human-Robot Interaction*. Presented at the IEEE/RSJ Intl Conf on Intelligent Robots and Systems. Retrieved from http://www.eecs.berkeley.edu/~riano/files/IROSWSAdjectives.pdf

Mei, T., Li, W. J., Ge, Y., Chen, Y., Ni, L., & Chan, M. H. (2000). An Integrated MEMS Three-Dimensional Tactile Sensor with Large Force Range. *Sensors & Actuators: A. Physical*, *80*(2), 155–162.

Micolich, A. P., Bell, L. L., & Hamilton, A. R. (2007). An improved process for fabricating high-mobility organic molecular crystal field-effect transistors. *Journal of Applied Physics*, *102*, 084511. doi:10.1063/1.2802284

Millar, S. (1994). *Understanding and Representing Space: Theory and Evidence from Studies With Blind and Sighted Children*. Oxford University Press.

Miller, A. T., & Allen, P. K. (2004). Graspit! A Versatile Simulator for Robotic Grasping. *Robotics & Automation Magazine, IEEE*, *11*(4), 110–122. doi:10.1109/MRA.2004.1371616

Mittendorfer, P., & Cheng, G. (2011). Humanoid Multimodal Tactile-Sensing Modules. *IEEE Transactions on Robotics*, *27*(3), 401 –410. doi:10.1109/TRO.2011.2106330

Muhammad, H. B., Recchiuto, C., Oddo, C. M., Beccai, L., Anthony, C. J., Adams, M. J., … Ward, M. C. L. (2011). A capacitive tactile sensor array for surface texture discrimination. *Microelectronic Engineering*, *88*(8), 1811–1813. doi:16/j.mee.2011.01.045

Mukai, T., Onishi, M., Odashima, T., Hirano, S., & Zhiwei Luo. (2008). Development of the Tactile Sensor System of a Human-Interactive Robot “RI-MAN” *IEEE Transactions on Robotics*, *24*(2), 505–512. doi:10.1109/TRO.2008.917006

Nakamoto, H., Kobayashi, F., & Kojima, F. (2010). Shape classification using tactile information in rotation manipulation by universal robot hand. *Robotics 2010 Current and Future Challenges*, 123–132.

Nawaz, A. A., Mao, X., Stratton, Z. S., & Huang, T. J. (2013). Unconventional microfluidics: expanding the discipline. *Lab on a Chip*. doi:10.1039/c3lc90023a

O'Doherty, J. E., Lebedev, M. A., Ifft, P. J., Zhuang, K. Z., Shokur, S., Bleuler, H., & Nicolelis, M. A. L. (2011). Active tactile exploration using a brain-machine-brain interface. *Nature, advance online publication*. doi:10.1038/nature10489

Okamura, A. M., & Cutkosky, M. R. (2001). Feature detection for haptic exploration with robotic fingers. *The International Journal of Robotics Research*, *20*(12), 925–938.

Overstreet, C., Klein, J. D., & Helms Tillery, S. (2013). Excitation of distinct pools of somatosensory neurons via intracortical microstimulation. In *Proc Soc for Neuroscience*. Presented at the Soc for Neuroscience, New Orleans, LA.

Overvliet, K. E., Smeets, J. B. J., & Brenner, E. (2008). The use of proprioception and tactile information in haptic search. *Acta Psychologica*, *129*(1), 83–90. doi:10.1016/j.actpsy.2008.04.011

Pape, L., Oddo, C. M., Controzzi, M., Förster, A., & Schmidhuber, J. (2012). Learning tactile skills through curious exploration. *Frontiers in Neurorobotics*, *6*, 6. doi:10.3389/fnbot.2012.00006

Park, Y. L., Chen, B., & Wood, R. J. (2011). Soft Artificial Skin with Multi-Modal Sensing Capability Using Embedded Liquid Conductors. Presented at the IEEE Sensors Conf, Limerick, Ireland.

Park, Y. L., Majidi, C., Kramer, R., Bérard, P., & Wood, R. J. (2010). Hyperelastic pressure sensing with a liquid-embedded elastomer. *Journal of Micromechanics and Microengineering*, *20*, 125029.

Park, Y.-L., Chen, B.-R., & Wood, R. J. (2012). Design and Fabrication of Soft Artificial Skin Using Embedded Microchannels and Liquid Conductors. *IEEE Sensors Journal*, *12*(8), 2711 –2718. doi:10.1109/JSEN.2012.2200790

Penfield, W., & Rasmussen, T. (1950). *The cerebral cortex of man: a clinical study of localization of function*. Macmillan.

Peng Peng, Rajamani, R., & Erdman, A. G. (2009). Flexible Tactile Sensor for Tissue Elasticity Measurements. *Journal of Microelectromechanical Systems*, *18*(6), 1226–1233. doi:10.1109/JMEMS.2009.2034391

Petriu, E. M., McMath, W. S., Yeung, S. S. K., & Trif, N. (1992). Active Tactile Perception of Object Surface Geometric Profiles. *IEEE Transactions on Instrumentation and Measurement*, *41*(1), 87 –92. doi:10.1109/19.126638

Phillips, J. R., & Johnson, K. O. (1981). Tactile spatial resolution. II. Neural

representation of bars, edges, and gratings in monkey primary afferents. *J Neurophysiol*, *46*(6), 1192–1203.

Plaisier, M. A., Bergmann Tiest, W. M., & Kappers, A. M. L. (2009). Salient Features in 3-D Haptic Shape Perception. *Attention, Perception, & Psychophysics*, *71*(2), 421–430.

Ponce Wong, R. D., Posner, J. D., & Santos, V. J. (2012). Flexible Microfluidic Normal Force Sensor Skin for Tactile Feedback. *Sensors and Actuators A: Physical*, *179*(0), 62–69. doi:10.1016/j.sna.2012.03.023

Pont, S. C., Kappers, A. M., & Koenderink, J. J. (1999). Similar mechanisms underlie curvature comparison by static and dynamic touch. *Perception & Psychophysics*, *61*(5), 874–894.

Prattichizzo, D., & Trinkle, J. C. (2008). Grasping. In B. Siciliano & O. Khatib (Eds.), *Springer Handbook of Robotics* (pp. 671–700). Berlin Heidelberg: Springer-Verlag. Retrieved from http://dx.doi.org/10.1007/978-3-540-30301-5_29

Riley, M. A., & Turvey, M. T. (2002). Variability and Determinism in Motor Behavior. *Journal of Motor Behavior*, *34*(2), 99–125.

Romo, R., Hernández, A., Zainos, A., & Salinas, E. (1998). Somatosensory discrimination based on cortical microstimulation. *Nature*, *392*(6674), 387–390. doi:10.1038/32891

Santos, V. J., Posner, J. D., & Ponce Wong, R. D. (2013). Systems for providing electro-mechanical sensors.

Schneider, F., Fellner, T., Wilde, J., & Wallrabe, U. (2008). Mechanical properties of silicones for MEMS. *Journal of Micromechanics and Microengineering*, *18*(6), 065008. doi:10.1088/0960-1317/18/6/065008

Schultz, A. E., Marasco, P. D., & Kuiken, T. A. (2009). Vibrotactile detection thresholds for chest skin of amputees following targeted reinnervation surgery. *Brain Research*, *1251*, 121–129. doi:10.1016/j.brainres.2008.11.039

Schulze, D., Karcher, C., Kocourek, V., & Mohring, J. U. (2006). Electrically Induced Instabilities of Liquid Metal Free Surfaces. In *Modelling for Material Processing* (Vol. 66, pp. 2501–2511). Riga.

Sergio, M., Manaresi, N., Tartagni, M., Canegallo, R., & Guerrieri, R. (2002). A textile-based capacitive pressure sensor. In *Sensor Letters*.

Shifeng Li, & Shaochen Chen. (2003). Polydimethylsioxane fluidic interconnects

for microfluidic systems. *IEEE Transactions on Advanced Packaging*, *26*(3), 242–247. doi:10.1109/TADVP.2003.817961

Siegel, D. M. (1991). *Pose Determination of a Grasped Object Using Limited Sensing* (No. AITR-1300). Retrieved from http://dspace.mit.edu/handle/1721.1/7292

Siegel, M. (2003). The Sense-Think-Act Paradigm Revisited. In *Robotic Sensing, 2003. ROSE' 03. 1st International Workshop on* (p. 5 pp.). Presented at the Robotic Sensing, 2003. ROSE' 03. 1st International Workshop on.

Srinivasan, M. A., & Dandekar, K. (1992). Role of fingertip geometry in the transmission of tactile mechanical signals. In M. W. Bidez (Ed.), *Advances in Bioengineering* (Vol. 22, pp. 573–576). American Society of Mechanical Engineers.

Srinivasan, M. A., & Dandekar, K. (1996). An investigation of the mechanics of tactile sense using two-dimensional models of the primate fingertip. *ASME Journal of Biomechanical Engineering*, *118*, 48–55.

Srinivasan, M. A., & LaMotte, R. H. (1991). Encoding of shape in the responses of cutaneous mechanoreceptors. In O. Franzen & J. Westman (Eds.), (Information Processing in the Somatosensory System, Wenner-Gren Intl. Symposium Series.). Macmillan Press.

Srinivasan, Mandayam A., & LaMotte, R. H. (1987). Tactile discrimination of shape: responses of slowly and rapidly adapting mechanoreceptive afferents to a step indented into the monkey fingerpad. *Journal of Neuroscience*, *7*(6), 1682–1697.

Stamper, S. A., Roth, E., Cowan, N. J., & Fortune, E. S. (2012). Active sensing via movement shapes spatiotemporal patterns of sensory feedback. *Journal of Experimental Biology*, *215*(9), 1567–1574. doi:10.1242/jeb.068007

Sternad, D., & Abe, M. O. (2010). Variability, Noise, and Sensitivity to Error in Learning a Motor Task. In F. Danion & M. Latash (Eds.), *Motor Control: Theories, Experiments, and Applications*.

Su, Z., Fishel, J. A., Yamamoto, T., & Loeb, G. E. (2012). Use of Tactile Feedback to Control Exploratory Movements to Characterize Object Compliance. *Frontiers in Neurorobotics*, *6*. doi:10.3389/fnbot.2012.00007

Su, Z., Li, Y., & Loeb, G. E. (2011). Estimation of Curvature Feature Using a Biomimetic Tactile Sensor. Retrieved from http://www.asbweb.org/conferences/2011/pdf/386.pdf

Surmann, P., & Zeyat, H. (2005). Voltammetric analysis using a self-renewable non-mercury electrode. *Analytical and Bioanalytical Chemistry, 383*(6), 1009–1013. doi:10.1007/s00216-005-0069-7

Takamuku, S., Gomez, G., Hosoda, K., & Pfeifer, R. (2007). Haptic discrimination of material properties by a robotic hand. In *IEEE 6th International Conference on Development and Learning, 2007. ICDL 2007* (pp. 1 –6). Presented at the IEEE 6th International Conference on Development and Learning, 2007. ICDL 2007. doi:10.1109/DEVLRN.2007.4354057

Tan, P.-N., Steinbach, M., & Kumar, V. (2006). *Introduction to Data Mining*. Pearson Addison Wesley.

Tatsuta Film. (n.d.). *Electromagnetic Noise Shielding Film for FPC Applications*. Osaka, Japan. Retrieved from http://film.tatsuta.com/eng/pdfs/sf_pc1000_catalog_en.pdf

Tegin, J., & Wikander, J. (2005). Tactile sensing in intelligent robotic manipulation – a review. *Industrial Robot: An International Journal*, *32*(1), 64–70. doi:10.1108/01439910510573318

Tiwana, M. I., Redmond, S. J., & Lovell, N. H. (2012). A review of tactile sensing technologies with applications in biomedical engineering. *Sensors and Actuators A: Physical*, *179*, 17–31. doi:10.1016/j.sna.2012.02.051

Tseng, W. Y., Fisher, J. S., Prieto, J. L., Rinaldi, K., Alapati, G., & Lee, A. P. (2009). A slow-adapting microfluidic-based tactile sensor. *Journal of Micromechanics and Microengineering*, *19*, 085002.

Ventrelli, L., Beccai, L., Mattoli, V., Menciassi, A., & Dario, P. (2009). Development of a stretchable skin-like tactile sensor based on polymeric composites. In *2009 IEEE International Conference on Robotics and Biomimetics (ROBIO)* (pp. 123–128). Presented at the 2009 IEEE International Conference on Robotics and Biomimetics (ROBIO), IEEE. doi:10.1109/ROBIO.2009.5420644

Wettels, N., & Loeb, G. E. (2011). Haptic feature extraction from a biomimetic tactile sensor: Force, contact location and curvature. In *2011 IEEE International Conference on Robotics and Biomimetics (ROBIO)* (pp. 2471 –2478). Presented at the 2011 IEEE International Conference on Robotics and Biomimetics (ROBIO), Phuket, Thailand. doi:10.1109/ROBIO.2011.6181676

Wettels, N., Smith, L. M., Santos, V. J., & Loeb, G. E. (2008). Deformable Skin Design to Enhance Response of a Biomimetic Tactile Sensor. In *Biomedical Robotics and Biomechatronics, 2008. BioRob 2008. 2nd IEEE*

RAS & EMBS International Conference on (pp. 132–137). Presented at the Biomedical Robotics and Biomechatronics, 2008. BioRob 2008. 2nd IEEE RAS & EMBS International Conference on. doi:10.1109/BIOROB.2008.4762914

Wettels, Nicholas, Santos, V. J., Johansson, R. S., & Loeb, G. E. (2008). Biomimetic Tactile Sensor Array. *Advanced Robotics*, *22*, 829–849. doi:10.1163/156855308X314533

Xu, D., Loeb, G. E., & Fishel, J. A. (2013). Tactile identification of objects using Bayesian exploration. In *Proc IEEE Intl Conf on Robotics and Automation*. Presented at the IEEE Intl Conf on Robotics and Automation, Karlsruhe, Germany. Retrieved from http://www.tactilesensor.com/Technology/_publications/2013_Xu_ICRA.pdf

Yousef, H., Boukallel, M., & Althoefer, K. (2011). Tactile sensing for dexterous in-hand manipulation in robotics–A review. *Sensors and Actuators A: Physical*.

Zhang, G. P., & Wang, Z. G. (2008). Fatigue of Small-Scale Metal Materials: From Micro-to Nano-Scale. *Multiscale Fatigue Crack Initiation and Propagation of Engineering Materials: Structural Integrity and Microstructural Worthiness*, 275–326.

Zuidhoek, S., Dokmeci, M. R., Annabiab, N., & Khademhosseini, A. (2012). Research Highlights. *Lab on a Chip*. Retrieved from http://pubs.rsc.org/en/content/articlepdf/2013/lc/c2lc90139k

APPENDIX A

SUPPLEMENTAL MATERIAL FOR CHAPTER 3

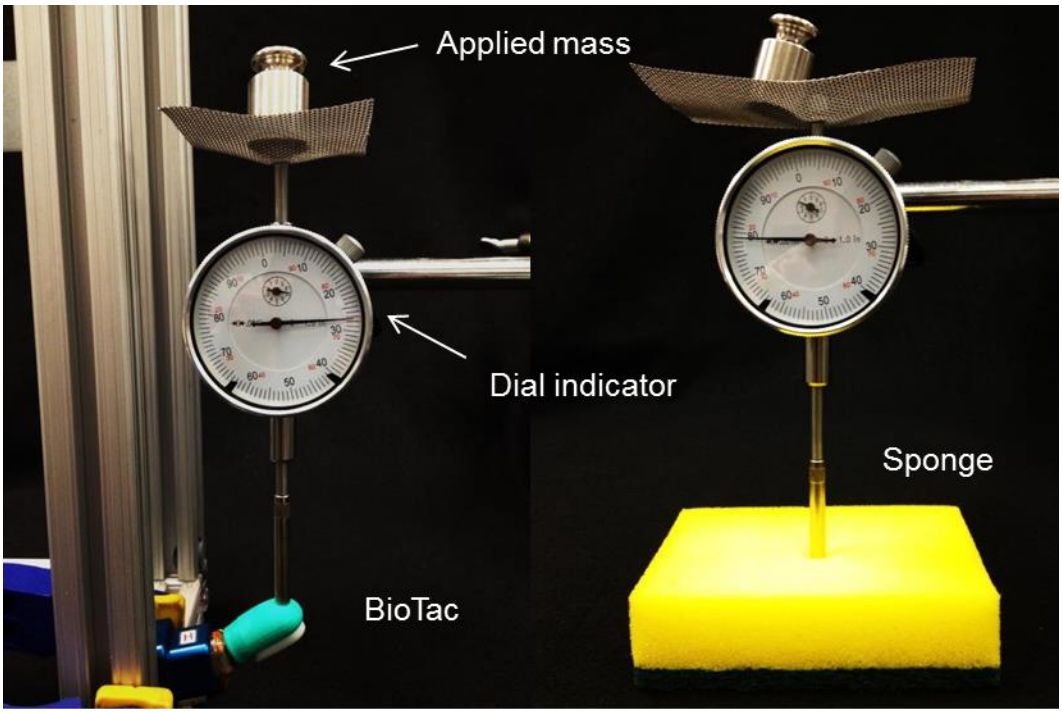

Figure A.1. Custom durometer setup for measuring stiffness of compliant stimuli. The dial indicator's measurement at the surface of the object is measured. Mass is added to the top of the indicator. The indentation in the compliant object is allowed to stabilize. The setups for a) a BioTac oriented at 30° with respect to the flat tip of the indicator and b) a sponge are depicted.

APPENDIX B

SUPPLEMENTAL MATERIAL FOR CHAPTER 4

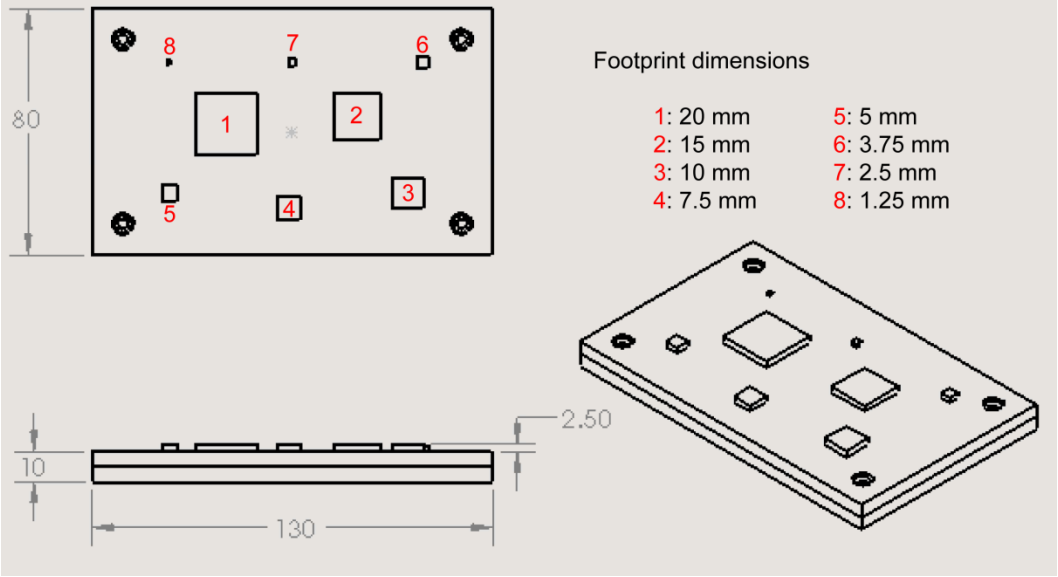

Figure B.1. SolidWorks schematics of tactile stimuli for characterization of finger-sized geometric feature. Different views of the planar bumps are shown. The footprint dimensions are given for the labeled features in red (numbered in descending size). All dimensions are given in mm.

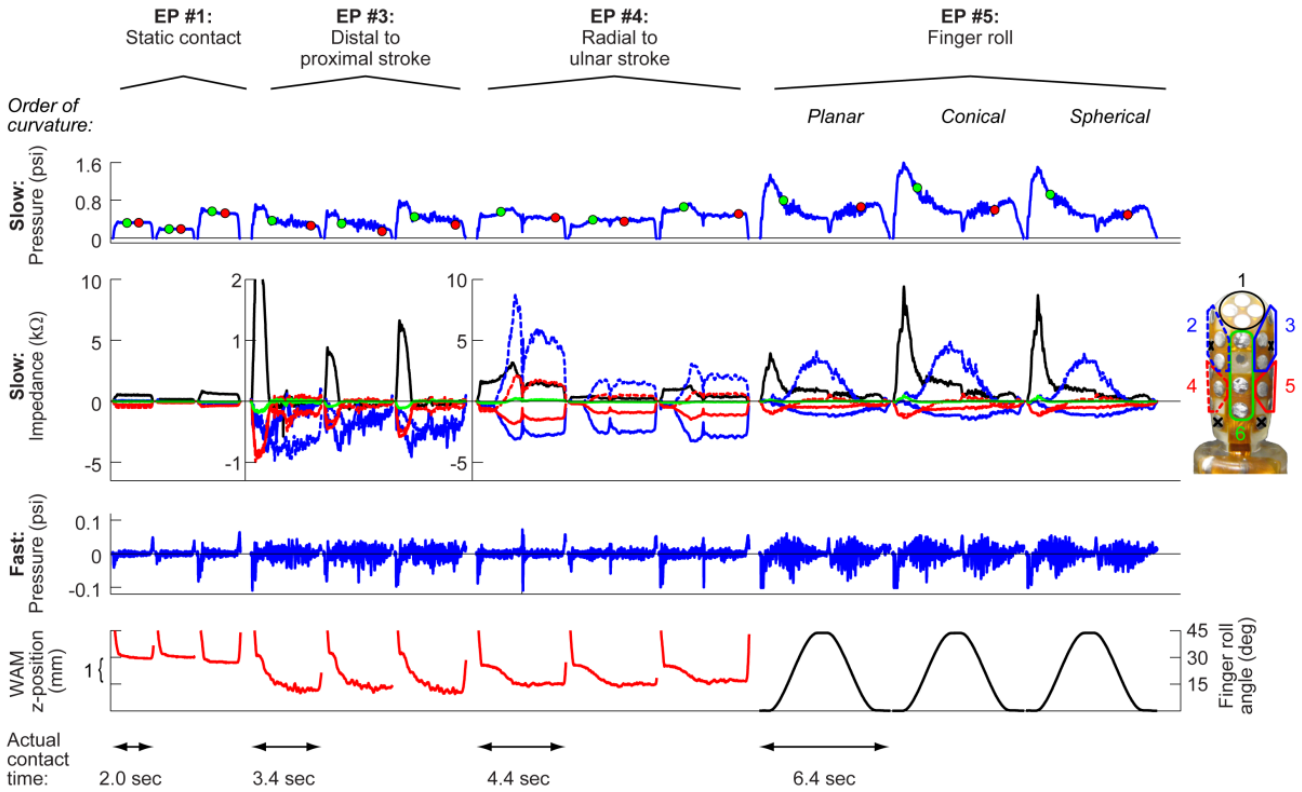

Figure B.2. Representative multimodal tactile data for a planar, conical, and spherical 7.5 mm pits. Overall fluid pressure (row 1) was used to determine initial contact and loss of contact with the test plate. Only periods of contact with the geometric features (between the green and red dots in row 1) were used to extract model input parameters.

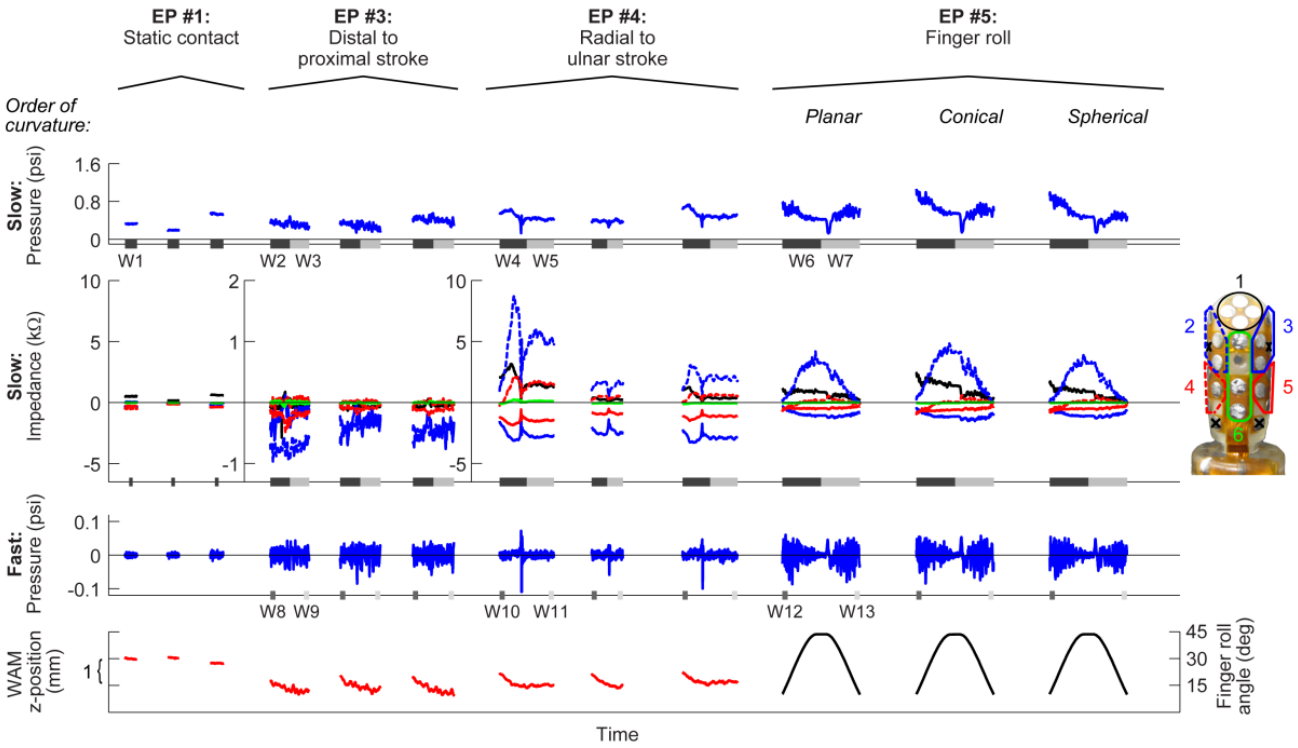

Figure B.3. Truncated multimodal tactile data for a planar, conical, and spherical 7.5 mm pits. Tactile signals were truncated (from *Figure B.2*) such that only periods of contact with geometric features were used for modeling. Inputs to the SVC and SVR models were calculated from windows of time (W1-W13) that were specific to each exploratory procedure.

C++ code to control the Barrett WAM for haptic exploration of finger-sized geometric features

```
/*
 * Based on file “can_terminal.cpp”
 *  Created on: Aug 19, 2010
 *      Author: dc
 *
 *  Modified on: June 9, 2013
 *      Modified originally by R. Hellman,
 *      Later modified by R. Ponce Wong and R. Hellman
 *
 */

#include <iostream>
#include <fstream>
#include <stdio.h>
#include <vector>
#include <string>
#include <cstdio>
#include <math.h>
#include <cstdlib>  // For mkstmp()

#include <boost/ref.hpp>
#include <boost/bind.hpp>
#include <boost/tuple/tuple.hpp>
#include <unistd.h>
#include <barrett/os.h>  // For btsleep()
#include <boost/thread.hpp>
#include <barrett/bus/can_socket.h>

#include <barrett/detail/stl_utils.h>  // waitForEnter()
#include <barrett/math.h>
#include <barrett/units.h>
#include <barrett/systems.h>
#include <barrett/log.h>
#include <barrett/products/product_manager.h>
#include <barrett/standard_main_function.h>

//Data logging
 #define BARRETT_SMF_VALIDATE_ARGS

//EPOS REQUIRED
#include "EPOSInterface.h"

//HAND REQUIRED
#include "btserial.h"

//BIOTAC REQUIRED
#include "cheetah.h"
#include "biotac.h"

using namespace barrett;
using detail::waitForEnter;
using systems::connect;
using systems::disconnect;
using systems::reconnect;

int MovementState = 0;
bool BTrecord = false;
char BTfilename[120];
char BHfilename[120];
char WAMfilename[120];
int BTn=0;
int rec_duration;

std::vector<int> DateVec;
std::vector<int> BTdegVec;
```

```
std::vector<int> VelVec;
std::vector<double> PushVec;
std::vector<std::string> TypeVec;
std::vector<double> OverallDimensionVec;
std::vector<std::string> HeightVec;
std::vector<int> TrialVec;



////////////////////////////////////////////////////////////////////////////////
////
//  FUNCTION:  Thread to Collect BioTac Data
                                //
////////////////////////////////////////////////////////////////////////////////
////
void BioTacThread(const bool* going)
{
        int err = 0;
        printf("Checking the BTHand & BTData dir exist if not will create\n");
        err = system("mkdir -p S_feat_BTData");
        err = system("mkdir -p S_feat_BTHand");
        err = system("mkdir -p S_feat_BTWAMdata");
        while(*going)
        {
                btsleep(0.1);
                if(BTrecord)
                {
                        printf("\n\nAbout to record\n\n");
                        system(BTfilename);
                        BTrecord = false;
                        printf("\n\nCall made\n\n");
                }
        }
        return;
}



////////////////////////////////////////////////////////////////////////////////
////
//  FUNCTION:  Thread to Communicate with EPOS Controller (Switch for Load Cell)
        //
////////////////////////////////////////////////////////////////////////////////
////
void readThread(const bus::CANSocket* bus, const bool* going) {
        int ret;
        int id;
        unsigned char data[bus::CANSocket::MAX_MESSAGE_LEN];
        size_t len;

        while (*going) {
                ret  = bus->receiveRaw(id, data, len, false);
                if (ret == 0) {  // success
                        //CHECKS for MovementState
                        if(id == 0x581 && data[0] == 0x4b && data[1] == 0x41 &&
data[2] == 0x60)
                        {
                                if(data[5] == 0x11){
                                        MovementState = 2;
                                }
                                else{
                                        MovementState = 0;
                                }
                        }
                } else if (ret != 1) {  // error other than no data
                        printf("ERROR: bus::CANSocket::receive() returned %d.\n",
ret);
```

```
                }
                usleep(1000);
        }
        return;
}



////////////////////////////////////////////////////////////////////////////////
////
//  FUNCTION:  Thread to Collect BarrettHand Strain Gage Data
                        //
////////////////////////////////////////////////////////////////////////////////
////
void BarrettHandSGThread(const bool* going) {
   PORT p;
   FILE *fp;

   bool fileOpen = false;
   char input[255];
   int err, len, SG3;
   if(err = serialOpen(&p, "/dev/ttyS0")) {
      printf("Error opening port: %d\n", err);
      return;
   }
   serialSetBaud(&p,9600);
   printf("BaudSet \n");
   btsleep(1);

   while(*going) {
                while(BTrecord)
                {
                        if(!fileOpen){
                                fp = fopen(BHfilename, "w");
                                if (!fp)
                                {
                                        printf("Error: Cannot open output file.\n");
                                }
                                else
                                fileOpen = true;
                        }
                /* Read chars from the port into the input buffer until
                the termination character '>' is received or 30 seconds has
                elapsed, whichever comes first. */
                serialWriteString(&p, "3FGET SG\r");
                serialReadLine(&p, input, &len, '>', 300000);
                SG3 = atoi(strtok(input+10, "="));
                fprintf(fp,"%4.0d\n",SG3);
        }
        if(fileOpen)
        {
                fclose(fp);
                fileOpen = false;
        }

        btsleep(0.1);

   }
   serialClose(&p);
   return;
}



////////////////////////////////////////////////////////////////////////////////
////
```

```
//  FUNCTION:  Function to specify which small feature to explore (i.e. to define
//
//                        which trajectory to load)
                                                    //
////////////////////////////////////////////////////////////////////////////////
////
void Small_Feature_to_Explore() {

        using namespace std;

        // Defining temporary string variables
        string temp_date;
        string temp_BTdeg;
        string temp_vel;
        string temp_push;
        string temp_type;
        string temp_dim;
        string temp_height;
        string temp_trial;

        // Defining variables to hold data for vector variables
        int date(0);
        int BTdeg(0);
        int vel(0);
        double push(0);
        double dim(0);
        int trial(0);

        // Defininng and opening the input data file
        ifstream myfile ("FileInfo_S_feat.txt");
        if (myfile.is_open())
        {
                while ( myfile.good() )
                {
                        // Assigning values of each column of the data file to the
temp variables
                        myfile >> temp_date >> temp_BTdeg >> temp_vel >> temp_push
>>
                                        temp_type >> temp_dim >> temp_height >>
temp_trial;

                        // Converting from string variable to int or floating
variables
                date  = atoi( temp_date.c_str());
                BTdeg = atoi(temp_BTdeg.c_str());
                vel   = atoi(  temp_vel.c_str());
                push  = atof( temp_push.c_str());
                dim   = atof(  temp_dim.c_str());
                        trial = atoi(temp_trial.c_str());

                        // Storing the values into vectors
                DateVec.push_back(date);
                BTdegVec.push_back(BTdeg);
                VelVec.push_back(vel);
                PushVec.push_back(push);
                        TypeVec.push_back(temp_type);
                OverallDimensionVec.push_back(dim);
                        HeightVec.push_back(temp_height);
                TrialVec.push_back(trial);
                }
                myfile.close();
  }
  else cout << "Unable to open file";
}
```

```
////////////////////////////////////////////////////////////////////////////////
////
//  MAIN FUNCTION:  Runs the experiment
                                                //
//             1) Load the data file containing the randomized exploration order
of features/
//             2) Move WAM to starting point (trajectory: 'firstmove_S_feat')
                    //
//             3) Defining the trajectory movements of the different small
features                //
//             4) Loop that runs with the specified number of iterations
                    //
//                          a. Defining the output file names
                                        //
//                          b. Turn on BioTac data collection
                                        //
//                          c. Perform exploratory movement based on listed
feature's dimension //
//                          d. Repeat until all rows of data file has been read
                            //
//             5) Finishing the experiment and closing evertyhing
                            //
////////////////////////////////////////////////////////////////////////////////
////
template<size_t DOF>
int wam_main(int argc, char** argv, ProductManager& pm, systems::Wam<DOF>& wam) {


        // Initial commands needed for setup
        BARRETT_UNITS_TEMPLATE_TYPEDEFS(DOF);
        int port = 1;
        printf("Using CAN bus port %d.\n", port);
        bus::CANSocket bus(port);
        EnableEPOS(&bus, 0x601);
        wam.gravityCompensate();
        typedef boost::tuple<double, jp_type> jp_sample_type;


        // Initializing the threads for BioTac data and BarrettHand strain gage
collection
        bool going = true;     // flag to go into the main parts of the following
threads
        boost::thread thread(readThread, &bus, &going);
        //boost::thread threadBarrettHand(BarrettHandSGThread, &going);
        boost::thread threadBioTac(BioTacThread, &going);


        // ???
        systems::Ramp time(pm.getExecutionManager());



        // ------ 1) Loading information from data file --> order of features to
explore ------
        Small_Feature_to_Explore();



        // ------ 2) Move WAM to starting point (trajectory: 'firstmove_S_feat') -
-----

        // Reading file "firstmove_S_feat" and saving the data into a vector
        log::Reader<jp_sample_type> lr("firstmove_S_feat"); //_Roll
        std::vector<jp_sample_type> vec;
        for (size_t i = 0; i < lr.numRecords(); ++i) {
                vec.push_back(lr.getRecord());
        }
```

```
        // Initialize the system with number of iteration and hold positions
between iterations
        int numOfRuns(1);
        printf("\nHow many iteration (i.e. number of runs) would you like? __ ");
        std::cin >> numOfRuns;
        printf("\nHold points off? (y: no holding points) any other value is
no...");
        char check = 'n';
        std::cin >> check;
        waitForEnter();
        int holdPoint(1);

        if( check == 'y' ){
                printf("\nHold points OFF! be careful!");
                holdPoint =0;
        }
        if(holdPoint){
                printf("\nCheck that firstmove vec makes sense... size = %4.0ld\n
Press [Enter] to continue...",lr.numRecords());
                waitForEnter();
        }

        math::Spline<jp_type> spline(vec);

        // First, move to the starting position
        wam.moveTo(spline.eval(spline.initialS()));

        // Then play back the recorded motion
        time.stop();
        time.setOutput(spline.initialS());

        systems::Callback<double, jp_type> trajectory(boost::ref(spline));
        connect(time.output, trajectory.input);
        wam.trackReferenceSignal(trajectory.output);
        time.start();
        while (trajectory.input.getValue() < spline.finalS()) {
                usleep(100000);
        }



        // ------ 3) Defining the trajectory movements of the different small
features ------

        // Exploratory trajectory of small feature #1
        log::Reader<jp_sample_type> lr_S_feat_1("exp_S_feat_1"); //_Roll
        std::vector<jp_sample_type> vec_S_feat_1;
        for (size_t i = 0; i < lr_S_feat_1.numRecords(); ++i) {
                vec_S_feat_1.push_back(lr_S_feat_1.getRecord());
        }
        math::Spline<jp_type> spline_S_feat_1(vec_S_feat_1);
        if(holdPoint){
                printf("\nTraj vector for small feature #1... numRecords = %4.0ld\n
Press [Enter] to continue...",
                                lr_S_feat_1.numRecords());
                waitForEnter();
        }
        //wam.moveTo(spline_S_feat_1.eval(spline_S_feat_1.initialS()));
        //time.stop();
        //time.setOutput(spline_S_feat_1.initialS());
        systems::Callback<double, jp_type>
trajectory_S_feat_1(boost::ref(spline_S_feat_1));
        connect(time.output, trajectory_S_feat_1.input);


        // Exploratory trajectory of small feature #2
        log::Reader<jp_sample_type> lr_S_feat_2("exp_S_feat_2"); //_Roll
        std::vector<jp_sample_type> vec_S_feat_2;
        for (size_t i = 0; i < lr_S_feat_2.numRecords(); ++i) {
```

```
                vec_S_feat_2.push_back(lr_S_feat_2.getRecord());
        }
        math::Spline<jp_type> spline_S_feat_2(vec_S_feat_2);
        if(holdPoint){
                printf("\nTraj vector for small feature #2... numRecords = %4.0ld\n
Press [Enter] to continue...",
                                lr_S_feat_2.numRecords());
                waitForEnter();
        }
        systems::Callback<double, jp_type>
trajectory_S_feat_2(boost::ref(spline_S_feat_2));
        connect(time.output, trajectory_S_feat_2.input);


        // Exploratory trajectory of small feature #3
        log::Reader<jp_sample_type> lr_S_feat_3("exp_S_feat_3"); //_Roll
        std::vector<jp_sample_type> vec_S_feat_3;
        for (size_t i = 0; i < lr_S_feat_3.numRecords(); ++i) {
                vec_S_feat_3.push_back(lr_S_feat_3.getRecord());
        }
        math::Spline<jp_type> spline_S_feat_3(vec_S_feat_3);
        if(holdPoint){
                printf("\nTraj vector for small feature #3... numRecords = %4.0ld\n
Press [Enter] to continue...",
                                lr_S_feat_3.numRecords());
                waitForEnter();
        }
        systems::Callback<double, jp_type>
trajectory_S_feat_3(boost::ref(spline_S_feat_3));
        connect(time.output, trajectory_S_feat_3.input);


        // Exploratory trajectory of small feature #4
        log::Reader<jp_sample_type> lr_S_feat_4("exp_S_feat_4"); //_Roll
        std::vector<jp_sample_type> vec_S_feat_4;
        for (size_t i = 0; i < lr_S_feat_4.numRecords(); ++i) {
                vec_S_feat_4.push_back(lr_S_feat_4.getRecord());
        }
        math::Spline<jp_type> spline_S_feat_4(vec_S_feat_4);
        if(holdPoint){
                printf("\nTraj vector for small feature #4... numRecords = %4.0ld\n
Press [Enter] to continue...",
                                lr_S_feat_4.numRecords());
                waitForEnter();
        }
        systems::Callback<double, jp_type>
trajectory_S_feat_4(boost::ref(spline_S_feat_4));
        connect(time.output, trajectory_S_feat_4.input);


        // Exploratory trajectory of small feature #5
        log::Reader<jp_sample_type> lr_S_feat_5("exp_S_feat_5"); //_Roll
        std::vector<jp_sample_type> vec_S_feat_5;
        for (size_t i = 0; i < lr_S_feat_5.numRecords(); ++i) {
                vec_S_feat_5.push_back(lr_S_feat_5.getRecord());
        }
        math::Spline<jp_type> spline_S_feat_5(vec_S_feat_5);
        if(holdPoint){
                printf("\nTraj vector for small feature #5... numRecords = %4.0ld\n
Press [Enter] to continue...",
                                lr_S_feat_5.numRecords());
                waitForEnter();
        }
        systems::Callback<double, jp_type>
trajectory_S_feat_5(boost::ref(spline_S_feat_5));
        connect(time.output, trajectory_S_feat_5.input);


        // Exploratory trajectory of small feature #6
```

```
	log::Reader<jp_sample_type> lr_S_feat_6("exp_S_feat_6"); //_Roll
	std::vector<jp_sample_type> vec_S_feat_6;
	for (size_t i = 0; i < lr_S_feat_6.numRecords(); ++i) {
		vec_S_feat_6.push_back(lr_S_feat_6.getRecord());
	}
	math::Spline<jp_type> spline_S_feat_6(vec_S_feat_6);
	if(holdPoint){
		printf("\nTraj vector for small feature #6... numRecords = %4.0ld\n
Press [Enter] to continue...",
				lr_S_feat_6.numRecords());
		waitForEnter();
	}
	systems::Callback<double, jp_type>
trajectory_S_feat_6(boost::ref(spline_S_feat_6));
	connect(time.output, trajectory_S_feat_6.input);


	// Exploratory trajectory of small feature #7
	log::Reader<jp_sample_type> lr_S_feat_7("exp_S_feat_7"); //_Roll
	std::vector<jp_sample_type> vec_S_feat_7;
	for (size_t i = 0; i < lr_S_feat_7.numRecords(); ++i) {
		vec_S_feat_7.push_back(lr_S_feat_7.getRecord());
	}
	math::Spline<jp_type> spline_S_feat_7(vec_S_feat_7);
	if(holdPoint){
		printf("\nTraj vector for small feature #7... numRecords = %4.0ld\n
Press [Enter] to continue...",
				lr_S_feat_7.numRecords());
		waitForEnter();
	}
	systems::Callback<double, jp_type>
trajectory_S_feat_7(boost::ref(spline_S_feat_7));
	connect(time.output, trajectory_S_feat_7.input);


	// Exploratory trajectory of small feature #8
	log::Reader<jp_sample_type> lr_S_feat_8("exp_S_feat_8"); //_Roll
	std::vector<jp_sample_type> vec_S_feat_8;
	for (size_t i = 0; i < lr_S_feat_8.numRecords(); ++i) {
		vec_S_feat_8.push_back(lr_S_feat_8.getRecord());
	}
	math::Spline<jp_type> spline_S_feat_8(vec_S_feat_8);
	if(holdPoint){
		printf("\nTraj vector for small feature #8... numRecords = %4.0ld\n
Press [Enter] to continue...",
				lr_S_feat_8.numRecords());
		waitForEnter();
	}
	systems::Callback<double, jp_type>
trajectory_S_feat_8(boost::ref(spline_S_feat_8));
	connect(time.output, trajectory_S_feat_8.input);




	//DATA LOGGER SETUP ----------------------------------------------------
-------------------------//
	systems::TupleGrouper<double, jp_type, jv_type, jt_type, cp_type,
Eigen::Quaterniond> tg;
	connect(time.output, tg.template getInput<0>());
	connect(wam.jpOutput, tg.template getInput<1>());
	connect(wam.jvOutput, tg.template getInput<2>());
	connect(wam.jtSum.output, tg.template getInput<3>());
	connect(wam.toolPosition.output, tg.template getInput<4>());
	connect(wam.toolOrientation.output, tg.template getInput<5>());

	typedef boost::tuple<double, jp_type, jv_type, jt_type, cp_type,
Eigen::Quaterniond> tuple_type;
	const size_t PERIOD_MULTIPLIER = 5;
```

```
	//-------------------------------------------------------------------------
-------------------------//



	// ------ 4) Loop that runs with the specified number of iterations ------
	for(int j(0); j<numOfRuns; j++)
	{
		// Verification of read data file with small feature randomization
		if(holdPoint)
		{
			printf("\nPress [ENTER] to start iteration # %4.0d\n    Num
of angles %ld", j+1, OverallDimensionVec.size());
			waitForEnter();
		}

		// Loop that runs the number of rows in the Trajectory Info data
file
		for(unsigned int i=0; i<OverallDimensionVec.size(); i++)
		{

			// --- a. Defining the output file names ---
			switch( int(OverallDimensionVec[i]*1000) )
			{
			case 2000:	// Overall dimension of feature is 2 cm
				rec_duration =
(int)ceil((double)lr_S_feat_1.numRecords()/100);		break;
			case 1500:	// Overall dimension of feature is 1.5 cm
				rec_duration =
(int)ceil((double)lr_S_feat_2.numRecords()/100);		break;
			case 1000:	// Overall dimension of feature is 1.0 cm
				rec_duration =
(int)ceil((double)lr_S_feat_3.numRecords()/100);		break;
			case 750:	// Overall dimension of feature is 0.75 cm
				rec_duration =
(int)ceil((double)lr_S_feat_4.numRecords()/100);		break;
			case 500:	// Overall dimension of feature is 0.50 cm
				rec_duration =
(int)ceil((double)lr_S_feat_5.numRecords()/100);		break;
			case 375:	// Overall dimension of feature is 0.375 cm
				rec_duration =
(int)ceil((double)lr_S_feat_6.numRecords()/100);		break;
			case 250:	// Overall dimension of feature is 0.250 cm
				rec_duration =
(int)ceil((double)lr_S_feat_7.numRecords()/100);		break;
			case 125:	// Overall dimension of feature is 0.125 cm
				rec_duration =
(int)ceil((double)lr_S_feat_8.numRecords()/100);		break;
			}
			BTn = sprintf(BTfilename, "./BioTac
S_feat_BTData/BT_%d_BT%ddeg_%dcmPERs_%.1fmm__%s_%.3fcm_%s_%d.txt %d", //_Roll
								DateVec[i], BTdegVec[i],
VelVec[i], (double)PushVec[i], TypeVec[i].c_str(),

		(double)OverallDimensionVec[i], HeightVec[i].c_str(), TrialVec[i],
								rec_duration);
			BTn = sprintf(BHfilename,
"S_feat_BTHand/SG_%d_BT%ddeg_%dcmPERs_%.1fmm__%s_%.3fcm_%s_%d.txt", //_Roll
								DateVec[i], BTdegVec[i],
VelVec[i], (double)PushVec[i], TypeVec[i].c_str(),

		(double)OverallDimensionVec[i], HeightVec[i].c_str(), TrialVec[i]);
			BTn = sprintf(WAMfilename,
"S_feat_BTWAMdata/WAM_%d_BT%ddeg_%dcmPERs_%.1fmm__%s_%.3fcm_%s_%d.csv", //_Roll
								DateVec[i], BTdegVec[i],
VelVec[i], (double)PushVec[i], TypeVec[i].c_str(),

		(double)OverallDimensionVec[i], HeightVec[i].c_str(), TrialVec[i]);
```

```
                        printf("%s\n",BTfilename);
                        printf("%d\n",rec_duration);
                        btsleep(0.1);



                        // --- b. Turn on BioTac data collection ---
                        BTrecord = true;
                        btsleep(0.75); //Let the WAM reach its starting point

                        // Turning the switch ON (to control load cell data
recording)
                        printf("\nTurning on Magnet\n");
                        DigitalOutputOn(&bus, 0x601);
                        DisableState(&bus, 0x601);
                        btsleep(0.75);

                        // WAM Data Logging
                        char tmpFile[] = "/tmp/btXXXXXX";
                        if (mkstemp(tmpFile) == -1) {
                                printf("ERROR: Couldn't create temporary file!\n");
                                return 1;
                        }
                        systems::PeriodicDataLogger<tuple_type>
logger(pm.getExecutionManager(),
                        new log::RealTimeWriter<tuple_type>(tmpFile,
PERIOD_MULTIPLIER * pm.getExecutionManager()->getPeriod()),
                        PERIOD_MULTIPLIER);
                        printf("Logging Initialized.\n");



                        // --- c. Perform exploratory movement based on listed
feature's dimension ---
                        switch( int(OverallDimensionVec[i]*1000) )
                        {
                        case 2000:     // Overall dimension of feature is 2 cm

        wam.moveTo(spline_S_feat_1.eval(spline_S_feat_1.initialS()));
                                time.stop();
                                time.setOutput(spline_S_feat_1.initialS());


        wam.trackReferenceSignal(trajectory_S_feat_1.output);
                                time.stop();
                                time.setOutput(spline_S_feat_1.initialS());
                                connect(tg.output, logger.input);     // To connect
to logger
                                time.start();
                                while (trajectory_S_feat_1.input.getValue() <
spline_S_feat_1.finalS()) {
                                        usleep(50000);
                                }
                                break;

                        case 1500:     // Overall dimension of feature is 1.5 cm

        wam.moveTo(spline_S_feat_2.eval(spline_S_feat_2.initialS()));
                                time.stop();
                                time.setOutput(spline_S_feat_2.initialS());


        wam.trackReferenceSignal(trajectory_S_feat_2.output);
                                time.stop();
                                time.setOutput(spline_S_feat_2.initialS());
                                connect(tg.output, logger.input);     // To connect
to logger (NEEDED to start logging in every case)
                                time.start();
```

```
                                while (trajectory_S_feat_2.input.getValue() <
spline_S_feat_2.finalS()) {
                                        usleep(50000);
                                }
                                break;

                        case 1000:      // Overall dimension of feature is 1.0 cm

        wam.moveTo(spline_S_feat_3.eval(spline_S_feat_3.initialS()));
                                time.stop();
                                time.setOutput(spline_S_feat_3.initialS());


        wam.trackReferenceSignal(trajectory_S_feat_3.output);
                                time.stop();
                                time.setOutput(spline_S_feat_3.initialS());
                                connect(tg.output, logger.input);     // To connect
to logger (NEEDED to start logging in every case)
                                time.start();
                                while (trajectory_S_feat_3.input.getValue() <
spline_S_feat_3.finalS()) {
                                        usleep(50000);
                                }
                                break;

                        case 750:       // Overall dimension of feature is 0.75 cm

        wam.moveTo(spline_S_feat_4.eval(spline_S_feat_4.initialS()));
                                time.stop();
                                time.setOutput(spline_S_feat_4.initialS());


        wam.trackReferenceSignal(trajectory_S_feat_4.output);
                                time.stop();
                                time.setOutput(spline_S_feat_4.initialS());
                                connect(tg.output, logger.input);     // To connect
to logger (NEEDED to start logging in every case)
                                time.start();
                                while (trajectory_S_feat_4.input.getValue() <
spline_S_feat_4.finalS()) {
                                        usleep(50000);
                                }
                                break;

                        case 500:       // Overall dimension of feature is 0.50 cm

        wam.moveTo(spline_S_feat_5.eval(spline_S_feat_5.initialS()));
                                time.stop();
                                time.setOutput(spline_S_feat_5.initialS());


        wam.trackReferenceSignal(trajectory_S_feat_5.output);
                                time.stop();
                                time.setOutput(spline_S_feat_5.initialS());
                                connect(tg.output, logger.input);     // To connect
to logger (NEEDED to start logging in every case)
                                time.start();
                                while (trajectory_S_feat_5.input.getValue() <
spline_S_feat_5.finalS()) {
                                        usleep(50000);
                                }
                                break;

                        case 375:       // Overall dimension of feature is 0.375 cm

        wam.moveTo(spline_S_feat_6.eval(spline_S_feat_6.initialS()));
                                time.stop();
                                time.setOutput(spline_S_feat_6.initialS());
```

```
        wam.trackReferenceSignal(trajectory_S_feat_6.output);
                                time.stop();
                                time.setOutput(spline_S_feat_6.initialS());
                                connect(tg.output, logger.input);     // To connect
to logger (NEEDED to start logging in every case)
                                time.start();
                                while (trajectory_S_feat_6.input.getValue() <
spline_S_feat_6.finalS()) {
                                        usleep(50000);
                                }
                                break;

                        case 250:       // Overall dimension of feature is 0.25 cm

        wam.moveTo(spline_S_feat_7.eval(spline_S_feat_7.initialS()));
                                time.stop();
                                time.setOutput(spline_S_feat_7.initialS());


        wam.trackReferenceSignal(trajectory_S_feat_7.output);
                                time.stop();
                                time.setOutput(spline_S_feat_7.initialS());
                                connect(tg.output, logger.input);     // To connect
to logger (NEEDED to start logging in every case)
                                time.start();
                                while (trajectory_S_feat_7.input.getValue() <
spline_S_feat_7.finalS()) {
                                        usleep(50000);
                                }
                                break;

                        case 125:       // Overall dimension of feature is 0.125 cm

        wam.moveTo(spline_S_feat_8.eval(spline_S_feat_8.initialS()));
                                time.stop();
                                time.setOutput(spline_S_feat_8.initialS());


        wam.trackReferenceSignal(trajectory_S_feat_8.output);
                                time.stop();
                                time.setOutput(spline_S_feat_8.initialS());
                                connect(tg.output, logger.input);     // To connect
to logger (NEEDED to start logging in every case)
                                time.start();
                                while (trajectory_S_feat_8.input.getValue() <
spline_S_feat_8.finalS()) {
                                        usleep(50000);
                                }
                                break;

                        }

                        //      Closing the data logger to prepare for next run
                        logger.closeLog();
                        printf("Logging stopped.\n");
                        log::Reader<tuple_type> lrr(tmpFile);
                        lrr.exportCSV(WAMfilename);
                        printf("Output written to %s.\n", WAMfilename);
                        std::remove(tmpFile);

                        btsleep(2);
                        DigitalOutputOff(&bus, 0x601);


                        if(holdPoint)
                        {
                        printf("\nPress [ENTER] to start the next movement");
                        waitForEnter();
```

```
                        }
                }


        }



        // ------ 5) Finishing the experiment and closing evertyhing ------
        if(holdPoint){
                printf("\nDone with iterations. Press [ENTER] to zero turn table
and return WAM to home.");
                waitForEnter();
        }
        btsleep(1);


        // Setting the WAM back to the starting/home positions and turning
everything off
        wam.moveHome();
        wam.idle();
    pm.getSafetyModule()->waitForMode(SafetyModule::IDLE);
        going = false;
        BTrecord = false;       //just to be safe

        /*
        // Turning the different threads off
                        thread.join();
                        threadBarrettHand.join();
                        threadBioTac.join();
        */

        return 0;
}
```

APPENDIX C

COPYRIGHT PERMISSIONS

ELSEVIER LICENSE
TERMS AND CONDITIONS

Jul 16, 2013

This is a License Agreement between Ruben D Ponce Wong ("You") and Elsevier ("Elsevier") provided by Copyright Clearance Center ("CCC"). The license consists of your order details, the terms and conditions provided by Elsevier, and the payment terms and conditions.

All payments must be made in full to CCC. For payment instructions, please see information listed at the bottom of this form.

Supplier	Elsevier Limited The Boulevard,Langford Lane Kidlington,Oxford,OX5 1GB,UK
Registered Company Number	1982084
Customer name	Ruben D Ponce Wong
Customer address	1249 E Spence Ave 133 TEMPE, AZ 85281
License number	3190301458391
License date	Jul 15, 2013
Licensed content publisher	Elsevier
Licensed content publication	Sensors and Actuators A: Physical
Licensed content title	Flexible microfluidic normal force sensor skin for tactile feedback
Licensed content author	Ruben D. Ponce Wong,Jonathan D. Posner,Veronica J. Santos
Licensed content date	June 2012
Licensed content volume number	179
Licensed content issue number	
Number of pages	8
Start Page	62
End Page	69
Type of Use	reuse in a thesis/dissertation
Portion	full article
Format	both print and electronic
Are you the author of this Elsevier article?	Yes
Will you be translating?	No
Order reference number	

Title of your thesis/dissertation	Towards Haptic Intelligence for Artificial Hands: Development and Use of Deformable, Fluidic Tactile Sensors to Relate Action and Perception
Expected completion date	Jul 2013
Estimated size (number of pages)	150
Elsevier VAT number	GB 494 6272 12
Permissions price	0.00 USD
VAT/Local Sales Tax	0.00 USD / 0.00 GBP
Total	0.00 USD
Terms and Conditions	

INTRODUCTION

1. The publisher for this copyrighted material is Elsevier. By clicking "accept" in connection with completing this licensing transaction, you agree that the following terms and conditions apply to this transaction (along with the Billing and Payment terms and conditions established by Copyright Clearance Center, Inc. ("CCC"), at the time that you opened your Rightslink account and that are available at any time at http://myaccount.copyright.com).

GENERAL TERMS

2. Elsevier hereby grants you permission to reproduce the aforementioned material subject to the terms and conditions indicated.

3. Acknowledgement: If any part of the material to be used (for example, figures) has appeared in our publication with credit or acknowledgement to another source, permission must also be sought from that source. If such permission is not obtained then that material may not be included in your publication/copies. Suitable acknowledgement to the source must be made, either as a footnote or in a reference list at the end of your publication, as follows:

"Reprinted from Publication title, Vol /edition number, Author(s), Title of article / title of chapter, Pages No., Copyright (Year), with permission from Elsevier [OR APPLICABLE SOCIETY COPYRIGHT OWNER]." Also Lancet special credit - "Reprinted from The Lancet, Vol. number, Author(s), Title of article, Pages No., Copyright (Year), with permission from Elsevier."

4. Reproduction of this material is confined to the purpose and/or media for which permission is hereby given.

5. Altering/Modifying Material: Not Permitted. However figures and illustrations may be altered/adapted minimally to serve your work. Any other abbreviations, additions, deletions and/or any other alterations shall be made only with prior written authorization of Elsevier Ltd. (Please contact Elsevier at permissions@elsevier.com)

6. If the permission fee for the requested use of our material is waived in this instance, please be advised that your future requests for Elsevier materials may attract a fee.

7. Reservation of Rights: Publisher reserves all rights not specifically granted in the combination of (i) the license details provided by you and accepted in the course of this licensing transaction, (ii) these terms and conditions and (iii) CCC's Billing and Payment terms and conditions.

8. License Contingent Upon Payment: While you may exercise the rights licensed immediately upon issuance of the license at the end of the licensing process for the transaction, provided that you have disclosed complete and accurate details of your proposed use, no license is finally effective unless and until full payment is received from you (either by publisher or by CCC) as provided in CCC's Billing and Payment terms and conditions. If full payment is not received on a timely basis, then any license preliminarily granted shall be deemed automatically revoked and shall be void as if never granted. Further, in the event that you breach any of these terms and conditions or any of CCC's Billing and Payment terms and conditions, the license is automatically revoked and shall be void as if never granted. Use of materials as described in a revoked license, as well as any use of the materials beyond the scope of an unrevoked license, may constitute copyright infringement and publisher reserves the right to take any and all action to protect its copyright in the materials.

9. Warranties: Publisher makes no representations or warranties with respect to the licensed material.

10. Indemnity: You hereby indemnify and agree to hold harmless publisher and CCC, and their respective officers, directors, employees and agents, from and against any and all claims arising out of your use of the licensed material other than as specifically authorized pursuant to this license.

11. No Transfer of License: This license is personal to you and may not be sublicensed, assigned, or transferred by you to any other person without publisher's written permission.

12. No Amendment Except in Writing: This license may not be amended except in a writing signed by both parties (or, in the case of publisher, by CCC on publisher's behalf).

13. Objection to Contrary Terms: Publisher hereby objects to any terms contained in any purchase order, acknowledgment, check endorsement or other writing prepared by you, which terms are inconsistent with these terms and conditions or CCC's Billing and Payment terms and conditions. These terms and conditions, together with CCC's Billing and Payment terms and conditions (which are incorporated herein), comprise the entire agreement between you and publisher (and CCC) concerning this licensing transaction. In the event of any conflict between your obligations established by these terms and conditions and those established by CCC's Billing and Payment terms and conditions, these terms and conditions shall control.

14. Revocation: Elsevier or Copyright Clearance Center may deny the permissions described in this License at their sole discretion, for any reason or no reason, with a full refund payable to you. Notice of such denial will be made using the contact information provided by you. Failure to receive such notice will not alter or invalidate the denial. In no event will Elsevier or Copyright Clearance Center be responsible or liable for any costs, expenses or damage incurred by you as a result of a denial of your permission request, other than a refund of the amount(s) paid by you to Elsevier and/or Copyright Clearance Center for denied permissions.

LIMITED LICENSE

The following terms and conditions apply only to specific license types:

15. **Translation**: This permission is granted for non-exclusive world **English** rights only unless your license was granted for translation rights. If you licensed translation rights you may only translate this content into the languages you requested. A professional translator must perform all translations and reproduce the content word for word preserving the integrity of the article. If this license is to re-use 1 or 2 figures then permission is granted for non-exclusive world rights in all languages.

16. **Website**: The following terms and conditions apply to electronic reserve and author websites:
Electronic reserve: If licensed material is to be posted to website, the web site is to be password-protected and made available only to bona fide students registered on a relevant course if:
This license was made in connection with a course,
This permission is granted for 1 year only. You may obtain a license for future website posting,
All content posted to the web site must maintain the copyright information line on the bottom of each image,
A hyper-text must be included to the Homepage of the journal from which you are licensing at http://www.sciencedirect.com/science/journal/xxxxx or the Elsevier homepage for books at http://www.elsevier.com , and
Central Storage: This license does not include permission for a scanned version of the material to be stored in a central repository such as that provided by Heron/XanEdu.

17. **Author website** for journals with the following additional clauses:

All content posted to the web site must maintain the copyright information line on the bottom of each image, and the permission granted is limited to the personal version of your paper. You are not allowed to download and post the published electronic version of your article (whether PDF or HTML, proof or final version), nor may you scan the printed edition to create an electronic version.
A hyper-text must be included to the Homepage of the journal from which you are licensing at http://www.sciencedirect.com/science/journal/xxxxx . As part of our normal production process, you will receive an e-mail notice when your article appears on Elsevier's online service ScienceDirect (www.sciencedirect.com). That e-mail will include the article's Digital Object Identifier (DOI). This number provides the electronic link to the published article and should be included in the posting of your personal version. We ask that you wait until you receive this e-mail and have the DOI to do any posting.

Central Storage: This license does not include permission for a scanned version of the material to be stored in a central repository such as that provided by Heron/XanEdu.

18. **Author website** for books with the following additional clauses:
Authors are permitted to place a brief summary of their work online only.
A hyper-text must be included to the Elsevier homepage at http://www.elsevier.com . All content posted to the web site must maintain the copyright information line on the bottom of each image.
You are not allowed to download and post the published electronic version of your chapter, nor may you scan the printed edition to create an electronic version.

Central Storage: This license does not include permission for a scanned version of the material to be stored in a central repository such as that provided by Heron/XanEdu.

19. **Website** (regular and for author): A hyper-text must be included to the Homepage of the journal from which you are licensing at http://www.sciencedirect.com/science/journal/xxxxx. or for books to the Elsevier homepage at http://www.elsevier.com

20. **Thesis/Dissertation**: If your license is for use in a thesis/dissertation your thesis may be submitted to your institution in either print or electronic form. Should your thesis be published commercially, please reapply for permission. These requirements include permission for the Library and Archives of Canada to supply single copies, on demand, of the complete thesis and include permission for UMI to supply single copies, on demand, of the complete thesis. Should your thesis be published commercially, please reapply for permission.

21. **Other Conditions**:

v1.6

If you would like to pay for this license now, please remit this license along with your payment made payable to "COPYRIGHT CLEARANCE CENTER" otherwise you will be invoiced within 48 hours of the license date. Payment should be in the form of a check or money order referencing your account number and this invoice number RLNK501066100. Once you receive your invoice for this order, you may pay your invoice by credit card. Please follow instructions provided at that time.

Make Payment To:
Copyright Clearance Center
Dept 001
P.O. Box 843006
Boston, MA 02284-3006

For suggestions or comments regarding this order, contact RightsLink Customer Support: customercare@copyright.com or +1-877-622-5543 (toll free in the US) or +1-978-646-2777.

Gratis licenses (referencing $0 in the Total field) are free. Please retain this printable license for your reference. No payment is required.